



universität
wien

DISSERTATION

Titel der Dissertation

Modeling and Simulation of Field-Effect Biosensors

Verfasserin

Dipl.-Math. Alena Bulyha

angestrebter akademischer Grad

Doktorin der Naturwissenschaften (Dr.rer.nat)

Wien, im Juni 2011

Studienkennzahl lt. Studienblatt:	A 091 405
Dissertationsgebiet lt. Studienblatt:	Mathematik
Betreuer:	Univ.-Prof. Dr. Norbert J. Mauser
co-Betreuer:	Privatdoz. Dr. Clemens Heitzinger

Acknowledgements

I am very grateful to Prof. Dr. Norbert J. Mauser and Dr. Clemens Heitzinger for their supervision and their constant and efficient support of my work. I am also thankful to Prof. Dr. Christoph W. Überhuber for introducing me into the field of my current PhD study. I thank my supervisors for their openness and believe that I can handle challenges, and in particular, for their patience and sympathy. I am really glad that I had got this opportunity to learn from you and I hope that we will collaborate a lot in the future.

Further I want to thank my colleagues Stefan Baumgartner, Marina Rehl, Nathalie Tassotti and Dr. Martin Vasicek, who worked with me and with whom I discussed many ideas. You were always willing to share your knowledges. I thank Dr. Hans-Peter Stimming and Dr. Nikolaos Sfakianakis, who helped me to solve mathematical problems.

I also thank Frau Stefanie Preuss for most efficient and friendly support in all administrative matters.

Furthermore I am grateful to my family, especially to my husband Sergei, for their trust in me and for their sympathetic support during my study.

This work was supported by the Austrian Science Fund (FWF) via the projects W8: "Wissenschaftskolleg: Differential Equations" and P20871-N13: "Mathematical Models and Characterization of BioFETs", the Viennese Fund for Science and Technology (WWTF) via the project MA09-28 "Mathematics and Nanosensors" and the Stadt Wien - Austrian Academy of Sciences via the project "Multi-Scale Modeling and Simulation of Field-Effect Nano-Biosensors" (Jubiläumsfond). Also, we acknowledge funding from the European Commission via the Marie-Curie project: "European Doctoral School in Mathematics: Differential Equations with Applications in Science and Engineering (DEASE)" (No. MEST-CT-2005-021122).

Abstract

This work is motivated by the need for a theoretical understanding of the functioning of field-effect biosensors or BioFETs (Field-Effect Transistors). The field-effect biosensor is a complex multi-scale system where a semiconductor device is coupled to a biologically sensitive layer (receptors or probes) that detects analyte biomolecules (targets), for instance DNA, in an electrolyte. The principle of BioFETs is the following: when the analyte biomolecules bind to the surface receptors, the charge distribution at the surface changes; that modulates the electrostatic potential in the semiconductor and, thus, its conductance, which can be measured.

The modeling of such BioFET sensors must take into account the electrostatics and the geometry of the liquid, of the probe and the target molecules in the boundary layer, the binding efficiency of the probes and targets, the electrostatics and the conductance of the semiconducting transducer and the device geometry. Note that the bio-physical and the nano-electronic parts define very different length scales, and therefore, they have to be considered separately and then coupled in a self-consistent manner.

In this thesis we provide a general mathematical concept to deal with transistors with DNA-modified insulator-electrolyte interface. For that we describe the functioning of the system as a whole and suggest corresponding segmentation for further treatment as well as the compilation procedures for previously segmented model. Besides a mathematical analysis of partial differential equations occurring in the model the main focus of the work is the modeling and simulation of the processes that occur in the bio-physical part of the sensors.

The simulation of the bio-functionalized surfaces poses special requirements on the Monte-Carlo simulations and these are addressed by the algorithm. The constant-voltage ensemble enables us to include the correct boundary conditions; the DNA (deoxyribonucleic acid) strands can be rotated with respect to the surface; and several molecules can be placed into a single simulation box in order to achieve good statistics in the case of low ionic concentrations, i.e. under conditions that are typically observed in experiments. Simulation results are presented for the leading example of surfaces functionalized with PNA (peptide nucleic acid) and with single- and double-stranded DNA in a sodium-chloride electrolyte. These quantitative results make it possible to quantify the screening of the biomolecule charge due to the counter-ions around the biomolecules and the electrical double layer. The resulting concentration profiles show a three-layer structure and non-trivial interactions between the electric double layer and the counter-ions.

We also identify the binding efficiency of the receptors to the DNAs of interest. For that we investigate the diffusive transport of the charged biomolecules and the two types of the chemical reactions near the functionalized surface, i.e. specific and non-specific binding. The well-posed problem is formulated, discretized and solved. We also present a simulation results and examine the diffusion and reaction processes as well as their interaction.

Furthermore, an approach is developed for device characterization that allows to deter-

mine the biological noise of the system and to identify the signal-to-noise ratio. We focus on the stochastic processes that occur at the functionalized surface. The chemical Langevin equation for a binding (i.e. association and dissociation) processes occurring at the functionalized surface is obtained. The binding efficiency of the biomolecules, the signal and the biological noise of the device are specified and calculated. The simulation results for binding efficiency and for signal-to-noise ratio are presented, compared and analyzed with respect to the response time.

Our mathematical modeling yields qualitative understanding of important properties of BioFETs and helps to provide high performance algorithms for predictive simulations.

Zusammenfassung

Die dieser Arbeit zugrunde liegende Motivation ist die Notwendigkeit des theoretischen Verstehens der Arbeitsweise von Feld-Effekt Biosensoren oder BioFETs (Feld-Effekt Transistoren). Der Feld-Effekt Biosensor ist ein komplexes "Multi-skalen" System. Der Halbleiter ist hierbei an die biologisch-empfindliche Schicht (bestehend aus Rezeptoren/Proben) gekoppelt, welche die zu erfassenden Analytmoleküle (Targets), wie etwa DNS, in einer Elektrolytlösung detektiert. Das Grundprinzip von BioFETs ist im Folgenden kurz erläutert: Wenn sich Analyt-Biomoleküle an Oberflächenrezeptoren binden, ändert sich die Ladungsverteilung nahe der Oberfläche. Dies führt zu einer messbaren Änderung von elektrostatischem Potenzial und Leitwert im Halbleiter.

Neben zahlreicher anderer Faktoren muss die Modellierung von BioFET Sensoren auch die Elektrostatik und Geometrie von Flüssigkeitsbestandteilen und Biomolekülen, die Bindungseffizienz ebendieser Probe- und Targetmoleküle auf der Grenzschicht, die Elektrostatik und Leitfähigkeit des Halbleitertransducers sowie die Sensorgeometrie berücksichtigen. Hierbei ist zu beachten, dass die bio-physikalischen und nano-elektronischen Bestandteile des Sensors von stark unterschiedlichem Längenmaßstab sind und somit getrennt betrachtet werden müssen und dann auf selbst-konsistente Art und Weise verbunden werden.

Diese Dissertation gibt ein allgemeines mathematisches Konzept für Transistoren, deren Grenzschicht zwischen Isolator und Elektrolytlösung mit DNA modifiziert wurde. Dafür beschreiben wir die Arbeitsweise des Systems als Ganzes und schlagen eine Segmentierung in Einzelmodelle vor, ebenso wie eine Methode zur späteren Zusammenführung der einzelnen Modellbestandteile. Neben einer mathematischen Analysis von partiellen Differentialgleichungen des Modells ist die Hauptaufmerksamkeit hierbei auf die Modellierung und Simulation von Prozessen gerichtet, die in der bio-physikalische Bestandteilen des Sensors auftreten.

Die Simulation von bio-funktionalisierten Oberflächen stellen bestimmte Anforderungen an die Simulation, welche mit einem Monte Carlo Algorithmus verwirklicht werden. Das konstantgehaltene Potenzial ermöglicht hierbei die Berücksichtigung der zugehörigen präzisen Randbedingungen: DNS-Stränge können an der Oberfläche rotiert werden und mehrere Moleküle können sich in einem Simulationsteilgebiet aufhalten. Letztere Bedingung ist notwendig um eine gute Statistik im Fall niedriger Ionenkonzentration zu erhalten. Die Simulationsergebnisse repräsentieren Oberflächen die mit PNS (Peptid-Nukleinsäure) und mit einzel und doppelsträngigen DNS-Molekülen (Desoxyribonukleinsäure) funktionalisiert sind und sich in einer Natriumchloridflüssigkeit befinden. Diese quantitativen Ergebnisse ermöglichen ein Screening der Biomolekülladungen, bedingt durch die Anwesenheit von Gegenionen in der Nähe von Biomolekülen und elektrischen Doppelschicht. Die Simulationsergebnissen zeigen drei-schichtige Strukturen ebenso wie eine nicht triviale Wechselwirkung zwischen der elektrischen Doppelschicht und den Gegenionen.

Wir bestimmen ebenso die Bindungseffizienz zwischen Rezeptoren und DNS-Molekülen. Dafür erforschen wir den diffusiven Transport der geladenen Biomoleküle ebenso wie die beiden möglichen Arten von chemischen Reaktionen in der Nähe der funktionalisierten Oberfläche,

genauer gesagt die spezifische und nicht spezifische Bindung. Dieses wohldefinierte Problem wurde mathematisch formuliert, diskretisiert und numerisch gelöst. Darüber hinaus präsentieren wir Simulationsergebnisse zu den untersuchten Diffusions- und Reaktionsprozessen, ebenso wie ihre wechselseitige Beeinflussung.

Außerdem wurde ein Verfahren zur Charakterisierung von Biosensoren entwickelt, welches das biologische Rauschen des Systems ermitteln kann. Wir konzentrieren uns hierbei auf stochastische Prozesse, die in der Nähe der funktionalisierten Oberfläche auftreten. Die chemische Langevin Gleichung wurde zur Beschreibung von Assoziations- und Dissoziationsprozessen an der Oberfläche hergeleitet. Die Bindungseffizienz der Biomoleküle, das Signal und das biologische Rauschen des Sensors wurden spezifiziert und kalkuliert. Die Simulationsergebnisse zu Bindungseffizienz und Signal-to-Noise Ratio wurden dargestellt, und bezüglich Antwortzeit verglichen und analysiert.

Unsere mathematisches Modell leistet somit einen maßgeblichen Beitrag zum qualitativen Verständnis der wichtigen Eigenschaften von BioFET Sensoren und liefert einen Hochleistungsalgorithmus zur Vorhersage verschiedenster Vorgänge im Sensor.

Contents

Acknowledgments	ix
Abstract	ix
Zusammenfassung	ix
Contents	ix
1 Introduction	1
2 DNA-modified FET	7
2.1 Physical structure: basic charged components	7
2.2 Mathematical models of charged BioFET-components	9
2.2.1 Electrons and holes	10
2.2.2 Biomolecules	13
2.2.3 Electrolyte ions	17
2.2.4 Hydrogen ions	19
2.2.5 Insulator	22
2.3 Conclusions	22
3 Electrolyte solution in the equilibrium state	25
3.1 Atomistic model	26
3.1.1 Simulation domain	26
3.1.2 Metropolis Monte Carlo simulation in the constant-voltage ensemble .	27
3.1.3 Chemical potential	29
3.1.4 Electrostatic potential energy	30

3.2	Simulation results	34
3.3	Conclusions	40
4	Transport of charged biomolecules with chemical reactions near the surface	43
4.1	Continuum model for the analyte flow	43
4.1.1	Adsorption of biomolecules: specific and non-specific binding	43
4.1.2	Model equations	45
4.2	Discretized model	54
4.2.1	Conservative scheme	54
4.2.2	Stability and convergence	56
4.3	Simulation results	58
4.4	Conclusions	61
5	Self-consistent model	63
5.1	Compilation procedures	64
5.2	Simulation results	66
5.3	Conclusions	70
6	Stochastic processes at the functionalized surface	71
6.1	Interaction processes	71
6.2	Chemical Langevin equation at the surface	72
6.3	Signal-to-Noise Ratio	74
6.4	Simulation results	78
6.5	Conclusions	83
A	Variables and units	85
B	Theorems	87
	Bibliography	89
	Curriculum Vitae	97

Chapter 1

Introduction

The detection and quantification of particular biomolecules is highly important in many areas of science and industry. Nowadays, the molecule-specific detectors or sensors are increasingly applied for the quality assurance in agriculture, food and pharmaceutical industries, for monitoring of environmental pollutants and biological warfare agents, for medical diagnostics, and for medical and pharmaceutical research and development, for instance, in proteomics and drug discovery. The new technology that is based on FET concept (field-effect transistor) combined with biologically modified surface layers (biologically sensitive field-effect transistors or devices, BioFETs or BioFEDs) is considered as a promising approach to sensitively and selectively detect the biomolecules of interest in the investigated samples, such a blood or physiological solution, in a fast and efficient way.

Since 1962, when L. C. Clark and C. Lyons [10] demonstrated for the first time "the possibilities for use of enzyme layers trapped between membranes used with electrodes" for sensing (so-called "enzyme electrode"), many efforts have been made in the field of biosensors and many different types of the devices have been developed [47, 52, 81].

The basic concept of biosensors is the integration of biologically active materials (or receptors) with a suitable transducer, which is usually coupled to an appropriate data processing system [48, 61]. The receptors are immersed into an electrolyte solution with the biomolecules (or analyte) of interest. As the receptors contact with the analyte molecules, a change in physical or chemical parameters of the system occurs. The transducer part convert these changes into a quantifiable (e.g. electrical, mechanical or optical) signal [34], then the response signal is processed and displayed in a suitable form. The specificity of the response is regulated by the placement and nature of the receptors, as well as by the nature of the detector.

The biological recognition element is a crucial part of the biosensor device. Different types of the biological materials of various complexity are used as recognition elements: from single biomolecules (e.g. nucleic acids, enzymes, proteins, antibodies) to living biological systems (e.g. cells, tissue slices, intact organs, microorganisms) [61]. The receptors also

distinguish from each other by the nature of the interaction processes: bio-catalytic (enzyme), immunological (antibody) and bio-affinity (DNA). Thus, the BioFETs can be classified by the type of the receptor: DNA-modified FET, enzyme-modified FET, immunologically modified FET with antibody-antigen binding and cell-based BioFET.

A wide variety of the transducer methods have been developed, which can be divided into labeled and label-free types. The labeled methods rely on the detection of specific labels, for instance fluorescence-, radioactive-, enzymatic-labels, etc., which have to be linked to analyte molecules. The label-free methods are based on the direct measurement of the physical change in the system that occurs during the reaction processes.

Classification of biosensors by the most common types of the biological materials and by the mostly used types of the transducer methods is summarized in Table 1.1.

Table 1.1: Classification of biosensors according to their structure.

Analyte:	\rightleftharpoons	Recognition elements:	\Rightarrow	Transducer:	\searrow \swarrow	Responses:
labeled label-free		DNAs Enzymes/Proteins Antibodies Living biological cells ...		Optical Piezoelectronic Calorimetric Electrochemical ...		Optical Acoustic Electrical Magnetic ...

According to the official nomenclature, which is proposed by the International Union of Pure and Applied Chemistry (IUPAC) [71], the electrochemical transducers can be also specified by their principles and include amperometric, potentiometric, conductometric, impedimetric and semiconductor field-effect.

In spite of the common concept, each type of the biosensor has its specific features, which make it significantly different from other types of sensors. Thus, different biosensors differ in their structure and physical and chemical processes. Therefore, it is not possible to make a universal mathematical model for the biosensors. In this work we focus upon DNA-modified FET (DNAFET) and consider a label-free electronic detection of DNAs by their intrinsic molecular charge using the field-effect platform. The transducer of DNAFET belongs to electrochemical class and it transforms a chemical change, which occurs after binding of DNAs, into an electric signal, i.e. into a change in electric current, resistance or voltage.

Among the wide variety of proposed types, such type of biosensors is of great interest nowadays and a number of highly sensitive and selective devices, which are based on DNAFET principles, are being developed [61, 68, 89]. The recently created label-free nanosensors [34, 35, 52, 58] demonstrate a great potential to detect disease markers directly in a physiological solution [69] and to provide a rapid, specific, sensitive, and low-cost point-of-care diagnosis.

The following definition of a BioFET was proposed by the International Union of Pure and

Applied Chemistry (IUPAC) [71]: "An electrochemical biosensor is a self-contained integrated device, which is capable of providing specific quantitative or semi-quantitative analytical information using a biological recognition element (biochemical receptor) which is retained in direct spatial contact with an electrochemical transduction element."

The development of biosensors is a multi-disciplinary research area that involves knowledge from solid state physics, bio- and electro-chemistry, electronics, mathematics and computer sciences. Because of the complexity of the biosensor functioning, the progress in the sensor technology is being accompanied by the development of mathematical models for particular processes that occur in each part of the developed devices.

The mathematical modeling facilitates a deeper understanding and simulation of individual processes and interactions of the parts of the system with each other, which enables an assessment of the functioning of the system as a whole. As a result, the modeling helps to predict the effect of changes to the system, to optimize the system performance and to improve the device design.

Since the invention of metal-oxide-semiconductor field-effect transistor (MOSFET) mathematical models have been developed for studies of semiconducting transducers, such as Poisson, Boltzmann, Vlasov, Drift-Diffusion equations, etc. [43,44,86], which are widely used nowadays. According to the goal of the investigation we select and further evolve the required model and corresponding numerical methods [19,41].

The studies of the behavior of liquids range from the observation of Brownian motion to the processing of ion-sensitive field-effect transistors (ISFETs). The various approaches for the simulation of liquids and the corresponding mathematical treatment include deterministic (e.g. Molecular Dynamic, Poisson-Boltzmann) as well as stochastic (e.g. Monte Carlo) methods, which describe the molecular model of liquid, the ion transport and the charge screening effect. For example, the Molecular Dynamic method [3, 21], which is based on the solution of Newton's equation of motion, is used to obtain the dynamic property of many-particle system. The Poisson-Boltzmann theory [13, 39, 49, 63, 70] allows to study the electric double-layer near the objects of simple geometry. The various modifications of the Monte Carlo methods have been developed and applied to study the behavior of static liquid [3, 9, 42, 46, 74, 76].

The studies of the transport of the biological species, which initially were performed in the field of physiology and cell and molecular biology, are contributing today to the research in the field of biosensors. In general, the mass transport occurs by both diffusion and convection. The spread of particles through random motion (diffusion) is described by the diffusion equation. From the previous studies the limitations of sensors due to potentially slow transport by diffusion in the static solution are known [64]. Temperature or pressure gradients between the chip and the analyte give rise to convection. This can be an advantageous effect, since it accelerates the transport of the analyte towards the sensor surface in contrast to the time-limiting properties of a pure diffusion mechanism. Furthermore, the pumps and the microfluidic system, such a those that have been developed in [68], can be used as efficient tools

for reducing the response times of particular sensors. Because many biomolecules are charged their transport is also influenced by the electric field, whereas the velocity of ion migration is described by the Nernst-Planck equation [11, 75]. In summary, the diffusion equation, the Nernst-Planck, Navier-Stokes, Poisson Equations can be used to describe transport processes in liquids [65, 75, 88].

The crucial part in the biosensor functioning is the chemical reactions, which occur between the different constituents and, in particular, between the receptors and the analyte molecules. Since the discovery of the double-helix structure of DNA the research on the DNA sensors has been constantly growing [1, 22, 23, 26]. The functioning principle of the DNA sensors (e.g. DNA-modified FET) is based on the hybridization of mobile DNA strands with immobilized DNA strands of known sequence to form a double-helix. The overall duplex formation, which depends on the rate of DNA transport and on the rate of the hybridization reaction, has been studied by many research groups [33, 54, 84, 85]. According to previous reports, the produced biological signal is a complex function of different effects, among them the specific and non-specific binding processes [17], hybridization of mismatched and partially matched DNA [55] etc.

As in all sensors, the most important parameter of biosensor systems is their signal-to-noise ratio (SNR). Some processes, due to their stochastic nature, result in a random signal fluctuation and, therefore, produce corresponding noise. One can distinguish between the following sources of noise, i.e. between the corresponding random processes, that appear in the BioFET [14, 40]: the thermal motion of carriers both in the semiconductor and in the electrolyte, the impurities in the conductive channel, the recombination and the generation of electron-hole pairs, the motion of the DNA strands in the electrolyte, the adsorption and the desorption of DNAs to the surface, and the hybridization and the dissociation processes. The random motion and the interaction of biomolecules produces the so-called biological noise [28, 29], which is of the main interest for our research.

The aim of this work is to provide a general mathematical concept to field-effect transistors with DNA-modified insulator-electrolyte interface. This work reports the simulation capability for the boundary layer that is crucial in the detection mechanism of the biosensors. We quantify the screening of biomolecule charge due to the counter-ions presented in the electrolyte. We identify the binding efficiency of the receptors to the DNAs of our interest. Furthermore, an approach is developed for device characterization that allows to determine the biological noise of the system and to identify the signal-to-noise ratio.

The thesis is organized as follows:

Chapter 2 summarizes the physical structure of DNAFET and gives an overview of the involved mathematical models regarding the basic components and their interactions. Here we describe the functioning of the system as a whole and suggest a corresponding segmentation for further treatment.

In Chapter 3, the Metropolis Monte Carlo algorithm in the constant voltage ensemble is extended (enhanced) for the calculation of 3D charge concentration at the charged surfaces

functionalized with PNA, single-stranded DNA and double-stranded DNA oligomers. The algorithm and all the interaction potentials between the various charge carriers are described in detail. Simulation results of the ionic charge concentrations (Na^+Cl^-) at the functionalized surface and within the inter-molecular space are also presented and discussed.

In Chapter 4, we investigate the diffusive transport of the charged biomolecules and two types of the chemical reactions near the functionalized surface, i.e. specific and non-specific binding. The well-posed problem is formulated, discretized and solved. We also present a simulation results and examine the diffusion and reaction processes as well as their interaction.

In Chapter 5, we consider the connection between different model algorithms and suggest the compilation procedures for previously segmented model. The influence of different parts on each other is presented and discussed. The result of self-consistent simulation is demonstrated as well.

In Chapter 6, we focus on the stochastic processes that occur at the functionalized surface. The chemical Langevin equation for binding (i.e. association and dissociation) processes occurring at the functionalized surface is obtained. The binding efficiency of the biomolecules, the signal and the biological noise of the device are specified and calculated. The simulation results for binding efficiency and for signal-to-noise ratio are presented, compared and analyzed with respect to the response time.

This work is based on

- A. Bulyha and C. Heitzinger, *An algorithm for three-dimensional Monte- Carlo simulation of charge distribution at biofunctionalized surfaces*, *Nanoscale*, 3(4), 1608-1617, 2011.
- A. Bulyha, C. Heitzinger, and N. J. Mauser, *Bio-sensors: Modelling and simulation of biologically sensitive field-effect transistors*, *ERCIM-news*, 85, 40-41, 2011.
- A. Bulyha, C. Heitzinger, and N. J. Mauser, *A stochastic-deterministic approach for modeling of the biological noise in the DNA-sensors*, 2011, *In preparation*.
- S. Baumgartner, A. Bulyha, M. Vasicek, N. Tassotti, and C. Heitzinger, *Investigations of optimal sensitivity for biosensors using a 3d self-consistent drift-diffusion Monte Carlo approach*, 2011, *In preparation*.

Chapter 2

DNA-modified FET

2.1 Physical structure: basic charged components

In the past decade the research in the semiconductor field-effect sensors has moved to a technology that is based on nanowires with biologically modified surface layers (biologically sensitive field-effect transistors or devices, BioFETs or BioFEDs) and a number of highly sensitive and selective devices have been developed [61, 68, 89]. The mostly common device structure is shown schematically in Fig. 2.1 and includes source (S), drain (D), backgate (G), a semiconductor layer between the source and the drain, and an insulator surrounding the transducer [67, 68].

The idea for sensing with field-effect transistors was introduced several decades ago and realized in MOSFETs (metal-oxide-semiconductor field-effect transistor). In standard devices, a semiconductor (such as silicon) is connected to metal (or polycrystalline silicon) source and drain, through which a current is injected and collected, respectively.

To control and manipulate the electrical properties of semiconductors different doping concentrations are used, i.e. the intentional incorporation of atomic impurities into material. By doping of silicon with elements, like phosphorus or arsenic, which are electron donors, the extra valence electrons are added and the transducer become an electrically conductive n-type semiconductor (n-Si). Aluminium, boron and gallium, for instance, are missing the valence electron and behave as an acceptor. Doping with these elements creates holes in the silicon lattice that are free to move. Such elements belong to p-type dopant and form an electrically conductive p-type semiconductor (p-Si).

The conductance of a MOSFET between the source and the drain is switched *on* and *off* by a voltage on the gate. Therefore, the gate electrode is a third metal contact coupled to the transducer through a thin dielectric layer. In the case of p-Si, the negative gate voltage, i.e., the negative net-charge at the interface between the transducer and the gate, leads to an accumulation of positive holes at the reverse side of this interface and generates a corresponding increase in conductance. In contrary, the positive net-charge will deplete

carriers and will lead to a decrease in the conductance. Such type of sensing is called *field-effect* and it can be used in planar [1, 56, 57] and nanowire devices [50, 51, 68]. Due to different sensitivity of planar devices and nanowires [16], the device geometry is significant in mathematical modeling.

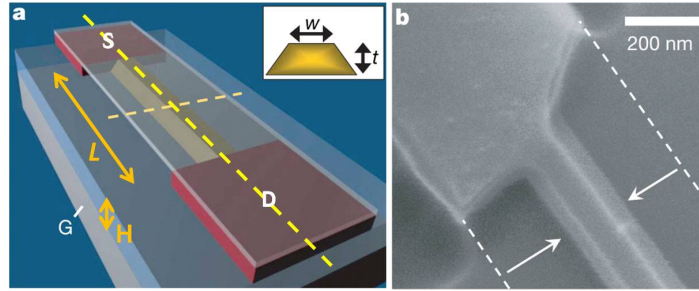


Figure 2.1: Device structure according to refs. [67,68]. (a) Schematic. The device consists of source (S), drain (D), backgate (G) and has the following parameters: $W = 50$ to 1000 nm, $t = 25$ to 80 nm, L is ca. $20 \mu\text{m}$ and H is ca. 200 nm. (b) Scanning electron micrograph.

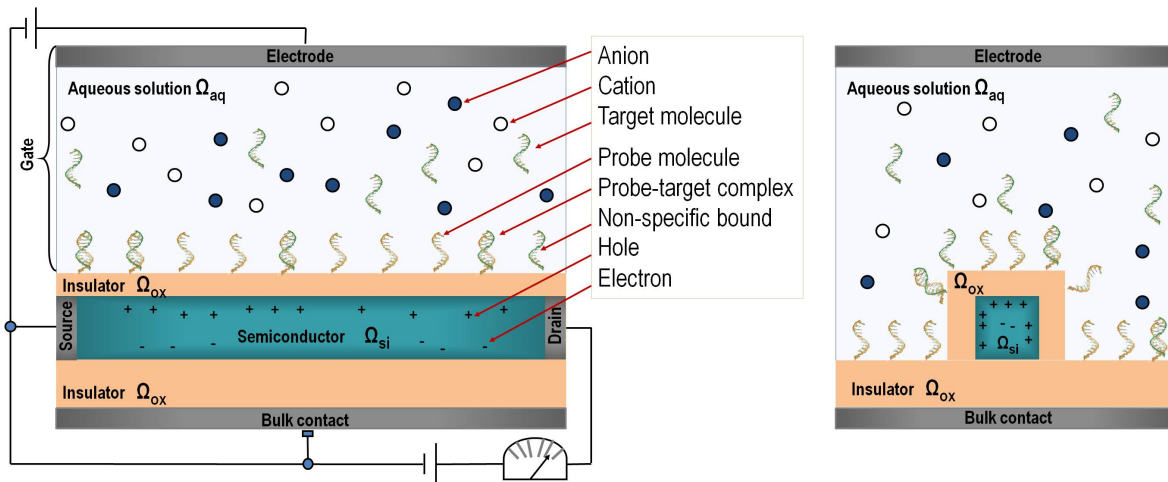


Figure 2.2: The schematic diagram of BioFETs, according to sectional views in Fig. 2.1.a.

Fig. 2.2 shows the schematic diagram of BioFETs, which consist of a semi-conducting transducer separated by an insulator layer (typically silicon dioxide or nitride) from the biological recognition element that surrounds the transducer. The biological recognition elements (simply receptors or probe molecules) are immobilized to the surface. In this work we deal with peptide nucleic acids (PNAs) and single-stranded deoxyribonucleic acids (ssDNAs). The basic idea of field-effect biosensors is similar to MOSFETs, except that the gate is replaced by an electrolyte (aqueous solution of Na^+Cl^-) containing the analyte (or target molecules) and that the external electrode is immersed in the aqueous solution. The analyte molecule is the molecule that we try to detect. It can be a DNA, an antigen, a tumor marker (protein). In our work we use ssDNAs. When the analyte biomolecules bind to the surface receptors, the charge distribution at the surface changes; that modulates the electrostatic potential in the semiconductor, and thus, its conductance.

Recent experiments have shown the possibility of detecting biomolecules by the effect of their intrinsic charge on the conductance of a semiconducting nanowire transducer [22]. However, despite the remarkable experimental progress in this field, the theoretical understanding of the field-effect sensors is still incomplete [34,37,58,61,62]. In order to achieve a quantitative understanding, a precise knowledge of the charge concentration in the surface layer is necessary; such a knowledge can up to now only be provided by simulations. Experiments have shown that it is possible to detect biomolecules through the effects of their intrinsic charges onto the conductance of a semiconductor transducer. However, a quantitative understanding of the field-effect functioning and of the crucial boundary-layer electrostatics is missing [62]. Moreover, a hybridization event is highly efficient and specific. Therefore, a deep understanding of the adsorption process of charged macromolecules onto a charged surface and of the binding of probe and target molecules are very important for sensor applications [69].

Thus, we can conclude that the modeling of such BioFET sensors must take into account the electrostatics and the geometry of the liquid, the probe and the target molecules in the boundary layer, the binding efficiency of the probes and targets, the electrostatics and the conductance of the semiconducting transducer, and the device geometry.

2.2 Mathematical models of charged BioFET-components

Let Ω be a bounded domain in \mathbb{R}^d , $d = 1, 2$ or 3 occupied by BioFET with boundary $\partial\Omega$. According to the BioFET structure [see Fig. 2.2] the total domain Ω is split into disjoint subsets $\Omega = \Omega_{Ox} \cup \Omega_{Si} \cup \Omega_{Liq}$ corresponding to the insulator (oxide), the transducer (silicon), and the electrolyte (liquid), respectively. The boundary of the domain is assumed to consist of a Neumann part and a Dirichlet part $\partial\Omega = \partial\Omega_N \cup \partial\Omega_D$, where the Dirichlet part $\partial\Omega_D = \partial\Omega_{os} \cup \partial\Omega_{od} \cup \partial\Omega_{ob} \cup \partial\Omega_{oe}$ corresponds to Ohmic contacts: source, drain, bulk contact and reference electrode.

According to the chosen device geometry the actual permittivity ε is the piecewise constant function.

$$\varepsilon(x) := \begin{cases} \varepsilon_{Ox} = \varepsilon_0 \varepsilon_1 \in \mathbb{R} & \text{in } \Omega_{Ox}, \\ \varepsilon_{Si} = \varepsilon_0 \varepsilon_2 \in \mathbb{R} & \text{in } \Omega_{Si}, \\ \varepsilon_{Liq} = \varepsilon_0 \varepsilon_3 \in \mathbb{R} & \text{in } \Omega_{Liq}, \end{cases}$$

where ε_0 denotes the permittivity of vacuum and ε_i are dielectric constants.

In our model we discern an internal electrical potential Ψ_I , which is produced by a local electric field, and a potential Ψ_E that is induced by an externally applied electric field. Thus, the total potential in the whole domain Ω is $\psi(t, \mathbf{x}) := \Psi_I(t, \mathbf{x}) + \Psi_E(t, \mathbf{x})$. We assume that the external electrical potential Ψ_E is given. The internal electrical potential Ψ_I can be

obtained via Poisson equation.

$$-\nabla \cdot (\varepsilon(\mathbf{x}) \nabla \Psi_I(\mathbf{x})) = q \varrho(\mathbf{x}), \quad \text{in } \Omega \subset \mathbb{R}^d, \quad (2.1)$$

where $\varrho(\mathbf{x})$ is a charge concentration in the whole domain Ω . In general, ϱ is a sum of fixed charge concentrations ϱ_i and the carrier distributions C_i

$$\varrho(\mathbf{x}) := \sum_i z_i \left(\varrho_i(\mathbf{x}) + C_i(\mathbf{x}) \right),$$

where i defines the species, z_i is the corresponding valence, and q is elementary charge. $C_i(\mathbf{x})$ are unknown and shall be obtained by other models.

As it is mentioned in section Section 2.1 we deal with different charged species, which can be arranged in the following categories:

in the insulator Ω_{Ox} :

- the charge of the insulator;

in the semiconductor Ω_{Si} :

- the electrons and the holes;

in the liquid Ω_{Liq} :

- the anions and the cations;
- the probe, the target molecules, the probe-target complexes and the non-specifically bounded molecules;
- the hydrogen ions.

Such partition is chosen due to significant differences in size, concentrations and motion behavior; and each category will be investigated separately.

2.2.1 Electrons and holes

First we consider the nano-electronic part with electrons and holes as charge carriers in the sub-domain Ω_{Si} , and identify two main sources for current flow:

- *diffusion* of the electrons and the holes due to concentration gradients,
- *drift* of the electrons and the holes caused by the electric potential gradient.

The total flows of the electrons and the holes are determined by the linear superposition of the diffusion and the drift processes.

Hence, the appropriate mathematical model for the transport of electrons and holes inside of the transducer is the system of the drift-diffusion equations (2.2) - (2.5) coupled to the Poisson equation. For the electron current density J_n and for the hole current density J_p in the silicon domain Ω_{Si} we use a model that has been proposed e.g. in Refs. [43, 44]:

$$\nabla \cdot J_n(\Psi_I, n) = q R, \quad (2.2)$$

$$\nabla \cdot J_p(\Psi_I, p) = -q R, \quad (2.3)$$

$$J_n = D_n \nabla n(\mathbf{x}) - \mu_n n(\mathbf{x}) \nabla \Psi_I(\mathbf{x}), \quad (2.4)$$

$$J_p = -D_p \nabla p(\mathbf{x}) - \mu_p p(\mathbf{x}) \nabla \Psi_I(\mathbf{x}), \quad (2.5)$$

where n and p are the concentrations of the electrons and the holes, the positive coefficients μ_n and μ_p are the electron and the hole mobility, respectively. The diffusion coefficients D_n and D_p are related to mobilities by Einstein's relations

$$D_n := U_{th} \mu_n,$$

$$D_p := U_{th} \mu_p.$$

U_{th} stands for the thermal voltage given by $U_{th} := k_B T / q$, where k_B denotes the Boltzmann's constant, q is the elementary charge, and T is the temperature.

The term R in the equations (2.2) and (2.3) describes difference of the rates of recombination and generation of electron-hole pairs and is called a recombination-generation rate. Recombination processes are exothermic (associated with energy release); they occur when a conduction electron becomes a valence electron and neutralizes a hole. Generation is an endothermic process (it requires energy) that occurs when a valence electron becomes a conduction electron and leaves a hole. In thermal equilibrium there is a dynamic balance between the recombination and the generation rates, i.e., $n p = n_{in}^2$.

Various energy transition processes exist, which determine the recombination-generation rate, namely, two-particle transition, three-particle transition and impact ionization. The impact ionization is a pure generation process, which occurs at a high electric field. The modeling of three-particle transition is only significant, if a high-injection condition must be investigated. In our case we assume a low electric field and a low injection, and consider only the two-particle transition process, which is described by the Shockley-Read-Hall term:

$$R = \frac{n p - n_{in}^2}{\tau_p(n + n_{in}) + \tau_n(p + n_{in})},$$

where n_{in} is the intrinsic density (i.e., in silicon at the room temperature), τ_n and τ_p are the life-times of electrons and holes, under the assumption that they are not doping-dependent. Typical values for τ_n and τ_p are 10^{-6} s and 10^{-5} s, respectively.

The performance of the semiconductor is mainly determined by its doping profile. Hence, the control of it remains very important [12]. This physical parameter can be modeled by using modern solid state physics or, according to recent publication [53], but also a direct measurement is possible. In order to control the electrical behavior of the devices, the maximal doping concentration shall be significantly larger than the intrinsic carrier concentration at the operating temperature. For simplicity we keep the dopant distribution constant so

that

$$\varrho_d + \varrho_a \gg n_{in},$$

where ϱ_d and ϱ_a denote the concentration of electrically active donor and acceptor atoms, respectively. For instance, $\varrho_{ad} := \varrho_d + \varrho_a = 2 \times 10^{18} [\text{q cm}^{-3}]$ and $n_{in} := 10^{10} [\text{q cm}^{-3}]$ for silicon at the room temperature.

We consider source and drain as Ohmic contacts and assume that the space charge vanishes, and the system is in thermal equilibrium, i.e.

$$\begin{aligned} p(x) - n(x) + \varrho_{ad} &= 0, \\ np &= n_{in}^2. \end{aligned}$$

Thus, the Dirichlet boundary condition at the Ohmic contacts is written as follows

$$\begin{aligned} n(\mathbf{x}) &= \frac{\varrho_{ad} + \sqrt{\varrho_{ad}^2 + 4n_{in}^2}}{2} & \mathbf{x} \in \partial\Omega_{os} \cup \partial\Omega_{od}, \\ p(\mathbf{x}) &= \frac{-\varrho_{ad} + \sqrt{\varrho_{ad}^2 + 4n_{in}^2}}{2} & \mathbf{x} \in \partial\Omega_{os} \cup \partial\Omega_{od}. \end{aligned}$$

The boundary potential consists of the externally applied potential Ψ_E and the potential produced by the doping Ψ_{bi} , the so-called built-in potential.

$$\Psi_I(\mathbf{x}) = \Psi_E + \Psi_{bi} \quad \mathbf{x} \in \partial\Omega_{os} \cup \partial\Omega_{od}.$$

The Ψ_{bi} is chosen in such a way that the device is in thermal equilibrium, i.e., the current density vanishes $J_n = J_p = 0$ and $\Psi_I = \Psi_{bi}$ in the equations (2.4) and (2.5), which implies

$$\Psi_{bi} = U_{th} \ln \left(\frac{\varrho_{ad} + \sqrt{\varrho_{ad}^2 + 4n_{in}^2}}{2n_{in}} \right).$$

The applied potential as well as the concentrations of the electrons and holes at the back-gate (bulk contact) and at the reference electrode are given, i.e.,

$$\begin{aligned} \Psi_I(\mathbf{x}) &= \Psi_b, & n(\mathbf{x}) &= n_b, & p(\mathbf{x}) &= p_b & \mathbf{x} \in \partial\Omega_{ob}, \\ \Psi_I(\mathbf{x}) &= \Psi_e, & n(\mathbf{x}) &= n_e, & p(\mathbf{x}) &= p_e & \mathbf{x} \in \partial\Omega_{oe}, \end{aligned}$$

where $n_b, n_e, p_b, p_e \geq 0$.

Everywhere else we use the Neumann conditions

$$\frac{\partial \Psi_I(\mathbf{x})}{\partial \vec{n}} = 0, \quad \frac{\partial n(\mathbf{x})}{\partial \vec{n}} = 0, \quad \frac{\partial p(\mathbf{x})}{\partial \vec{n}} = 0 \quad \mathbf{x} \in \partial\Omega_N,$$

where \vec{n} is the outward pointing normal vector.

2.2.2 Biomolecules

We consider an isolated sensor that is immersed into an analyte solution. The reactive solid surface $\partial\Omega_s$ of area A of the sensor is functionalized with $C_{P,0}$ receptors (probe molecules) per unit area, and the solution contains target molecules with initial concentration $C_{T,0}$ mol per liter. We will use below the notations P , T , PT for probe, target molecules and probe-target complexes, respectively. The probe-target complex PT is a molecule after hybridization event; and $C_{PT,0}$ is the corresponding initial concentration. We also denote the non-specifically bounded molecules as nT and their initial concentration as $C_{nT,max}$.

The crucial aspects of modeling are simulation of the chemical reactions at the functionalized surface and the simulation of transport of target molecules in the analyte solution to the active sensor area. There are several mechanisms, which create the flow of analyte molecules:

- *Diffusion* is random motion of molecules;
- *Convection* is caused by the bulk motion of fluids;
- *Migration* is the movement of charged particles in response to a local electric field;
- In addition, the *pump* is essential for the fast response times.

Definition 2.2.1. The net movement of molecules through a unit area per unit time in a given direction is known as a *flux*. In general, the flux is defined for any transported quantity [75].

Therefore, the total flux is $J(t, \mathbf{x}) = J_D(t, \mathbf{x}) + J_C(t, \mathbf{x}) + J_M(t, \mathbf{x})$, where J_D , J_C and J_M correspond to diffusion, convection and migration transport mechanisms, respectively.

The transport of target molecules in the analyte solution to the active sensor area must be taken into account to carry out the time-dependent simulations. In our model, the change of the concentration $C_T(t, \mathbf{x})$ of the target molecules is described by the continuum equation:

$$\frac{\partial C_T(t, \mathbf{x})}{\partial t} + \nabla \cdot J(t, \mathbf{x}) = 0, \quad \mathbf{x} \in \Omega, \quad (2.6)$$

where $J(t, \mathbf{x})$ characterizes the flow process in the analyte solution.

Chemical reactions

We consider two types of reversible chemical reactions, namely, a specific and a non-specific binding, which we can define as follows.

specific binding:

- *association* or *hybridization* is a process of binding of two complementary strands of deoxyribonucleic acid (DNA) to create a double-stranded DNA oligomers;
- *dissociation* or *denaturation* is an opposite to association process, by which double-stranded DNA oligomers separate into single strands

through the breaking of hydrogen bonds between the bases.

non-specific binding:

- *adsorption* is a direct binding of targets from the bulk phase to the surface;
- *desorption* is an opposite to adsorption process, by which the biomolecule is released from the surface.

Note that association and dissociation are more general processes, but in our case they are synonyms to hybridization and denaturation, respectively.

We assume that target molecules bind to the receptors and unbind from them with rates r_a and r_d , respectively. The rates k_a and k_d characterize the adsorption and desorption processes. Such first order reversible reactions can be depicted schematically as given by the equation below.



The hybridization depends on the density of the single (unbounded) probe molecules and on the concentration of free (unbounded) target molecules, i.e. on transport of analyte molecules to the functionalized surface; the adsorption depends on the concentration of the non-specifically bounded molecules at the maximum altitude and also on the concentration of unbounded target molecules; whereas the opposite processes are proportional to the density of the specifically or non-specifically bounded molecules, respectively. Thus, the dynamics of the binding processes is given by

$$\frac{dC_B}{dt} = (\cdot)_a C_P C_T - (\cdot)_d C_B, \quad (2.8)$$

where index B denotes PT or nT , C_i is an appropriate concentration, and pair $(\cdot)_a, (\cdot)_d$ corresponds to r_a, r_d or k_a, k_d rate coefficients, respectively.

Definition 2.2.2. The *chemical equilibrium* is understood as a balance between association and dissociation events, i.e. $\frac{dC_B}{dt} = 0$.

Definition 2.2.3. The time, during which the number of probe-target complexes reaches its chemical equilibrium value (or at least a detectable quantity), determines the *response time* of the sensor.

To describe the selectively adsorbing surface with probe molecules on it we use the Robin boundary conditions

$$\nabla C_T(t, \mathbf{x}) \cdot \vec{\mathbf{n}} = -\tilde{u}(t, \mathbf{x}, C_P, C_T, C_{PT}), \quad \mathbf{x} \in \partial\Omega_s, \quad (2.9)$$

where $\vec{\mathbf{n}}$ is the unit normal vector pointing outward to the surface $\partial\Omega$ and the function $\tilde{u}(t, \mathbf{x}, C_P, C_T, C_{PT})$ specifies chemical reactions at the surface.

For purely reflective (inert) walls we use the Neumann boundary conditions

$$\nabla C_T(t, \mathbf{x}) \cdot \vec{\mathbf{n}} = 0, \quad \mathbf{x} \in \partial\Omega \setminus \partial\Omega_s. \quad (2.10)$$

The case of a 'limited reaction', when the transport of analyte molecules is much more faster than the binding reaction (i.e., under assumption $C_T(t, 0) \approx c_0$, for instance for small sensors), is described in [65]. The solution of Eq.(2.8) in the equilibrium state is given by

$$\frac{C_{PT}(\infty)}{C_{P,0}} \equiv \frac{\hat{c}}{1 + \hat{c}},$$

where $\hat{c} = c_0 \frac{r_d}{r_a}$, irrespectively of how long the sensor takes to equilibrate.

Diffusion

We assume that there are no reaction processes far away from the functionalized surface and only elastic collisions occur between the biomolecules. Therefore, the kinetic energy and the momentum are conserved. The random nature of such collisions leads to a random motion of biomolecules and gives rise to their diffusion. The diffusion of the species in a dilute solution under the influence of a concentration gradient is governed by the Fick's first law and is expressed as

$$J_D(t, \mathbf{x}) := -\mathbf{D}\nabla C_T(t, \mathbf{x}),$$

where $\mathbf{D} := D(\mathbf{x})$ is a diffusion coefficient or diffusivity. In general, the diffusivity is a function of space and depends on the temperature, the pressure, the fluid viscosity, and on the type (size and shape) of the molecule. The diffusion coefficient for rod-like molecules is given in Section 4.3.

Convection

The bulk motion of fluid causes also the motion of biomolecules. Such convective flux is proportional to the hydrodynamic velocity field $\boldsymbol{\nu}$ and is given as follows

$$J_C(t, \mathbf{x}) := \boldsymbol{\nu}C_T(t, \mathbf{x}).$$

Definition 2.2.4. The fluid is *compressible* if the change in pressure or temperature results in a change in density. In the *incompressible* fluid the density is constant, i.e. $\rho = \text{const.}$ The *fluid density* is defined as mass per unit volume $\rho = m/V_u$.

From the second Newton's law $m \mathbf{a} = \mathbf{F}$ applied to a unit volume we obtain the equation of motion according to used model for fluid. The vector \mathbf{a} is a fluid acceleration that includes

the velocity change with respect to time and the convective acceleration, and is given by $\mathbf{a} = \frac{\partial \nu}{\partial t} + \nu \cdot \nabla \nu$. \mathbf{F} is a sum of forces, which are applied to the body and the surfaces. The body forces act on the body and include gravity F_g and electromagnetic forces F_e . Electromagnetic forces occur when an electromagnetic field interacts with electrically charged particles. The surface forces act on the surface of the control volume and include pressure F_p and viscous stress F_v . The forces are expressed as

$$\begin{aligned} F_g &= \rho g V_u, \\ F_e &= F_c = -\rho E V_u = \rho \nabla \psi V_u, \\ F_p &= -\nabla p V_u, \\ F_v &= \nabla \cdot v_s V_u, \end{aligned}$$

where g is the gravitational acceleration, E is the applied electrical field, ρ is the charge density, p is the pressure, and v_s is the viscous stress tensor. Here F_c is the Coulomb force. For incompressible Newtonian fluid with viscosity μ_f holds $\nabla \cdot v_s = \mu_f \Delta \nu$.

Hence, the velocity field ν for incompressible Newtonian fluid in applied electrical field is governed by the following Navier-Stokes equation

$$\rho \frac{\partial \nu(t, \mathbf{x})}{\partial t} + \rho \nu(t, \mathbf{x}) \cdot \nabla \nu(t, \mathbf{x}) = \mu_f \Delta \nu(t, \mathbf{x}) + \rho g + \rho \nabla \psi(t, \mathbf{x}). \quad (2.11)$$

where $\rho = q(C_1 - C_2)$, q is the elementary charge, while C_1 and C_2 are concentrations of cations and anions, respectively.

Under the assumption that the step in space is proportional to the biomolecule length and is much larger than the radius of the fluid molecules, we can use the Neumann boundary condition

$$\nabla \nu(t, \mathbf{x}) \cdot \vec{\mathbf{n}} = 0, \quad (2.12)$$

where $\vec{\mathbf{n}}$ is the unit normal vector pointing outward to $\partial \Omega_{Liq}$.

Migration

Because the DNAs are charged molecules, their transport is influenced by the internal as well as by the external electric field. The internal electrical field arises due to the differences in ion concentrations and from the accumulation of charges at the active surface layer. The flux J_M is a product of the concentration and the velocity of migration $J_M = C_T v_m$.

The velocity can be obtained from the drag forces $F_d = N_A f_d v_m$, where N_A is Avogadro's number, and f_d is the *friction drag coefficient*. For a sphere of radius r this coefficient is well known and is equal to $f_d = 6 \pi \mu_f r$. Otherwise, the friction drag coefficient is inversely proportional to diffusivity $f_d = k_B T/D$, where k_B is the Boltzmann constant, and T is the temperature. The absolute value of the drag forces is equal to those of the electric forces

acting on a mol of ions, but their directions are opposite.

$$F_d = -F_e = -z_T q N_A \nabla \psi,$$

where z_T is the net charge on the target molecule.

Hence, the transport of the biomolecules is proportional to the electrical potential gradient $\nabla \psi(t, \mathbf{x})$, where the total potential ψ is given as above $\psi(t, \mathbf{x}) := \Psi_I(t, \mathbf{x}) + \Psi_E(t, \mathbf{x})$.

$$J_M(t, \mathbf{x}) := -D \frac{z_T q}{k_B T} C_T(t, \mathbf{x}) \nabla \psi(t, \mathbf{x}),$$

where $D > 0$, z_T , q , k_B and T are the diffusivity, the net charge on the target molecule, the elementary charge, the Boltzmann constant and the temperature, respectively.

All these processes shall be taken into account in the development of the algorithms for the diffusion-convection-migration (DCM) problem with chemical reactions near the functionalized surface.

Pumps

The precise control of the transport of biomolecules is required to achieve a fast response times of biosensor. According to recent publications, different types of the integrated micro-pumps have been developed for flow modulation in microfluidic systems. The pumps are based on monitoring of the pressure [15] or the temperature [59] gradients, or of the electric field [88]. Pumps can also create the flow by stirring. In particular cases the pumps can maintain the given constant flow rates; in other cases the fluid speed is uncontrolled (in literature such pumps are sometimes denoted as mixers). In the case of an embedded pump we can localize the dominant process and simplify the problem, e.g., for the embedded mechanical pump we can assume that the stirring is a dominant process and, therefore, the velocity ν is given and it is constant in time.

In general, the velocity field should be calculated dependent on the modeled pump and the properties of the used fluid.

2.2.3 Electrolyte ions

A crucial aspect of the modeling is the calculation of the charge distribution in bio-functionalized surface layers. The standard continuum model is the mean-field Poisson equation, in which the free charges are treated as points and included in the model via Boltzmann statistics.

$$-\nabla \cdot (\varepsilon_{Li q}(\mathbf{x}) \nabla \Psi_I(\mathbf{x})) = q \left(\rho_s(\mathbf{x}) + \sum_i z_i C_i^\infty e^{-z_i \beta (\Psi_I - \Phi_F)} \right) \quad \text{in } \Omega_{Li q},$$

where $\varrho_s(\mathbf{x})$ is the charge density near the functionalized surface, i defines the species type, C_i^∞ is the bulk concentration of the species i , z_i is the corresponding valency, $\beta = q/(k_B T)$, q is the elementary charge, and ε_{Liq} is the actual permittivity. Φ_F corresponds to the Fermi level.

The classical Poisson-Boltzmann theory is successfully used to study the planar electric double layer and the electrolyte bulk. In our case the charge density $\varrho_s(\mathbf{x})$ has to be carefully modeled.

To calculate the motion of the analyte molecules we can also use the model that has been described before for the target molecules with corresponding concentration and diffusivity. In this case the boundary conditions given in (2.12) should be modified to include the geometry of the biomolecules.

According to the recent experimental results [4, 72] and simulations [66, 76], both the electrostatic and the hard-sphere collisions are sensitive to the ion size. It is also essential to consider mixed-valence ionic systems, since the electrolyte is usually buffered. Because the applied voltage between the electrodes and the bulk concentrations of the ions are controlled in experiments, their influence on the ionic concentrations has also to be investigated. The Metropolis Monte Carlo (MMC) algorithm in the constant-voltage ensemble is the appropriate numerical method, which requires the description of the complex chemical systems in terms of a realistic atomic model, the computation of the interaction forces and the minimizing of the energy.

Input parameters:

- type of the biomolecules and their length;
- angle between biomolecule and surface;
- length of linkers;
- type (radius and valence) of the electrolyte ions and their minimum number in the box;
- concentration of the used ions;
- minimum height of box;
- number of molecules at the surface;
- distance between them;
- type (charge) of the insulator;
- pH-value of water;
- initial value of chemical potential;
- applied potential.

MMC algorithm:

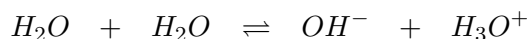
1. Construct the simulation box:
 - adapt height and width of box with account to the chosen input parameters;
 - put the biomolecules and the linkers on their places.
2. Build a random state of the system:
 - put every electrolyte ions onto a random place in the box.

3. Generate randomly a new state of the system by changing the placement of ions in the simulation box:
 - by translation of the ions inside of the box;
 - by insertion or deletion of ions;
 - by transferring a random amount of charges between the electrodes.
4. Propose the new state as a follow-up of the current state.
5. Recalculate the chemical potential if it is necessary.
6. Calculate the change in the energy of the system dE (energy difference), which is caused by the movement of charges.
7. If the move would bring the system to a state with lower energy (i.e., $dE < 0$) the new state will be unconditionally accepted; otherwise the move will be allowed with a certain probability.
8. To calculate the chemical potential μ :
 - repeat step 2-7 until $|\mu_{new} - \mu_{old}| \leq \delta \ll 1$.
9. To calculate the charge distribution of ions:
 - repeat step 2-7 with fixed chemical potential
 - until the desired (required) smoothness of the calculated charge profiles is achieved.

In the case of DNAFET, we can construct arbitrary single- and double-stranded oligomers of B-DNA as left-handed helical molecules with Watson-Crick base pairs, which have the anti-parallel organization of the sugar-phosphate chains. We assume that the partial charges of the backbone are given and calculate the atomic coordinates of base pairs by using the data from [80]. The charge of the sugar-phosphate backbone can be also calculated by using the GROMACS package [78]. Each oligomer is bound to the surface by a linker. The PNA and DNA oligomers and their linkers are modeled as impenetrable cylinders with two hemispheres of the same radius at the top and at the bottom. PNA oligomers are modeled by uncharged cylinders, and ssDNA and dsDNA oligomers carry the charges of the phosphate groups of the backbone on their outside just as in B-DNA oligomers. The linkers are orthogonal to the surface so that they touch the surface. The upper hemisphere of the linker overlaps with the lower hemisphere of the oligomer and acts as a flexible joint. Hence the oligomers can be rotated with respect to the surface.

2.2.4 Hydrogen ions

According to the acid-base theory, the water molecule can act both as a base and as an acid ion, i.e. the water molecule is able to gain a hydrogen ion H^+ or to lose it. Hence, two molecules of water dissociate into hydronium (H_3O^+) and hydroxide (OH^-) ions:



This process is known as self-ionization reaction. The concentration of hydroxide ions is specified by the pH-value, so that

$$C(H^+) C(OH^-) = 10^{-14},$$

where C denotes the concentration. The same ionization processes, which occur at the insulator-electrolyte interface, induce the charge of the insulator.

To describe such reactions we use the site-dissociation theory [5, 79]. Fig. 2.3 shows a schematic representation of the site-dissociation model, where the positively and negatively charged sites (or donors and acceptors) are produced during the association and dissociation processes that occur at the oxide-liquid surface. It is assumed in this model that the surface

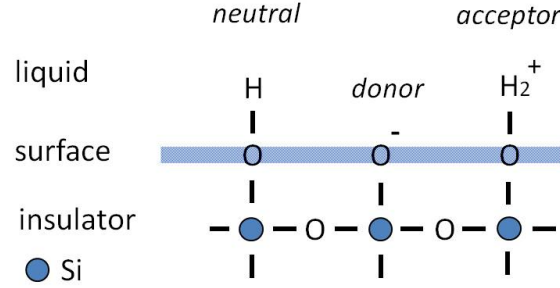
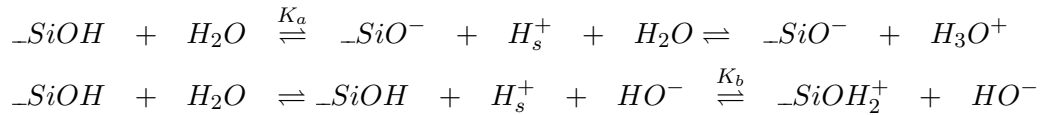


Figure 2.3: Schematic diagram of association/dissociation processes at the insulator-electrolyte interface, during which the positively and negatively charged sites (or donors and acceptors) are produced.

sites are involved in the chemical reactions: the discrete site can associate with hydrogen ion (basic reaction) or can dissociate the hydrogen ion (acidic reaction). With an example of silicon dioxide SiO_2 these chemical reactions can be written as follows



where $_SiOH$, $_SiOH_2^+$ and $_SiO^-$ denote neutral, positively and negatively charged sites, and hydrogen ions H_s^+ are located near surface. This process is controlled by the association K_a and the dissociation K_b parameters, which are measured experimentally. They can be also obtained from the equations of the acidic and the basic reactions as follows

$$K_a = \frac{[_SiO^-][H_s^+]}{[_SiOH]} \quad \text{and} \quad K_b = \frac{[_SiOH_2^+]}{[_SiOH][H_s^+]}. \quad (2.13)$$

Under concentration we understand in this section the number of sites (or ions) per surface

area and denote it as $[\cdot]$. Thus, the concentration of hydrogen ions at the surface is

$$[H_s^+]^2 = \frac{K_a}{K_b} \frac{[-SiOH_2^+]}{[-SiO^-]}.$$

Therefore, the net surface charge ϱ_s is the difference of the concentrations of acceptors and donors multiplied by the elementary charge q

$$\varrho_s = q ([-SiOH_2^+] - [-SiO^-]). \quad (2.14)$$

Note that the surface is not charged if the equation $[H_s^+]^2 = \frac{K_a}{K_b}$ holds.

The total number of sites per unit area N_s is the sum of the concentrations of all binding types

$$N_s = [-SiOH] + [-SiOH_2^+] + [-SiO^-]. \quad (2.15)$$

The relation between hydrogen ions at the surface and in the bulk is given by the Boltzmann equation.

$$\begin{aligned} [H_s^+] &= [H_b^+] e^{-\beta\psi_s}, \\ \ln[H_b^+] - \ln[H_s^+] &= \beta\psi_s, \end{aligned}$$

where $\beta := q/k_B T$, q is the elementary charge, k_B is the Boltzmann's constant, T is the temperature, and ψ_s denotes the potential difference between the surface and the bulk of the liquid. If we combine equations (2.13) - (2.15) with the Boltzmann equation we obtain the equation for the surface potential

$$\begin{aligned} \ln[H_b^+] - \ln \sqrt{\frac{K_a}{K_d}} &= \beta\psi_s + \frac{2}{e^w - e^{-w}}, \\ 2.303 \left(\log_{10}[H_b^+] - \log_{10} \sqrt{\frac{K_a}{K_d}} \right) &= \beta\psi_s + \sinh^{-1} w, \end{aligned}$$

where

$$w = \frac{\varrho_s}{2qN_s} \sqrt{\frac{1}{K_a K_b}}$$

Next we use the facts that the negative logarithm of base 10 of hydrogen ion concentration is given as pH value and the isoelectric point pI is the pH at which a surface carries no net electrical charge, i.e. $[-SiOH_2^+] = [-SiO^-]$. These parameters are determined as follows

$$pH := -\log_{10}[H_b^+] \quad \text{and} \quad pI := -\log_{10} \sqrt{\frac{K_a}{K_d}}.$$

Using linearized Gouy-Chapman-Stern model we can approximate the surface charge as $\varrho_s = \psi_s \Upsilon_{DL}$, where $\Upsilon_{DL} = 20\mu\text{Fcm}^{-1}$ is the double layer capacitance.

Hence, we can simplify the equation

$$2.303 \left(pH - pI \right) = \beta \psi_s + \sinh^{-1} \frac{\psi_s}{\beta \gamma}, \quad (2.16)$$

where $\gamma := \frac{2qN_s\sqrt{K_aK_b}}{\beta\Upsilon_{DL}}$.

On the other hand, γ is a measured parameter and determines the ψ_s to pH relation. According to [5] the value of $\gamma = 0.14$ has been experimentally determined for SiO_2 . The isoelectric point for silicon dioxide is about $pI \approx 2.2$. Therefore, the insulator-electrolyte interface is negatively charged if $pH > 2.2$.

2.2.5 Insulator

According to the site-dissociation theory we assume that the insulator is charge-neutral in Ω_{Ox} and is charged at the insulator-electrolyte interface $\partial\Omega_{Ox}$. Thus, the homogeneous Laplace's equation holds in the insulator layer

$$-\varepsilon_{Ox}\Delta\Psi_I(\mathbf{x}) = 0, \quad in \quad \Omega_{Ox},$$

with a constant charge at the insulator-electrolyte interface

$$-\varepsilon_{Ox}\Delta\Psi_I(\mathbf{x}) = q \varrho_{Ox}, \quad on \quad \partial\Omega_{Ox}.$$

We use the Neumann conditions for the inert boundary

$$\frac{\partial\Psi_I(\mathbf{x})}{\partial\vec{n}} = 0, \quad on\partial\Omega_N,$$

where \vec{n} is the outward pointing normal vector.

2.3 Conclusions

The modeling of BioFET sensors is complicated by the fact that they comprise a biophysical (biomolecular) and a nano-electronic parts with different length scales. The microscopic scale is governed by the length of single biomolecules, which are typically in the range of a few to some dozen nano-meters. The macroscopic scale is defined by the dimensions of the whole sensor, which is larger by several orders of magnitude. Therefore, solving of the Poisson equation is not possible in the whole domain. Both parts have to be considered separately and then coupled together in a self-consistent manner.

According to the considerations made in Section 2.2.2 - Section 2.2.4 the biophysical part of the biosensor can be described by coupling the Poisson equation, the Navier-Stokes equations and the diffusion-convection-migration problem with reactive boundary conditions in k -dimensional parameter space. In this case we deal with time-varying boundaries. Because

the electrolyte solution is always buffered with other ions to keep the pH-value constant, the parameter space will be larger than eight, i.e., $k > 8$. Due to the large number of unknowns and complicated boundary conditions it is necessary to consider separately the transport of biomolecules and the movement of electrolyte ions.

The Metropolis Monte Carlo method in constant-voltage ensemble can be used to investigate the ionic concentrations near the groups of charged objects with various geometries and sizes. Because the commonly used concentration of the electrolyte varies from 1M to 10^{-3} M the numbers of the electrolyte ions and the hydrogen ions can differ by several orders of magnitude. Therefore, the simultaneous application of the MMC algorithm for both types of ions requires a very large simulation box or, otherwise, leads to unsatisfactory statistics. Thus, the contribution of the hydrogen ions to our model shall be calculated separately.

To simplify the model it is useful to reformulate the DCM problem to one-parameter space and to rewrite the time-dependent boundary conditions to suitable Neumann and (or) Dirichlet boundary conditions. Depending on the geometry of the microfluidic channel and the sensor, the one-, two-, or three-dimensional version of the equations should be selected.

Chapter 3

Electrolyte solution in the equilibrium state

The standard continuum model for the electrostatics of biomolecules is the mean-field Poisson equation with a Boltzmann term for the concentration of the mobile charges, then called the Poisson-Boltzmann equation [13, 63, 70]. In this continuum model the mobile charges are treated as point charges and included using Boltzmann statistics. The classical Poisson-Boltzmann theory is successful to study the planar electric double layer and the electrolyte bulk. Also various modifications of the Poisson-Boltzmann approach have been developed and applied to study the electric double layer around a uniformly charged spherical colloid particle [49] and around an infinitely large and uniformly charged cylinder [39].

However, there are experimental results which show the effect of ion size on diffusion in alkali halides [4] (e.g., NaCl) or at the surface [72] that cannot be explained by Poisson-Boltzmann theory. Also recent simulations [66, 76, 77] show that both the electrostatic and hard-sphere collisions are sensitive to ion size. To include the finite-size effects of small ions, various methods have been developed. These include canonical and grand canonical Monte Carlo (MC) simulations [3, 42, 46, 74] and density-functional theory [9, 76]. The advantages and disadvantages of such methods for mixed-sized ions systems are discussed in the literature [7, 9, 76, 83]. MC simulations agree better with experimental data since the finite size of the ions is taken into account.

Although electrical double layers have been extensively studied near planar, uniformly charged surfaces [6, 36, 74] and around isolated, infinitely large and uniformly charged cylinders [25, 82, 83], the ionic concentrations near groups of charged objects with various geometries and sizes at surfaces have been investigated much less.

Since field-effect sensors are extremely sensitive to screening effects and the voltages are applied across the devices in experiments, correct boundary conditions must be used in self-consistent simulations. Furthermore, in experiments very low ionic concentrations are used. To arrive at good statistics in MC simulations, this implies that a large simulation domain

must be used. Since the distance between biomolecules is also small in experiments [54], this requires the capability to include several molecules in a single simulation domain (see Fig. 1). Additionally, since the electrolyte is usually buffered, it is essential to consider not only mixed-size, but also mixed-valence ionic systems. Therefore the valence of the ions can be specified as an input parameter in the MC algorithm. Finally, to calculate the electrostatic free energy of various orientations of the biomolecules [31, 70], the PNA and DNA strands can be rotated in the MC algorithm.

These requirements were taken into account in the development of the Metropolis Monte Carlo (MMC) algorithm and hence this work solves the problem of simulating the electrostatics of biofunctionalized surfaces at the microscopic scale for sensor applications.

3.1 Atomistic model

The classical MMC algorithm is extended to include the effects of biomolecules such as PNA, ssDNA, and dsDNA on ionic charge distributions near charged boundaries in an electrolyte. We treat the constant-voltage ensemble as an extension of the grand-canonical ensemble, i.e, the voltage applied to the electrodes is a controlled parameter. Another parameter that has to be constant during the simulation is the bulk ionic concentration. This is achieved using the chemical potential energy, which has to be calibrated using the iterative algorithm described below.

3.1.1 Simulation domain

The simulation domain (see Fig. 3.1) consists of a finite box $[-W, W] \times [-W, W] \times [-H, H]$ with $H \geq 2W$ that is bounded in the z -coordinate by two sheets. The interior of the box contains an electrolyte solution and one or more immobile (macro-)molecules arranged in a Cartesian grid. It is reasonable and convenient to take periodic boundary conditions in the x - and y -directions which are parallel to the sheets. The box has hard, impenetrable walls at $z = -H$ and $z = H$ carrying uniform surface charge of densities ρ and 0, respectively. Two additional charge densities σ_1 and σ_2 are associated with the sheets and are adjusted to the desired potential difference. If there is one molecule, it is linked at the center of the lower wall at $(0, 0, -H)$. If the box contains more molecules, they are arranged in an equidistant grid and each molecule is centered in its grid cell.

The box confines N_1 cations (e.g., Na) with charge q_1 , N_2 anions (e.g., Cl) with charge q_2 , and N_3 partial charges of the molecule with charges $q_{3,i}$ (e.g., the phosphate groups of the DNA backbone). It is required that the whole system is electrically neutral, i.e.,

$$4W^2(\sigma_1 + \sigma_2 + \rho) + N_1q_1 + N_2q_2 + \sum_{i=1}^{N_3} q_{3,i} = 0.$$

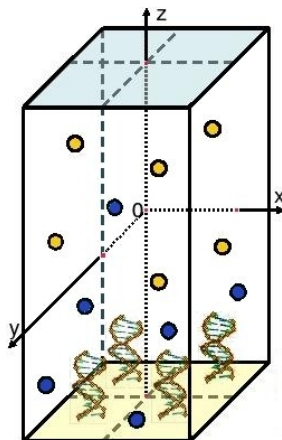


Figure 3.1: The simulation domain. Here it contains 2×2 biomolecules.

All types of ions are modeled as charged hard spheres with a diameter of 0.3nm and water is considered as a continuous structure-less medium with a constant relative permittivity of $\epsilon_r = 80$. To speed up electrostatics calculations, it is furthermore assumed that $\epsilon_r = 80$ everywhere in the simulation box. The minimal separation between ions and the boundaries is $l = 0.1\text{nm}$. The temperature of the system is $T = 300\text{K}$.

In this work the PNA, single-stranded DNA, and double-stranded DNA oligomers are modeled as impenetrable cylinders with two hemispheres at the top and at the bottom. The oligomers have ten base pairs (each base pair has a height of 0.34nm) and a radius of 1nm. They are bound orthogonal to the surface so that a hemisphere touches the surface. The PNA oligomers are uncharged in the model, whereas the ssDNA and dsDNA oligomers carry point charges of one electron charge at the location of each phosphate group of their backbones. Thus the partial charges are distributed along a helix or a double helix in the right rotational direction with a distance from the cylinder surface equal to the oxygen atom radius of 60pm.

3.1.2 Metropolis Monte Carlo simulation in the constant-voltage ensemble

The simulation samples the configuration space by randomly changing the placement of ions in the simulation box while avoiding overlaps [45, 46] and by transferring a random amount of charge between the sheets [36].

In the sequel we use the notations of Ref. [3]. In the canonical ensemble (i.e., N , V , T are constant), we denote the partition function for a system of N particles from the same species (the anions or the cations) in a volume V at temperature T by Q_N and we denote the total energy of the system in state N by E_N . The partition function Q_N can be factorized into a product of kinetic (ideal gas) and potential (excess) parts,

$$Q_N = Q_N^{\text{ig}} Q_N^{\text{ex}} = \frac{V^N}{N! \Lambda^{3N}} Q_N^{\text{ex}}, \quad (3.1)$$

where the volume V is $8(W-l)^2(H-l)$ and Λ is the thermal de-Broglie wavelength of the particles in an ideal gas at the specified temperature, i.e., $\Lambda = \sqrt{h^2/(2\pi mk_B T)}$. The excess part in the canonical ensemble is

$$Q_N^{\text{ex}} = V^{-N} \int e^{-\beta E_N(\mathbf{r})} \mathbf{d}\mathbf{r}.$$

We denote the difference in electrostatic potential energy between two configurations by U_{tot} and the chemical potential energy by μ . (To simplify notation we write U_{tot} instead of ΔU_{tot} in the following.) As usual T denotes the temperature, k_B the Boltzmann constant, and $\beta := 1/(k_B T)$. The probability that the system occupies state N is $p_N = Q_N^{-1} \exp(-\beta E_N)$ and therefore the ratio of the probabilities of the old state N and the new state M can be written as

$$\frac{p_N}{p_M} = \nu e^{-\beta \Delta E},$$

where $\nu := Q_M/Q_N$ and $\Delta E := E_N - E_M$ depends on the ensemble of the system. The transition to the next configuration is possible by four processes and is chosen with the following probabilities $P = p_N/p_M$:

- (1) translation of an ion with probability $P = \min(1, e^{-\beta U_{\text{tot}}})$,
- (2) insertion of an ion with probability $P = \min(1, \nu e^{-\beta U_{\text{tot}} + \beta \mu})$,
- (3) deletion of an ion with probability $P = \min(1, \nu e^{-\beta U_{\text{tot}} - \beta \mu})$, and
- (4) charge transfer between the two sheets with probability $P = \min(1, e^{-\beta U_{\text{tot}} + \beta A \Phi \hat{\sigma}})$.

In case (1), the translation of an ion, the temperature T , the number of the ions ($N = M$) and the volume of the system V are constant. Therefore, $Q_N^{\text{ig}} Q_N^{\text{ex}} = Q_M^{\text{ig}} Q_M^{\text{ex}} = Q(N, V, T)$ and hence $\nu = 1$. Furthermore the total energy of the system in a certain state is equal to the electrostatic potential in this state, i.e., $\Delta E = U_{\text{tot}}$.

In cases (2) and (3) ions are exchanged with the surrounding, but the chemical potential μ , the temperature T , and the volume V remain constant and we have

$$Q(\mu, V, T) = Q(N, V, T) \sum_N e^{\beta \mu N}.$$

Hence for the insertion of an ion we have

$$\begin{aligned} \Delta E &= \Delta U_{\text{tot}} - \mu, \\ \nu &= \frac{Q_{N+1}^{\text{ig}}}{Q_N^{\text{ig}}} = \frac{V}{(N+1)\Lambda^3}. \end{aligned}$$

Case (3), the deletion of an ion, is symmetrical to the insertion and we find

$$\nu = \frac{N\Lambda^3}{V},$$

$$\Delta E = \Delta U_{\text{tot}} + \mu.$$

In order to retain the charge neutrality of the simulation box, insertion and deletion of ions are always performed pairwise, i.e., both an anion and a cation are inserted or deleted in one step. We therefore rewrite the partition function Q_N from (3.1) for two types of particles, namely anions and cations, as

$$Q_{N_1+N_2} = Q_{N_1} Q_{N_2} = \frac{V_1^{N_1} V_2^{N_2}}{N_1! N_2! \Lambda_1^{3N_1} \Lambda_2^{3N_2}} Q_{N_1}^{\text{ex}} Q_{N_2}^{\text{ex}}.$$

This yields $\mu = \mu_1 + \mu_2$ and $\nu = \nu_1 \nu_2$, where the indices 1, 2 denote the particle species.

In case (4), the charge transfers between sheets, the voltage difference Φ between the sheets remains constant in addition to the canonical ensemble. The partition function can be written as an integral over the possible charge densities σ of the sheet,

$$Q(N, V, T, \Phi) = \int_{\sigma} Q(N, V, T) e^{\beta A \Phi \sigma} d\sigma,$$

where A is the area of the sheet. In this case we have $\nu = 1$ and $\Delta E = \Delta U_{\text{tot}} - A\Phi\hat{\sigma}$, where the charge density $\hat{\sigma}$ is transferred between the two sheets (see also Section 3.1.4). The equation $\sigma_1 = -\sigma_2$ always holds for charge densities of the sheets. Since the whole system is neutral, the number of ions is chosen so that the charge of the molecules and the surface charge ρ are compensated.

3.1.3 Chemical potential

The chemical potential μ_i of the i th species is defined as the change in the Helmholtz free energy upon insertion of a test particle, i.e.,

$$\mu_i = \left(\frac{\partial A_H}{\partial N} \right)_{N_j V T},$$

where the index means that the volume V , the temperature T , and the other particle numbers N_j ($j \neq i$) are constant. The Helmholtz free energy of the canonical ensemble is given by

$$\begin{aligned} A_H &= -k_B T \ln Q(N, V, T) \\ &= -k_B T \ln Q^{\text{ig}}(N, V, T) - k_B T \ln Q^{\text{ex}}(N, V, T) \\ &= A_H^{\text{ig}} + A_H^{\text{ex}} \end{aligned}$$

and hence the chemical potential is

$$\mu_i = \frac{\partial A_H^{\text{ig}}}{\partial N} + \frac{\partial A_H^{\text{ex}}}{\partial N} = \mu_i^{\text{ig}} + \mu_i^{\text{ex}}.$$

Therefore the excess chemical potential is the difference between the chemical potential of a given species and that of an ideal gas under the same conditions. The chemical potential of an ideal gas is given by

$$\begin{aligned} \mu_i^{\text{ig}} &= -k_B T \frac{\partial \ln Q^{\text{ig}}}{\partial N} = -k_B T \ln \frac{Q_{N+1}^{\text{ig}}}{Q_N^{\text{ig}}} = -k_B T \ln \frac{V}{N \Lambda^3}, \\ \rho_i &:= \frac{\Lambda^3 N}{V}. \end{aligned}$$

where ρ_i is the target density of the i th species. This yields

$$\mu_i = k_B T \ln \rho_i + \mu_i^{\text{ex}}. \quad (3.2)$$

The excess chemical potential μ_i^{ex} can be calculated iteratively [42] as follows. After starting with an estimated value like $\mu_i^{\text{ex}} = -1$ or $\mu_i^{\text{ex}} = 0$, in each iteration step n the value of $\mu_{i,n}^{\text{ex}}$ is calculated by

$$\mu_{i,n}^{\text{ex}} := \mu_{i,n-1} - k_B T \ln \langle \rho \rangle_n, \quad (3.3)$$

where $\langle \rho \rangle_n$ is the average particle density of the previous step.

Combining the probabilities of insertion or deletion of an ion (see Section 3.1.2) and the identity $\Lambda^3 = \exp(\ln \Lambda^3)$ with (3.2) and (3.3), we find that the probabilities do not depend on the thermal de-Broglie wavelength, i.e., $\Lambda = 1$.

3.1.4 Electrostatic potential energy

The total potential energy U_{tot} of the system can be divided into several terms due to the superposition principle and hence we can consider the interaction between each pair of charge types and calculate the corresponding potential energies separately. In the following, the indices I , S , and P denote ions, sheets, and partial charges of the molecule.

The movements of charges, resulting in changes in the potential energy terms, can be divided into three groups:

1. $U_{\text{tot}} = U_{IS} + U_{II} + U_{IP}$ by translation, insertion, or deletion of ions;
2. $U_{\text{tot}} = U_{SS} + U_{SI} + U_{SP}$ by charge transfer between the two sheets; and
3. $U_{\text{tot}} = U_{PS} + U_{PI} + U_{PP}$ by movements and deformations of the molecule.

In the following we describe the calculations of the potential energy that are required

for the probability calculation in the MC loop. The variables and their units or values are summarized in Appendix A.

The term U_{IS}

In the grand-canonical ensemble, the term U_{IS} describes charge-sheet interactions by

$$U_{IS} = -\frac{1}{2\epsilon} q_i \sigma r, \quad (3.4)$$

where q_i is a particle charge, ϵ is the permittivity, σ is the charge density of the sheet, and r is distance between the ion and the sheet, which is measured along the z -axis. We denote the elementary charge by q and the valence of an ion by $z_i = q_i/q$. To save computation time, we set $q^* := q\sqrt{\frac{\beta}{4\pi\epsilon}}$, $z_i^* := q^* z_i$, and $\sigma^* := q^* \sigma/q$. Hence the calculation for the i th ion is simply

$$\beta U_{IS,i} = -2\pi z_i^* \sigma^* r,$$

where the values z_i^* are kept in a look-up table.

The term U_{II}

The second term includes two types of Coulomb charge-charge interaction: the interaction U_{II}^C of ion i with ions inside the cell and the interaction U_{II}^{out} of ion i with its mirror images in the surrounding cells to treat the long-range contributions of the Coulomb forces [6, 74].

The term U_{II}^C is the Coulomb charge-charge interaction

$$U_{II}^C = \frac{1}{4\pi\epsilon} \frac{q_i q_j}{r},$$

between two ions in a homogeneous medium, where q_l is a particle charge and r is the distance between the ions. With the notation above we have

$$\beta U_{II,i}^C = \sum_{j,j \neq i} \frac{z_i^* z_j^*}{r}.$$

Analogously to the method described in Ref. [6] and [74], the interaction between the test particle i and an outside charged plane of size $L \times L$ carrying a uniform charge density of q_j/L^2 is written as

$$U_{II}^{out}(i, j) = U_{II}^{\infty}(i, j) - U_{II}^{in}(i, j),$$

where $U_{II}^{\infty}(i, j)$ is the potential energy of the particle i and an infinite sheet corresponding to the ion q_j . This potential energy is given by (3.4) with $\sigma = q_j/L^2$ and $r = d$. The second term is the interaction between the test particle i and an inside charged plane and is given

by

$$\begin{aligned}
 U_{II}^{\text{in}}(i, j) &= \frac{q_i q_j}{4\pi\epsilon L^2} \int_{-L/2}^{L/2} \int_{-L/2}^{L/2} \frac{dx dy}{r(x, y)} \\
 &= \frac{q_i q_j}{4\pi\epsilon L} \left(-2 \ln \left(\frac{-1 + 2\sqrt{1/2 + (d/L)^2}}{1 + 2\sqrt{1/2 + (d/L)^2}} \right) \right. \\
 &\quad \left. - 4 \frac{d}{L} \arctan \left(\frac{1}{4d/L\sqrt{1/2 + (d/L)^2}} \right) \right), \tag{3.5}
 \end{aligned}$$

where d is the distance between a particle and a plane (along the z -axis). This yields

$$\begin{aligned}
 \beta U_{II,i}^S &= \beta \sum_{j, j \neq i} (U_{II}^\infty(i, j) - U_{II}^{\text{in}}(i, j)) \\
 &= 2 \sum_{j, j \neq i} \frac{z_i^* z_j^*}{L} \left(-\pi \frac{d}{L} + \ln \left(\frac{-1 + 2\sqrt{1/2 + (d/L)^2}}{1 + 2\sqrt{1/2 + (d/L)^2}} \right) \right) \\
 &\quad + 2 \frac{d}{L} \arctan \left(\frac{1}{4d/L\sqrt{1/2 + (d/L)^2}} \right).
 \end{aligned}$$

The term U_{IP}

The term U_{IP} , i.e., the interaction between an ion and a partial charge of a molecule, is calculated analogously to U_{II} .

The term U_{SS}

In the constant-voltage ensemble, the charge density $\hat{\sigma}$ is transferred between the two sheets. We denote the distance between the sheets by d , the area of the sheets by A , and the charge densities of the sheet at $z = -H$ by σ_1 and the one at $z = H$ by σ_2 . The charge transfer between the two sheets can be described as an axially parallel transport of charge q' from an infinitesimal segment of one sheet to the corresponding segment of the second sheet.

The term U_{SS} describes the interaction between the sheet of area A and the infinite sheet. Using (3.4) with $r = d$ and $q_i = q'$ and integrating, we hence find

$$U_{SS} = -\frac{1}{2\epsilon} \sigma \hat{\sigma} A d, \tag{3.6}$$

where we have used $\int_A q' dx dy = \hat{\sigma} A$. This yields

$$\beta U_{SS} = -2\pi \sigma^* \hat{\sigma}^* A d.$$

The terms U_{SI} and U_{SP} in the constant-voltage ensemble

The charge transfer between two sheets can be treated as a decrease of the charge density by $\hat{\sigma}$ of one sheet and the corresponding increase of charge density at the second sheet. In the constant-voltage ensemble, the terms U_{SI} and U_{SP} describe the interactions between a sheet, whose charge density is changed, and a point charge q_j (the charge of an ion or a partial charge of a molecule). Analogously to the calculations for the term U_{II} , we have to take into account the long-range contributions from the rest of the boxes.

Again we split this term into the sheet-charge interaction U_{SI}^q and the interaction between the sheet (of area A) and the outside charged plane corresponding to the point charge q_j , i.e.,

$$U_{SI}(j) = U_{SI}^q(j) + (U_{SI}^\infty(j) - U_{SI}^{\text{in}}(j)).$$

Using (3.5) with $q_i = \hat{\sigma}A$, where $A = L^2$, we find

$$U_{SI}^{\text{in}}(j) = \frac{\hat{\sigma}}{4\pi\epsilon} q_j \int_{-L/2}^{L/2} \int_{-L/2}^{L/2} \frac{1}{r(x, y)} dx dy,$$

where $r(x, y) := \sqrt{x^2 + y^2 + d^2}$ and d is the distance between the sheet and the point charge.

The potential energy dU_{SI}^q of q_j due to an infinitesimal segment $dx dy$ of the sheet with charge $q' = \hat{\sigma} dx dy$ can be written as

$$dU_{SI}^q(j, x, y) = \frac{q_j}{4\pi\epsilon} \frac{\hat{\sigma} dx dy}{r(x, y)}.$$

By integrating over all infinitesimal segments we find $U_{SI}^q(j) = U_{SI}^{\text{in}}(j)$.

The interaction $U_{SI}^\infty(j)$ between the sheet of area A and the infinite sheet corresponding to the point charge q_j is found from (3.6) using a charge density of $\sigma = q_j/L^2$ for the infinite sheet. We have

$$U_{SI}^\infty(j) = -\frac{1}{2\epsilon} \hat{\sigma} q_j r,$$

where r is distance between the ion and the sheet.

Hence we finally have

$$\beta U_{SI} = -2\pi \sum_j \hat{\sigma}^* z_j^* r.$$

The terms U_{PI} , U_{PS} , and U_{PP}

In this work we assume the molecule to be rigid, and therefore we always have

$$U_{PI} = U_{PS} = U_{PP} = 0.$$

3.2 Simulation results

In the Metropolis Monte Carlo simulations we investigate surfaces functionalized with different types of biomolecules, different surface charges, and different applied voltages. In order to calculate the charge densities and the amount of screening, we consider four different situations:

- In the first situation, no molecules are present and an electric double layer is formed. This situation provides the baseline for the next simulations and a check of our simulations with the large body of work on electric double layers.
- In the second situation, an uncharged cylindrical molecule, i.e., PNA, is present. In a sensor setting this means that the surface has been functionalized, but no target molecules is present.
- In the third situation, a charged cylindrical molecule, i.e., single-stranded DNA, is present. This situation means that a strand of ssDNA has bound to the PNA from the first situation and is being detected by the redistribution of charges. It can also mean that the surface was functionalized with ssDNA and no target molecule is present yet.
- In the fourth situation, a charged cylindrical molecule with twice the amount of charge, i.e., double-stranded DNA, is present. This situation means that the probe strand from the third situation is now bound to a complementary target strand.

If we consider field-effect biosensors, the difference in the charge distribution between the second and third situations and between the third and fourth situations is crucial for the functioning of these sensors and provides the detection mechanism. In the simulations the

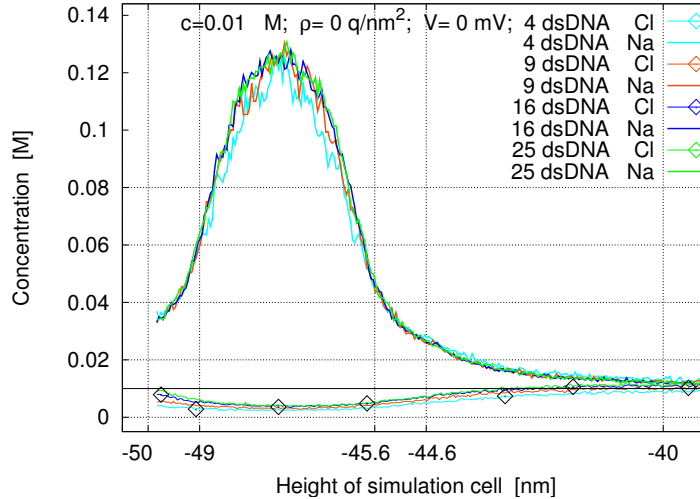


Figure 3.2: Density profiles for a 1:1 electrolyte and boxes containing different numbers of dsDNA strands under the same simulations parameters. Here and in the following figures c is the concentration of the electrolyte, ρ is the surface charge density of the sheet at -50nm , and V is the difference in the electrostatic potential between the two sheets.

sheet that corresponds to the sensor surface is located at $z = -50\text{nm}$ and the oligomers have z -coordinates in the interval $[-50, -44.6]\text{nm}$. The simulations are three-dimensional

and the concentration profiles are shown as function of the z -coordinate. In general, the simulation domain is not symmetrical around $z = 0$.

Table 3.1: Nominal simulation parameters.

Salt concentration	0.01M
Potential difference	0mV
Surface charge density	0q/nm ²
Macromolecule separation	8nm
Number of macromolecules	3 × 3

The simulation box can contain several molecules arranged in a grid. This is necessitated by the fact that low electrolyte concentrations, as they occur in experiments, require large box sizes in order to obtain reasonable results from a MC simulation. The distance between molecules, however, is also given by real-world values and can be much smaller than the box size. Therefore we developed the capability to include many molecules in a single simulation box.

Hence we first investigate the influence of the number of molecules on the resulting concentration profiles all else being equal. Fig. 3.2 shows concentration profiles for boxes containing 2×2 , 3×3 , 4×4 , and 5×5 oligomers under the same conditions. The differences in the concentration profiles are due to the slightly different approximations made during the calculation of interactions between a point charge and a sheet outside of the box (see Section 3.1.4). On the other hand, the simulation times increase significantly when the size is increased. In the following simulations we use boxes containing 3×3 oligomers and 100nm high, since this size provides results very close to the limit of an infinite box size and since at this size there are enough ions present to ensure good statistics in the MC loop.

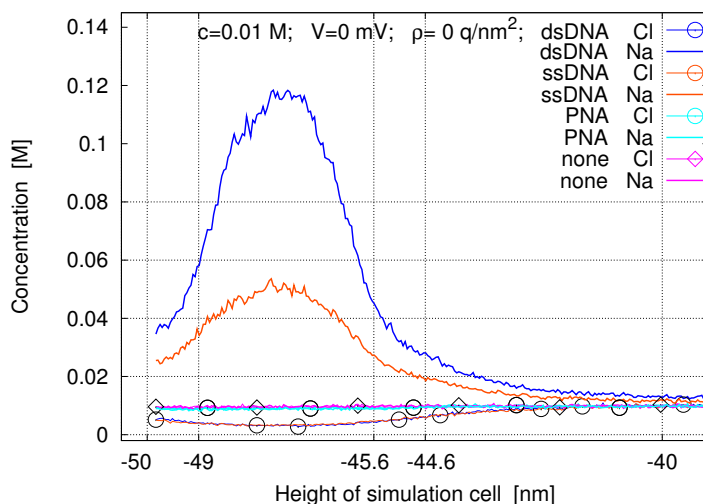


Figure 3.3: Concentration profiles for a 1:1 electrolyte for four types of macromolecules under nominal simulation parameters.

The nominal simulation parameters for all types of macromolecules are shown in Table 3.1. In what follows, the normalized surface charge density denoted by ρ is given in units

of elementary charges per square nanometer.

Concentration profiles for the nominal simulation parameters and different molecules are shown in Fig. 3.3. The small influence of the steric effect of the uncharged PNA is seen. The simulations with charged molecules show that the ionic concentration in the intermolecular space differs substantially from the bulk concentration. There is also a substantial change in charge distribution after hybridization of a second strand. Moreover the maximum value of cation concentration and the minimum value of anion concentration are reached at the middle of the molecules.

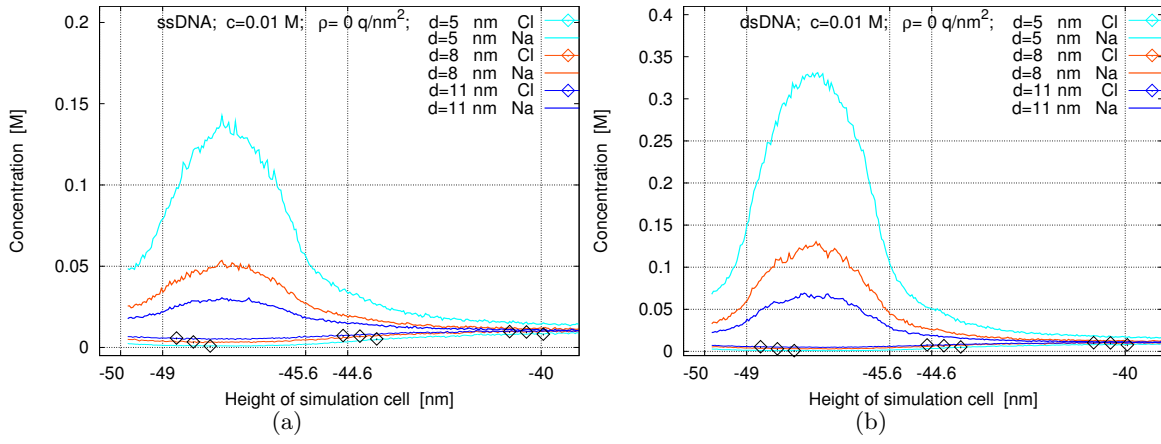


Figure 3.4: Concentration profiles for ssDNA (a) and dsDNA (b) for a surface charge density of $\rho = 0$ q/nm², for a bulk concentration of 0.01M, and with no applied voltage. The molecules are placed on grids with spacings of 5nm, 8nm, and 11nm.

The concentration of the molecules can also be varied by varying the grid spacing. In Fig. 3.4 the concentration profiles for ssDNA and dsDNA and three grid spacings of 5nm, 8nm, and 11nm are shown. The increase or decrease of the distance between the molecules leads to the expected change in the ion concentration in the intermolecular space.

Figures 3.5 and 3.6 show the ionic concentration profiles for different voltages applied across the box and for surface charge densities of $\rho = 0$ q/nm² and $\rho = -0.2$ q/nm² at the left sheet. The molecules considered are ssDNA and dsDNA.

If the left sheet is at a negative voltage (blue lines), the sodium concentration (lines without marks) at the sheet and in the intermolecular space is increased compared to the case of no applied voltage (red lines). At the same time, the chlorine concentration decreases. Fig. 3.6 quantifies how much this effect is more pronounced when there is an additional charge on the left sheet. The charge density of $\rho = -0.2$ q/nm² is the charge density of silicon oxide in water at pH = 7. It is seen that in this case the electric double layer and the charge cloud of the counter-ions of the molecules overlap. Therefore they have to be modeled self-consistently and cannot be separated: this non-trivial behavior is clearly observed in the unmarked blue lines in Fig. 3.5 and the unmarked red lines in Fig. 3.6.

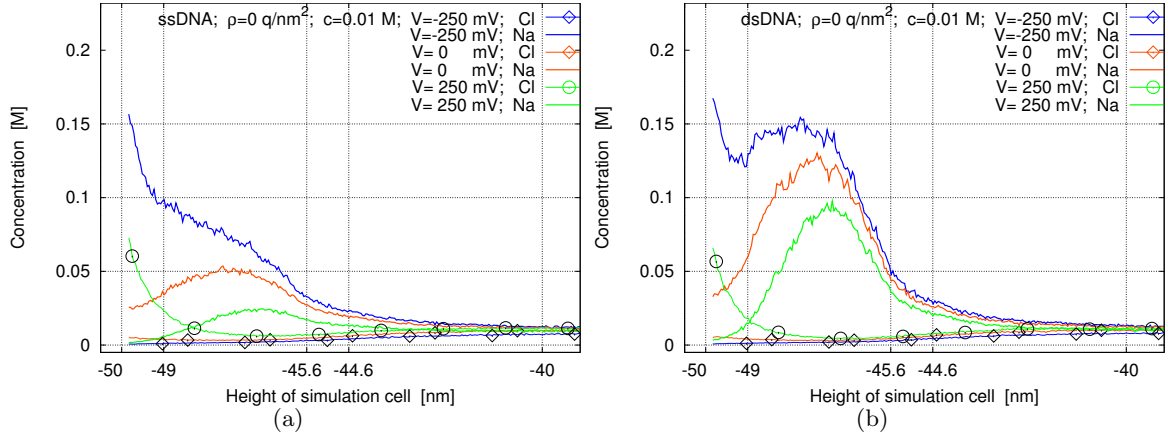


Figure 3.5: Concentration profiles for ssDNA and dsDNA for a surface charge density of $\rho = 0 \text{ q/nm}^2$ and for applied potentials of -250 mV , 0 mV , and 250 mV .

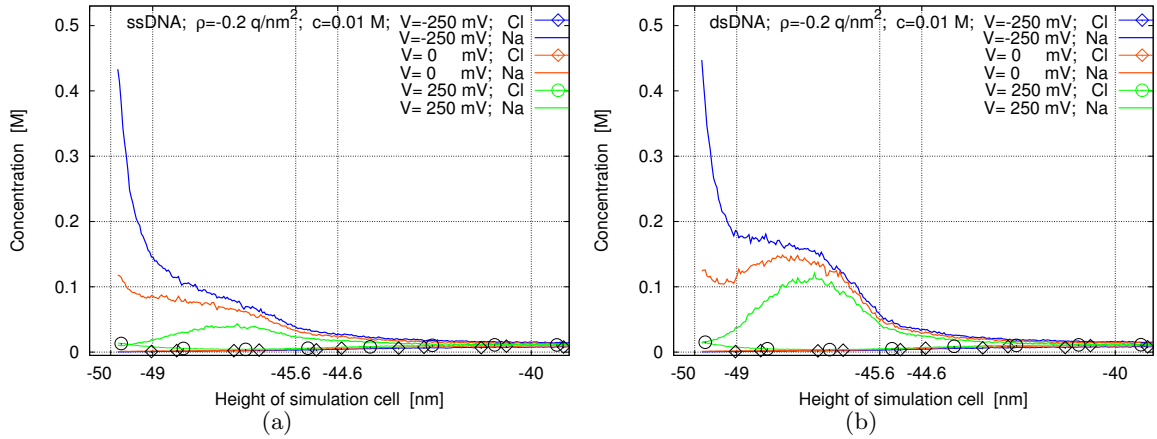


Figure 3.6: Concentration profiles for ssDNA and dsDNA for a surface charge density of $\rho = -0.2 \text{ q/nm}^2$ and for applied potentials of -250 mV , 0 mV , and 250 mV .

If the left sheet is at a positive voltage (green lines), the chlorine concentration (lines with circles) in the electric double layer at the sheet is much increased. At the same time, the concentration of the sodium counter-ions (lines without marks) in the intermolecular space is decreased compared to the case of no applied voltage (red lines). When there is an additional negative charge on the left sheet (Fig. 3.6), there is no increase of chlorine in the electric double layer. It is also worth noting that the concentration of the sodium counter-ions is increased for all applied voltages, significantly in some cases, when the surface is negatively charged compared to the uncharged case.

If there is no applied voltage, the concentration profiles for different molecules and dif-

ferent surface charge densities of the left sheet are similar to the concentration profiles shown in Fig. 3.5.

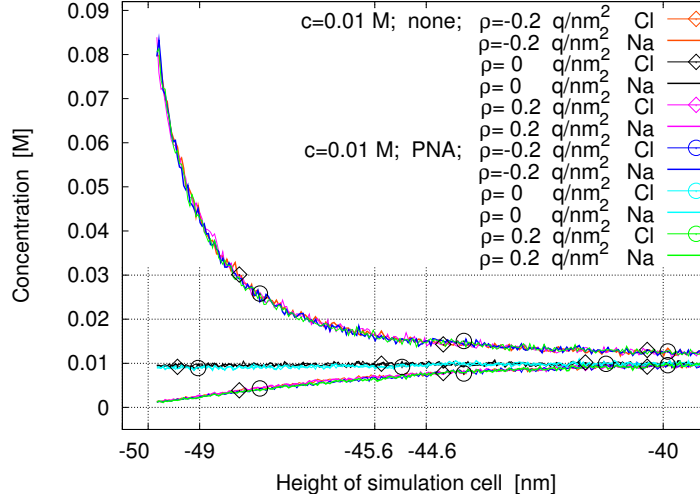


Figure 3.7: Concentration profiles for no molecules and for PNA and for surface charge densities of $\rho = -0.2q/\text{nm}^2$, $\rho = 0$, and $\rho = +0.2q/\text{nm}^2$ with no applied potential.

In Fig. 3.7 concentration profiles for no molecules and for PNA are shown. The charge density of the left sheet is varied and there is no applied potential. The formation of electric double layers at charged plates in an electrolyte is an often studied situation, although usually high electrolyte concentrations are used. [7,8,76,77] The concentration profiles of cations and anions are symmetric in both cases with respect to positive and negative surface charge densities of the sheet. This verifies the MC algorithm.

In Fig. 3.8, we next investigate the situation where a negative charge on the left sheet and the negative charge of the molecules determine the concentration profiles of the ions Fig. 3.8 (a). The charge of the sheets can be modified by an applied voltage as well (blue and red lines). If the net charge of the plate is negative and much smaller than the total charge of the DNA strands, the concentration profiles of the cations show two peaks located near the cathode and within the intermolecular space (red and cyan lines in the Fig. 3.8 a). Hence there are two areas with high cation concentration. As the charge of the cathode decreases, the second peak becomes wider until both areas overlap. The behavior of the anions is simpler: their concentration increases with increasing distance from the left sheet until it reaches the bulk concentration. If the net charge of the sheet is positive (Fig. 3.8 b), the behavior is more complicated and we can discern three layers. The first and third peaks correspond to maxima in the anion concentrations and the second peak corresponds to maxima in the cation concentrations. By increasing the surface charge, the second peak is shifted slightly away from the plate, the cation concentration in the intermolecular space is decreased, and the anion concentration in the third layer (near the bulk) becomes higher than the cation concentration.

Thus we observe a complicated behavior of three interacting layers: first, there is an

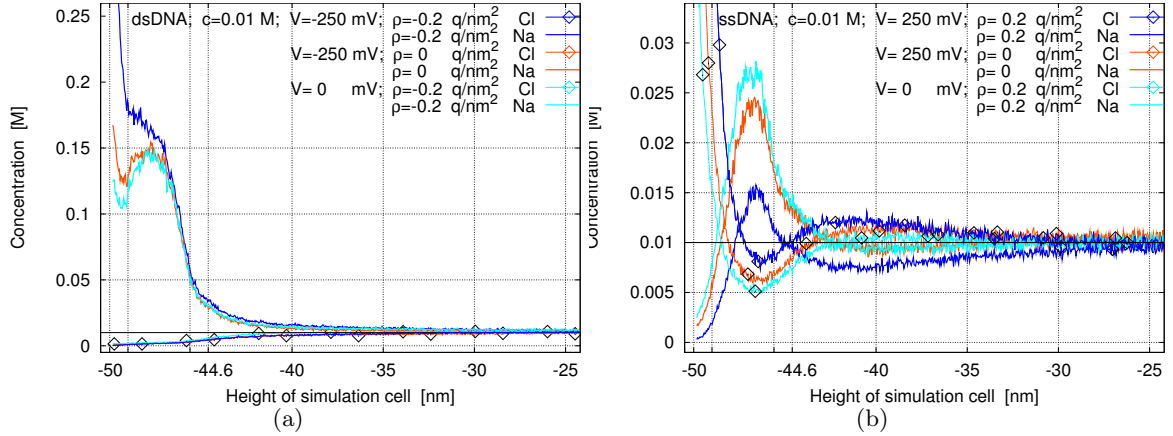


Figure 3.8: Concentration profiles for ssDNA and dsDNA for various charge densities of the left sheet and for various applied potentials.

electric double layer at the boundary; second, there is a layer caused by the molecule charges; and third, there is a boundary layer above the molecule layer and between the bulk. The third layer is effectively a double layer caused by the molecule layer.

In Figures 3.9 and 3.10 we study the modification of the concentration profiles when the electrolyte concentration is reduced from 0.02M to 0.01M and then to 0.005M. In Fig. 3.9 there is no charge on the left sheet, whereas in Fig. 3.10 the left sheet is negatively charged.

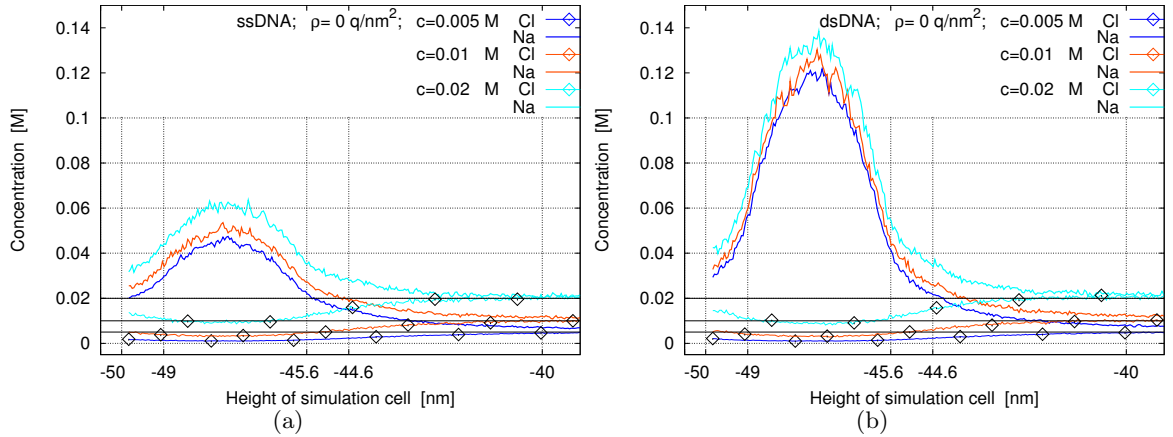


Figure 3.9: Concentration profiles for ssDNA (a) and dsDNA (b) for a surface charge density of $\rho = 0$ q/nm² and for bulk electrolyte concentrations of 0.005M, 0.01M, and 0.02M.

The simulations show that the concentration of the counter-ions around the molecules decreases slightly with decreasing bulk electrolyte concentration. In three of the four cases, the counter-ion concentrations show maxima in the intermolecular space and reach them approximately at the middle of the intermolecular space. In the fourth case, when the left

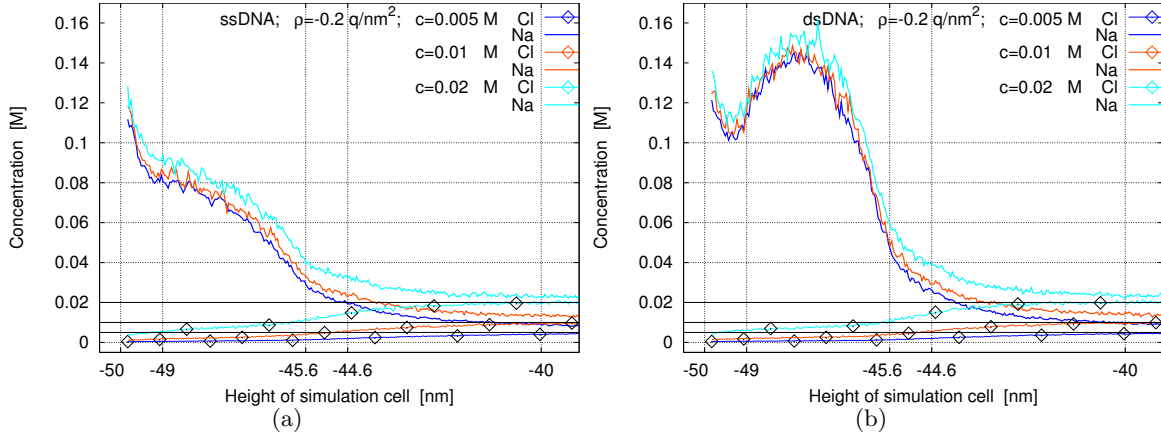


Figure 3.10: Concentrations profiles for ssDNA (a) and dsDNA (b) for a surface charge density of $\rho = -0.2 \text{ q/nm}^2$ and for bulk electrolyte concentrations of 0.005M, 0.01M, and 0.02M.

sheet is negatively charged and ssDNA is present, the concentration profiles are monotone.

The qualitative behavior of the concentration profiles in these simulations is the same regardless of the bulk electrolyte concentration. The salt concentration is an important quantitative, but not a crucial qualitative parameter in the simulations. In practice it is chosen to fulfill experimental requirements such as DNA hybridization.

3.3 Conclusions

In this chapter, the simulation capability for ionic concentration profiles at charged surfaces functionalized with molecules was developed. The model and algorithm are general enough to consider any type of charged surface functionalized with rigid molecules. The simulations are three-dimensional and a potential difference can be applied across the simulation box. The physical systems that can be simulated are, e.g., the boundary layers of (field-effect) biosensors and biomolecules at membranes. The algorithm is general enough to investigate systems with low electrolyte concentrations and high surface densities of molecules.

The model makes quantitative investigations possible: the ion concentration profiles are calculated depending on bulk electrolyte concentration and on molecule surface density and molecule charge. Important simulation results for engineering applications are the concentrations of screening charges (i.e., counter-ions) around different kinds of biomolecules. For example, it was found that the bulk electrolyte concentration determines the amount of counter-ions in a highly nonlinear manner. This work provides an essential building block for the quantitative understanding of field-effect biosensors, since it provides the understanding of the electrostatics of the crucial boundary layer.

It was found that due to the presence of the charged molecules, the ionic concentration profiles generally exhibit a three-layer structure. The first layer is the electric double layer due to the charged surface, the second layer is due to counter-ions between the molecules, and the third layer is a boundary layer above the layer of the biomolecules. The interaction between the electric double layer and the counter-ions is non-trivial and necessitates this kind of quantitative investigation that we presented.

Chapter 4

Transport of charged biomolecules with chemical reactions near the surface

4.1 Continuum model for the analyte flow

We consider the same sensor as in Section 2.1 and begin with the specification of the sensing system: the target molecules wander diffusively through the solution and bind to the probes, which are linked to the surface. In the case of a uniform viscosity, constant temperature and pressure, the diffusivity D will be independent of position. Note that the diffusivity depends in general on the type (size and shape) of the molecule. It will be described more precisely in Section 4.3. In our model we keep this parameter constant. Furthermore, we consider a non-specific adsorption of targets to the surface, where $C_{nT}(t)$ denotes a concentration for such molecules (referred further as non-specifically adsorbed molecules). For simplicity, we assume that all probe molecules are attached to the surface, and that the initial concentrations $C_{T,0}$ and $C_{P,0}$ are uniform; the initial concentration of probe-target complexes and non-specifically adsorbed molecules are equal to zero $C_{PT,0} = C_{nT,0} = 0$. In this work we focus on the selectively adsorbing boundary conditions, which are a crucial part of the modeling of the biosensors, and which are, despite of the remarkable experimental progress in this field, still not clearly understood by experimentalists. Thus, for instance, the two types of the adsorption, specific and non-specific, are not very well distinguished in the experiments.

4.1.1 Adsorption of biomolecules: specific and non-specific binding

The proposed model is based upon two mechanisms of adsorption: the direct binding of targets from the bulk phase to probe molecules and the non-specifically adsorption of target molecules to the surface. If the chemical reaction between biomolecules has an association

rate $r_a > 0$, and disassociation rate $r_d > 0$, and $k_a \geq 0$ and $k_d \geq 0$ represent the non-specific adsorption and desorption, then from the law of mass action we obtain the following relations at the surface $\partial\Omega_s$

$$\frac{\partial C_{PT}(t)}{\partial t} = r_a C_T(t, x_s) \left(C_{P,0} - C_{PT}(t) \right) - r_d C_{PT}(t), \quad (4.1)$$

$$\frac{\partial C_{nT}(t)}{\partial t} = k_a C_T(t, x_s) \left(C_{nT,max}(t) - C_{nT}(t) \right) - k_d C_{nT}(t), \quad (4.2)$$

with initial data:

$$C_{PT}(t=0) = C_{nT}(t=0) = 0,$$

where x_s is located near $\partial\Omega_s$, the terms $C_P(t) := C_{P,0} - C_{PT}(t)$ and $C_T(t, x_s) := C_T(t, x = x_s)$ describe the concentration of single probe molecules and free target molecules, respectively, i.e., those molecules, which are not bounded at the time t . $C_{nT,max}$ is a concentration of non-specific adsorption at the maximum altitude. Under the assumption that single species do not overlap, it is determined to be

$$C_{nT,max}(t) = \frac{1 - \pi R_P^2 C_P(t) - \pi R_{PT}^2 C_{PT}(t)}{\pi R_T^2} < \frac{1}{\pi R_T^2},$$

where R_P , R_T and R_{PT} are radius of probes, targets and probe-target complexes including a distance of closest approach, respectively. In the case of $R_P = R_{PT}$ the concentration is constant and equal to $C_{nT,max} = (1 - \pi R_{PT}^2 C_{P,0}) / \pi R_T^2$.

We also fix the $C_T(t, x_s) =: c^*$ in the eqns. (4.1) and (4.2). In this case the functions at the right-hand side are everywhere differentiable in C_{PT} and C_{nT} . Moreover, the absolute values of the derivatives are bounded above by $r_a c^*$ and $k_a c^*$, respectively. Thus, they are Lipschitz continuous in C_{PT} and C_{nT} and continuous in $t \in [0, T]$. According to Picard-Lindelöf Theorem the ordinary differential equations (4.1) and (4.2) with initial conditions have unique solutions, which depend on $C_T(t, x_s)$ in our case, and are given for $t > 0$ as follows:

$$0 < C_{PT}(t) = \frac{r_a C_T(t, x_s) C_{P,0}}{r_d + r_a C_T(t, x_s)} \left(1 - e^{-(r_a C_T(t, x_s) + r_d)t} \right) \leq \frac{C_{P,0}}{\frac{r_d}{r_a C_T(t, x_s)} + 1} < C_{P,0}, \quad (4.3)$$

$$0 < C_{nT}(t) = \frac{k_a C_T(t, x_s) C_{nT,max}}{k_d + k_a C_T(t, x_s)} \left(1 - e^{-(k_a C_T(t, x_s) + k_d)t} \right) < C_{nT,max}(t), \quad (4.4)$$

where $C_T(t, x_s) > \max\left\{-\frac{r_d}{r_a}, -\frac{k_d}{k_a}\right\}$ will be determined below in (4.6).

The concentrations $C_{PT}(t)$ and $C_{nT}(t)$ at the time interval $(0, T]$ are equal to zero only if there are no reaction processes, i.e., $r_a = r_d = k_a = k_d = 0$. Therefore, we assume for further considerations that $\frac{r_d}{r_a} \frac{k_d}{k_a} > 0$.

4.1.2 Model equations

Our model interconnects four types of charged biomolecules, namely, the single probe molecules, the free target molecules, the probe-target complexes and the non-specifically bounded targets; all of them with different motion behavior. The total number of molecules shall be constant at each time, i.e.,

$$\int_{\Omega} (C_P(t, \mathbf{x}) + C_T(t, \mathbf{x}) + C_{PT}(t, \mathbf{x}) + C_{nT}(t, \mathbf{x})) d\mathbf{x} = \int_{\Omega} (C_P(0, \mathbf{x}) + C_T(0, \mathbf{x})) d\mathbf{x} = \text{const}, \quad \forall t.$$

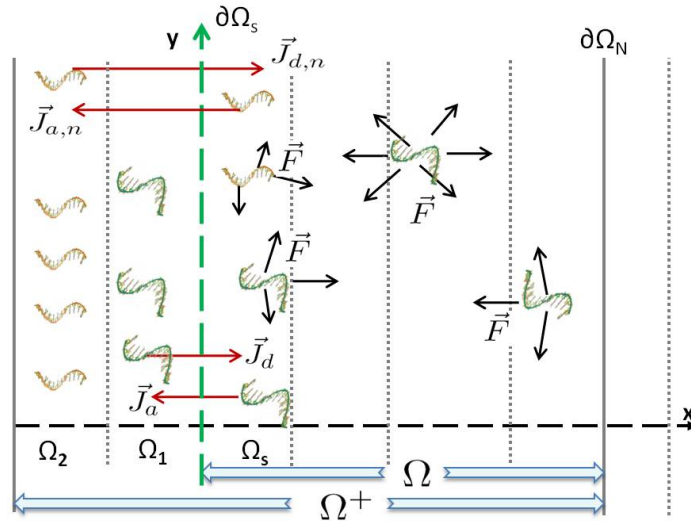


Figure 4.1: The simulation domain.

In order to satisfy the law of conservation of mass and to reduce the number of unknowns we reformulate the problem (2.6) - (2.10), (4.1) and (4.2). Let Ω be a bounded domain $\bar{\Omega} := \Omega \cup \partial\Omega$ with smooth boundary $\partial\Omega := \partial\Omega_s \cup \partial\Omega_N$, where $\partial\Omega_s$ is a functionalized surface and $\partial\Omega_N$ depicts the inert walls. Let also Ω^+ be an extended with $\Omega_1 \cup \Omega_2$ domain (see Fig. 4.1), and Ω_s be a reaction chamber, such that in the domain $\Omega_m := \Omega \setminus \Omega_s$ only processes of motion occur. We choose Ω_1 and Ω_2 in a such way so that the volumes are equal, i.e., $V_{\Omega_1} = V_{\Omega_2} = V_{\Omega_s}$. Notice that vector \vec{F} in Fig. 4.1 denotes, in general, diffusion, migration or convection processes $\vec{F} := \vec{J}_D + \delta_1 \vec{J}_M + \delta_2 \vec{J}_C$, where $\delta_{1,2} = 0$ or 1 , according to used model. In this section we investigate the reaction processes and focus on the pure diffusive flux $J_D(t, \mathbf{x}) := -\mathbf{D} \nabla C_T(t, \mathbf{x})$.

In the domains Ω_m and Ω_s the function $u(t, \mathbf{x})$ equates to the concentration of free target molecules.

$$\partial_t u(t, \mathbf{x}) = -\nabla \cdot J_D = \nabla \cdot (\mathbf{D} \nabla u(t, \mathbf{x})), \quad \mathbf{x} \in \Omega_m, \quad t \in (0, T] \quad (4.5)$$

where $\mathbf{D} = D(\mathbf{x}) > 0$ is a diffusivity.

The hybridization of targets from the bulk phase can be interpreted as molecules flow

\vec{J}_a through the surface $\partial\Omega_s$ and their accumulation in Ω_1 . The denaturation is an opposite process and is described by flow \vec{J}_d .

The reversible non-specific adsorption is depicted in our model as jump $\vec{J}_{a,n}$ to the domain Ω_2 and desorption is a backward jump $\vec{J}_{d,n}$.

We assume that the non-specifically adsorbed target molecules will bind to a single probe only after their desorption, i.e., at another time step. We also assume that the chemical reaction is one-dimensional (in x-direction) and the movement of analyte molecules is three-dimensional. We suppose that after hybridization the target can be bound to another probe molecule only after its movement to another place.

Thus, the non-specifically adsorbed targets are located in Ω_2 and the probe-target complexes are accumulated in Ω_1 , i.e., the function $u(t, x)$, $x \in \Omega_1$ or Ω_2 , is associated with probe-target complexes and with non-specifically bounded targets.

$$\begin{aligned} 0 \leq C_{PT}(t) = u(t, x_{s-1}) < C_{P,0} \quad \text{and} \quad \partial_t C_{PT}(t) = \partial_t u(t, x_{s-1}), \quad x_{s-1} \in \Omega_1, \quad t \in (0, T] \\ 0 \leq C_{nT}(t) = u(t, x_{s-2}) < C_{nT,max} \quad \text{and} \quad \partial_t C_{nT}(t) = \partial_t u(t, x_{s-2}), \quad x_{s-2} \in \Omega_2, \quad t \in (0, T] \end{aligned}$$

In such an interpretation it is enough to control the number of target molecules disregarding their state of binding. Ω_1 and Ω_2 can be simply considered as "look-up" domains for specific and non-specific binding, respectively.

Now we can argue that any interaction between single P and free T molecules at time t only occurs if $\mathbf{x}(t) \in \Omega_s$, i.e. the target and probe molecules are close to another, where $\mathbf{x}(t)$ is the location of the analyte molecule at the time t . The same assumptions we make for non-specific reactions. Let \vec{n} be a unit normal vector pointing outward to the surface. In the domain Ω_s the flows \vec{J}_d and \vec{J}_a have opposite directions, i.e., $\vec{J}_a \cdot \vec{n} > 0$, $\vec{J}_d \cdot \vec{n} < 0$. Moreover, there are no flow \vec{F} through the surfaces $\partial\Omega_s$ and $\partial\Omega_N$, i.e., $\vec{F} \cdot \vec{n} \leq 0$. To satisfy the last inequality, we extend (expand) the diffusion function in Ω^+ as follows

$$\begin{aligned} D(t, x) &= 0 && \text{in } \Omega_1 \cup \Omega_2 \cup \partial\Omega_s, \\ 0 < \underline{D} \leq D(t, x) \leq \overline{D} &\leq 1 && \text{in } \Omega, \\ D(t, x) &= 0, && \text{on } \partial\Omega^+. \end{aligned}$$

Thus, the Eq. (4.6) describes the flow near the functionalized surface.

$$\begin{aligned} \partial_t u(t, x_s) &= -\nabla \cdot (J_D(t, x_s)) \\ &- r_a u(t, x_s)(C_{P,0} - u(t, x_{s-1})) + r_d u(t, x_{s-1}) \\ &- k_a u(t, x_s)(C_{nT,max} - u(t, x_{s-2})) + k_d u(t, x_{s-2}), \end{aligned} \tag{4.6}$$

where $x_s \in \Omega_s$, $x_{s-1} \in \Omega_1$, $x_{s-2} \in \Omega_2$ and $t \in (0, T]$.

In Ω_1 the both flows \vec{J}_a and \vec{J}_d change their directions, i.e., $\vec{J}_a \cdot \vec{n} < 0$, $\vec{J}_d \cdot \vec{n} > 0$. Analogously we consider the flows $\vec{J}_{a,n}$ and $\vec{J}_{d,n}$. Hence, the equations (4.1) and (4.2) can be

rewritten as

$$\partial_t u(t, x_{s-1}) = r_a u(t, x_s) (C_{P,0} - u(t, x_{s-1})) - r_d u(t, x_{s-1}), \quad (4.7)$$

$$\partial_t u(t, x_{s-2}) = k_a u(t, x_s) (C_{nT,max} - u(t, x_{s-2})) - k_d u(t, x_{s-2}), \quad (4.8)$$

where $x_s \in \Omega_s$, $x_{s-1} \in \Omega_1$, $x_{s-2} \in \Omega_2$ and $t \in (0, T]$.

Thus, we consider the initial-boundary-value problem $u(t, x) : (0, T] \times \Omega^+ \mapsto \mathbb{R}$ described by the equations (4.5)-(4.8) with initial conditions

$$u(t=0, x) = u_I(x) := \begin{cases} C_{T,0}, & x \in \Omega_s \cup \Omega_m, \\ 0, & x \in \Omega_1 \cup \Omega_2, \end{cases} \quad (4.9)$$

and with Neumann boundary conditions at the inert walls

$$\frac{\partial u(t, x)}{\partial \vec{n}} = 0, \quad x \in \partial\Omega_N, \quad (4.10)$$

where \vec{n} is the outward unit normal vector along $\partial\Omega_N$ and $C_{P,0}, C_{T,0}, C_{nT,max}, r_a, r_d, k_a$ and k_d are the given constants, i.e. the experimentally measured quantities, and $\frac{r_d}{r_a} \ll 1$ and $\frac{k_d}{k_a} \ll 1$.

Lemma 4.1.1. *Law of mass conservation .*

The solution $u(t, \mathbf{x})$ of the initial-boundary-value problem (4.5)-(4.10) satisfies the global law of mass conservation:

$$\int_{\Omega^+} u(t, \mathbf{x}) d\mathbf{x} = \int_{\Omega^+} u_I(\mathbf{x}) d\mathbf{x} = \text{const},$$

$$\|u(t, \mathbf{x})\|_{L^1(\Omega^+)} = \|u_I(\mathbf{x})\|_{L^1(\Omega^+)} < \infty, \quad \forall t,$$

where $u_I(\mathbf{x})$ is the initial concentration of target molecules given by (4.9) and $d\mathbf{x} = dx dy dz$ if $\Omega^+ \subset \mathbb{R}^3$.

Proof. Let $\Omega^+ \setminus \Omega_m = \Omega_s \cup \Omega_1 \cup \Omega_2$ and $\Omega = \Omega_m \cup \Omega_s$ be the same as described above.

Due to the special choice of domains Ω_1 and Ω_2 , the function $u(t, x_s) \in \Omega_s$ can be specified in the domain $\Omega^+ \setminus \Omega_m$ as a function

$$u_s(t, \mathbf{x}) = u(t, x_s) \quad \text{in } \Omega_s \quad \text{and} \quad u_s(t, \mathbf{x}) = 0 \quad \text{in } \Omega_m \cup \Omega_1 \cup \Omega_2.$$

Analogously we can write for $u(t, x_{s-1}) \in \Omega_1$, $u(t, x_{s-2}) \in \Omega_2$ and $u(t, x) \in \Omega_m$

$$\begin{aligned} u_1(t, \mathbf{x}) &= u(t, x_{s-1}) \quad \text{in } \Omega_1 & \text{and} & \quad u_1(t, \mathbf{x}) = 0 \quad \text{in } \Omega_m \cup \Omega_s \cup \Omega_2, \\ u_2(t, \mathbf{x}) &= u(t, x_{s-2}) \quad \text{in } \Omega_2 & \text{and} & \quad u_2(t, \mathbf{x}) = 0 \quad \text{in } \Omega_m \cup \Omega_s \cup \Omega_1, \\ u_0(t, \mathbf{x}) &= u(t, x) \quad \text{in } \Omega_m & \text{and} & \quad u_0(t, \mathbf{x}) = 0 \quad \text{in } \Omega_s \cup \Omega_1 \cup \Omega_2. \end{aligned}$$

We integrate $\partial_t u(t, \mathbf{x})$ over domain Ω^+

$$\begin{aligned} \int_{\Omega^+} \partial_t u(t, \mathbf{x}) \, d\mathbf{x} &= \int_{\Omega_m} \nabla \cdot (\mathbf{D} \nabla u_0(t, \mathbf{x})) \, d\mathbf{x} + \int_{\Omega_{\Omega^+ \setminus \Omega_m}} \nabla \cdot (\mathbf{D} \nabla u_s(t, \mathbf{x})) \, d\mathbf{x} \\ &\quad - \int_{\Omega_{\Omega^+ \setminus \Omega_m}} \left(r_a u_s(t, \mathbf{x})(C_{P,0} - u_1(t, \mathbf{x})) - r_d u_1(t, \mathbf{x}) \right) \, d\mathbf{x} \\ &\quad - \int_{\Omega_{\Omega^+ \setminus \Omega_m}} \left(k_a u_s(t, \mathbf{x})(C_{nT,max} - u_2(t, \mathbf{x})) - k_d u_2(t, \mathbf{x}) \right) \, d\mathbf{x} \\ &\quad + \int_{\Omega_{\Omega^+ \setminus \Omega_m}} \left(r_a u_s(t, \mathbf{x})(C_{P,0} - u_1(t, \mathbf{x})) - r_d u_1(t, \mathbf{x}) \right) \, d\mathbf{x} \\ &\quad + \int_{\Omega_{\Omega^+ \setminus \Omega_m}} \left(k_a u_s(t, \mathbf{x})(C_{nT,max} - u_2(t, \mathbf{x})) - k_d u_2(t, \mathbf{x}) \right) \, d\mathbf{x}. \end{aligned}$$

Hence, the mass conservation law in differential form can be written as

$$\int_{\Omega^+} \partial_t u(t, \mathbf{x}) \, d\mathbf{x} = \int_{\Omega^+} \nabla \cdot (D(\mathbf{x}) \nabla u(t, \mathbf{x})) \, d\mathbf{x} = - \int_{\Omega^+} \nabla \cdot J_D(t, \mathbf{x}) \, d\mathbf{x}.$$

We apply the divergence theorem and use the definition of diffusion on the boundary $\partial\Omega^+$

$$\partial_t \int_{\Omega^+} u(t, \mathbf{x}) \, d\mathbf{x} = \int_{\partial\Omega^+} (D(\mathbf{x}) \nabla u(t, \mathbf{x})) \cdot \vec{\mathbf{n}} \, d\mathbf{x} = 0.$$

This implies the global law of mass conservation

$$\int_{\Omega^+} u(t, \mathbf{x}) \, d\mathbf{x} = \int_{\Omega^+} u_I(\mathbf{x}) \, d\mathbf{x} = \text{const.}$$

□

For the above suggested model we will give in the next section a discretized conservative scheme and demonstrate that the mass can be conserved exactly. To show the existence, uniqueness and properties of the solution we consider an equivalent problem using (4.3) and (4.4) under new notations. Let $u_1(t, u)$ and $u_2(t, u)$ be the unique solutions of (4.7) and (4.8), respectively, and denote the second and the third terms in eq. (4.6) as $b(t, u)$ and $f(t, u)$.

$$u_1(t, u) = \frac{r_a u(t, x) C_{P,0}}{r_d + r_a u(t, x)} \left(1 - e^{-(r_a u(t, x) + r_d)t} \right) \quad t \in (0, T], \quad x \in \Omega_s, \quad (4.11)$$

$$u_2(t, u) = \frac{k_a u(t, x) C_{nT,max}}{k_d + k_a u(t, x)} \left(1 - e^{-(k_a u(t, x) + k_d)t} \right) \quad t \in (0, T], \quad x \in \Omega_s, \quad (4.12)$$

$$d := d(x) = \begin{cases} 1, & t \in (0, T], \quad x \in \Omega_m, \\ 0, & t \in (0, T], \quad x \in \Omega_s, \end{cases} \quad (4.13)$$

$$b(t, x, u) := \begin{cases} 1, & t \in (0, T], \quad x \in \Omega_m, \\ r_a(C_{P,0} - u_1(t, u)) + k_a(C_{nT,max} - u_2(t, u)), & t \in (0, T], \quad x \in \Omega_s, \end{cases} \quad (4.14)$$

$$f(t, x, u) := \begin{cases} 0, & t \in (0, T], \quad x \in \Omega_m, \\ r_d u_1(t, u) + k_d u_2(t, u), & t \in (0, T], \quad x \in \Omega_s, \end{cases} \quad (4.15)$$

$$\partial_t u(t, x) = \nabla \cdot (a \nabla u(t, x)) - (b(t, \hat{u}) - d) u(t, x) + f(t, \hat{u}), \quad t \in (0, T], \quad x \in \Omega, \quad (4.16)$$

$$\begin{aligned} \frac{\partial u(t, x)}{\partial \vec{n}} &= 0, & t \in (0, T], \quad x \in \partial\Omega_N, \\ u(t, x) &= 0 & t \in (0, T], \quad x \in \Omega_D, \\ u(t, x) &= u_I & t = 0, \quad x \in \Omega, \\ a &:= D(x) \in (0, 1], & t \in (0, T], \quad x \in \Omega. \end{aligned} \quad (4.17)$$

\hat{u} denotes that its value is obtained at the earlier iterative step. To solve the initial-boundary-value problem (4.11) - (4.17) we use the following algorithm. We start with $b = b(u_I)$ and $f = f(u_I)$, then solve the equation (4.16) and then recalculate the coefficients $b(t, \hat{u}) = b(t, u)$ and $f(t, \hat{u}) = f(t, u)$.

Lemma 4.1.2. *The solution of the initial-boundary-value problem (4.5)-(4.10) and, therefor, the solution of the equivalent systems (4.11)-(4.16) is unique and it is non-negative in $(0, T] \times \Omega_m$ and strictly positive in $(0, T] \times \Omega_s$.*

Proof. We choose $u = c + v$, where c is a positive constant equal to $\inf u_I$.

If $\|v\|_{C(\Omega^+)} \leq c$, the function u will be non-negative.

Since u fulfills the law of mass conservation, we can estimate

$$\|v\|_{C(\Omega^+)} \leq \|v\|_{L^1(\Omega^+)} = \|u - c\|_{L^1(\Omega^+)} = \int_{\Omega^+} u \, dx - \int_{\Omega^+} c \, dx = \int_{\Omega^+} u_I \, dx - \int_{\Omega^+} c \, dx = 0 \leq c.$$

This give us a non-negativity of u .

Next we consider the function $u \equiv 0$. It satisfies the equation (4.6) only if $u_1 = 0$ and $u_2 = 0$, i.e., at the time $t = 0$, and will be strictly positive in $(0, T] \times \Omega_s$.

Assume that v_1 and v_2 are two different ($v_1 \not\equiv v_2$) solutions of our problem.

$$\|v_1\|_{L^1(\Omega^+)} - \|v_2\|_{L^1(\Omega^+)} = \|u_I\|_{L^1(\Omega^+)} - \|u_I\|_{L^1(\Omega^+)} = 0.$$

On the other hand $\int_{\Omega^+} v_1 \, dx - \int_{\Omega^+} v_2 \, dx = \int_{\Omega^+} (v_1 - v_2) \, dx = 0$ if $v_1 \equiv v_2$.

Thus, we can conclude that the solution is unique. □

Due to the inequalities (4.3) and (4.4), we get in the domain $(0, T] \times \Omega_s$ the following

estimates

$$0 < u_1(t, u) \leq \frac{r_a u C_{P,0}}{r_d + r_a u} < C_{P,0},$$

$$0 < u_2(t, u) < C_{nT,max},$$

$$0 < \underline{b} \leq b(t, u) < r_a C_{P,0} + k_a C_{nT,max} =: \bar{b}, \quad (4.18)$$

$$0 < \underline{f} \leq f(t, u) < r_d C_{P,0} + k_d C_{nT,max} =: \bar{f}. \quad (4.19)$$

Lemma 4.1.3. *Let $F(t, u) := -(b(t, u) - d(x)) u(t, x) + f(t, u)$ for $u \in \Omega$ be a non-linear part of the Eq. (4.16), where $d(t, u)$, $b(t, u)$, and $f(t, u)$ are given by the Eqs. (4.13) - (4.15), respectively. The function $F : \mathbb{R} \rightarrow \mathbb{R}$ is Lipschitz continuous in u and continuous in t .*

Proof. In the proof we only consider the inhomogeneity in the domain Ω_s , because the function F is equal to zero in the domain Ω_m .

$$\begin{aligned} F(t, u) &= -b(t, u) u(t, x) + f(t, u) \\ &= -r_a C_{P,0} u - k_a C_{nT,max} u + (r_a u + r_d) u_1 + (k_a u + k_d) u_2 \\ &= -r_a C_{P,0} u - k_a C_{nT,max} u + r_a C_{P,0} u(1 - e^{-(r_a u + r_d)t}) + k_a C_{nT,max} u(1 - e^{-(k_a u + k_d)t}) \end{aligned}$$

The function F is everywhere differentiable in u with the following derivative

$$\begin{aligned} F'_u &= r_a C_{P,0} (1 - e^{-(r_d + r_a u)t}) + r_a^2 C_{P,0} t u e^{-(r_d + r_a u)t} - r_a C_{P,0} \\ &\quad + k_a C_{nT,max} (1 - e^{-(k_d + k_a u)t}) + k_a^2 C_{nT,max} t u e^{-(k_d + k_a u)t} - k_a C_{nT,max} \end{aligned}$$

We analyze the function $u e^{-(r_d + r_a u)t}$. It is concave for $t \in (0, T]$ and $u \geq 0$ and its derivative

$$\left(u e^{-(r_d + r_a u)t} \right)'_u = e^{-t(ur_a + r_d)} (1 - t u r_a)$$

has a root in $\frac{1}{t r_a}$. Hence, this function is bounded

$$u e^{-(r_d + r_a u)t} \leq \frac{1}{t r_a}$$

Similarly we estimate

$$u e^{-(k_d + k_a u)t} \leq \frac{1}{t k_a}$$

The functions $1 - e^{-(r_d + r_a u)t}$ and $1 - e^{-(k_d + k_a u)t}$ are located between 0 and 1 for $t \in (0, T]$ and $u \geq 0$.

Therefore, the absolute value of the derivative is bounded above by a constant that does not depend on time.

$$|F'_u| \leq C_{P,0} r_a + C_{nT,max} k_a.$$

This in particular implies a growth estimate

$$|F(y)| \leq c_F(1 - |y|)$$

for each $y \in \mathbb{R}$ and some constant c_F , which does not depend on y . □

Hence, the diffusion equation with reactive boundary conditions has been reformulated to the well-studied initial-boundary-value parabolic problem and we can apply the standard theory for linear parabolic PDE given, for instance, in Ref. [18].

Let ϕ be a test function in $H_0^1([0, T] \times \Omega)$. Multiplying the equation (4.16) by ϕ and applying partial integration over Ω , we can rewrite it in following form

$$\langle \dot{u}, \phi \rangle + B[u, \phi; t] = (F, \phi), \quad (4.20)$$

$$\frac{\partial u(t, x)}{\partial \vec{n}} = 0, \quad t \in (0, T], \quad x \in \partial\Omega_N, \quad (4.21)$$

$$u(t, x) = 0 \quad t \in (0, T], \quad x \in \Omega_D, \quad (4.22)$$

$$u(t, x) = u_I \quad t = 0, \quad x \in \Omega, \quad (4.23)$$

where $\langle \dot{u}, \phi \rangle$ is a duality pairing of the functions from $H^{-1}(\Omega)$ and $H_0^1(\Omega)$, $B[u, \phi; t]$ is a time-dependent bilinear form in $H_0^1(\Omega)$, (F, ϕ) is an inner product in $L^2(\Omega)$, and the function F is defined as above.

Definition 4.1.1. (Weak solution)

The function $u \in L^2(0, T; H_0^1(\Omega))$ with its time derivative $\dot{u} \in L^2(0, T; H^{-1}(\Omega))$ is a weak solution of (4.11) - (4.17) if

- it solves the equation (4.16) in weak sense, i.e., solves the Eq. (4.20) for each $\phi \in H_0^1([t_0, T_0] \times \Omega)$ and for initial data $u_I \in L^2(\Omega)$;
- it satisfies the boundary-value conditions (4.21) and (4.22).

Theorem 4.1.4. (Existence of weak solution)

The initial-boundary-value problem (4.5)-(4.10) has a weak solution $u(t, \mathbf{x})$ in $L^2(0, T; H_0^1(\Omega))$ for all $t \in (0, T]$ and in $C(0, T; L^2(\Omega))$ for a.e. $t \in (0, T]$.

Proof. We consider a space $\mathcal{K} := C([t_0, T_0]; L^2(\Omega))$ with the norm

$$\|\mathbf{v}\|_{\mathcal{K}} = \max_{t \in [t_0, T_0]} \|\mathbf{v}(t)\|_{L^2(\Omega)}$$

We linearize the equation (4.20) by setting $F(t, u) = F(t, u^*) =: F_u$ and apply the existence theory for linear parabolic equations, where $u^* \in \mathcal{K}$ is a given function and, by consequence of the growth estimate, $F(t, u^*) \in L^2(t_0, T_0; L^2(\Omega))$.

Let u be the unique weak solution of the linearized initial-boundary-value problem given by (4.20) - (4.23), i.e., it satisfies

$$\partial_t u - \nabla \cdot D \nabla u = F_u \quad (4.24)$$

for each $\phi \in H_0^1([t_0, T_0] \times \Omega)$.

We define $Gu^* = u$ so that $G : \mathcal{K} \rightarrow \mathcal{K}$. Additionally, we choose $v^* \in \mathcal{K}$ and define $v := Gv^*$. Consequently v satisfies

$$\partial_t v - \nabla \cdot D \nabla v = F_v, \quad (4.25)$$

where $F_v := F(t, v^*)$. After subtracting (4.25) from (4.24) and under notations $w := u - v = Gu^* - Gv^*$ and $F_w := F_u - F_v$ we write

$$\partial_t w - \nabla \cdot D \nabla w = F_w \quad (4.26)$$

Note that $\partial_t(w^2) = 2w \partial_t w$ and

$$\int_{\Omega} \nabla w \cdot D \nabla w \, dx = w \cdot D \nabla w|_{\partial\Omega} - \int_{\Omega} w \cdot D \nabla w \, dx = - \int_{\Omega} w \cdot D \nabla w \, dx,$$

because $D(x)|_{\partial\Omega} = 0$. Multiplying by $2w$ and integrating over Ω we obtain

$$\begin{aligned} 2 \int_{\Omega} w \partial_t w \, dx - 2 \int_{\Omega} w \nabla \cdot D \nabla w \, dx &= 2 \int_{\Omega} w F_w \, dx, \\ \partial_t \int_{\Omega} w^2 \, dx - 2D \int_{\Omega} (\nabla w)^2 \, dx &= 2 \int_{\Omega} w F_w \, dx. \end{aligned}$$

Hence

$$\partial_t \|w\|_{L^2(\Omega)}^2 + 2D \|w\|_{H_0^1(\Omega)}^2 = 2(w, F_w).$$

We find $(F(u^*) - F(v^*))^2 \leq c_w (u^* - v^*)^2 = c_w (w^*)^2$ from the Lipschitz continuity of function F , where c_w is a square Lipschitz constant, which does not depend on u^* and v^* , and $w^* := u^* - v^*$.

$$\begin{aligned} 2(w, F_w) &\leq 2(|w| |F_w|) = 2 \int_{\Omega} |w| |F_w| \, dx \leq 2 \int_{\Omega} \left(\frac{\delta}{2} |w|^2 + \frac{1}{2\delta} |F_w|^2 \right) \, dx \\ &= \delta \|w\|_{L^2(\Omega)}^2 + \delta^{-1} \|F_w\|_{L^2(\Omega)}^2 \leq \delta \|w\|_{L^2(\Omega)}^2 + \delta^{-1} c_w \|w^*\|_{L^2(\Omega)}^2 \quad \text{for } \forall \delta > 0. \end{aligned}$$

Using the Poincaré-Friedrich inequality $\|w\|_{L^2(\Omega)}^2 \leq c_{pf} \|w\|_{H_0^1(\Omega)}^2$ we calculate

$$\partial_t \|w\|_{L^2(\Omega)}^2 \leq \delta c_{pf} \|w\|_{H_0^1(\Omega)}^2 - 2D \|w\|_{H_0^1(\Omega)}^2 + \delta^{-1} c_w \|w^*\|_{L^2(\Omega)}^2.$$

The term $\delta c_{pf} \|w\|_{H_0^1(\Omega)}^2 - 2D \|w\|_{H_0^1(\Omega)}^2$ can be eliminated, if we choose δ sufficiently small,

i.e., $\delta < \frac{2D}{c_p f}$ and $\delta < 1$ at the same time. Hence, we estimate

$$\partial_t \|w\|_{L^2(\Omega)}^2 \leq c_w \|w^*\|_{L^2(\Omega)}^2 \leq c_w \|w^*\|_{\mathcal{K}}^2. \quad (4.27)$$

Integrating this inequality from t_0 to $\tau \in [t_0, T_0]$ we obtain

$$\|w(\tau)\|_{L^2(\Omega)}^2 \leq c_w \int_{t_0}^{\tau} \|w^*\|_{\mathcal{K}}^2 d\tau \leq c_w \delta_T \|w^*\|_{\mathcal{K}}^2,$$

where $\|w^*\|_{\mathcal{K}}^2$ does not depend on t . Because the left-hand side is valid for each $\tau \in [t_0, T_0]$ we can maximize it with respect to τ

$$\begin{aligned} \|Gu^* - Gv^*\|_{\mathcal{K}}^2 &\leq c_w \delta_T \|u^* - v^*\|_{\mathcal{K}}^2, \\ \|Gu^* - Gv^*\|_{\mathcal{K}} &\leq \sqrt{c_w \delta_T} \|u^* - v^*\|_{\mathcal{K}}. \end{aligned}$$

Therefore, we conclude that the mapping G is a strict contraction if $\sqrt{c_w \delta_T} < 1$. Selecting $T_0 > 0$ so small that $\delta_T < c_w^{-1}$ we can apply Banach's fixed point theorem to find a weak solution on some small time interval.

To find a weak solution existing on the full interval $[0, T]$ we apply iteratively the following schema:

- Start with $t_0 := 0$ and initial conditions $u(t_0) = u_I$, find the weak solution u_0 on the time interval $[t_0, t_0 + \delta_T]$.
- Continue with $t_1 := t_0 + \delta_T$ and initial conditions $u(t_1) = u_0$, find the weak solution u_1 on the time interval $[t_1, t_1 + \delta_T]$.
- After finitely many steps we construct our weak solution.

Let φ_{ε_1} and φ_{ε_2} be mollifiers in t of u , where ε_1 and ε_2 are real numbers from $(0, 1]$. Set $\sigma := \max\{\varepsilon_1, \varepsilon_2\}$ and extend the function u to the larger time interval $I := [t_0 - \sigma, T_0 + \sigma]$, i.e., $u \in L^2(I; H_0^1(\Omega))$. Next we consider two sets of smooth functions $u^{\varepsilon_1} := \varphi_{\varepsilon_1} * u$ and $u^{\varepsilon_2} := \varphi_{\varepsilon_2} * u$, where $*$ denotes a convolution and $u^{\varepsilon_1}, u^{\varepsilon_2} \in \mathcal{K}$.

We repeat the same calculations as above until (4.27) with $w^* := \varphi_{\varepsilon_1} * u^* - \varphi_{\varepsilon_2} * u^*$, $w := u^{\varepsilon_1} - u^{\varepsilon_2}$ and $F_w := F(t, \varphi_{\varepsilon_1} * u^*) - F(t, \varphi_{\varepsilon_2} * u^*)$ to find

$$\partial_t \|u^{\varepsilon_1} - u^{\varepsilon_2}\|_{L^2(\Omega)}^2 \leq c_w \|\varphi_{\varepsilon_1} * u^* - \varphi_{\varepsilon_2} * u^*\|_{\mathcal{K}}^2.$$

Hence

$$\|u^{\varepsilon_1}(\tau) - u^{\varepsilon_2}(\tau)\|_{L^2(\Omega)}^2 \leq \|u^{\varepsilon_1}(s) - u^{\varepsilon_2}(s)\|_{L^2(\Omega)}^2 + c_w \int_s^{\tau} \|\varphi_{\varepsilon_1} * u^* - \varphi_{\varepsilon_2} * u^*\|_{\mathcal{K}}^2 d\tau$$

for all $t_0 \leq s < t \leq T_0$. We fix all points $s \in (t_0, T_0)$ for which $u^{\varepsilon_1}(s) \rightarrow u(s)$ in $L^2(\Omega)$. We maximize the left-hand side with respect to τ and take a limes

$$\lim_{\varepsilon_1, \varepsilon_2 \rightarrow 0} \|u^{\varepsilon_1} - u^{\varepsilon_2}\|_{\mathcal{K}}^2 \leq \lim_{\varepsilon_1, \varepsilon_2 \rightarrow 0} \left(\|u^{\varepsilon_1}(s) - u^{\varepsilon_2}(s)\|_{L^2(\Omega)}^2 + c_w \delta_T \|\varphi_{\varepsilon_1} * u^* - \varphi_{\varepsilon_2} * u^*\|_{\mathcal{K}}^2 \right)$$

Therefore, the smooth functions $\{u^{\varepsilon_1}\}_{\varepsilon_1 \in (0,1]}$ converge in \mathcal{K} to a $v \in \mathcal{K}$, where $v := \lim_{\varepsilon_2 \rightarrow 0} \{u^{\varepsilon_2}\}$. Due to $u^{\varepsilon_1}(t) \rightarrow u(t)$ for a.e. t , we conclude $u = v$ a.e.. If we chose $t_0 := 0$ and $T_0 := T$, we obtain the statement of the theorem. □

Theorem 4.1.5. *Es exists a constant*

$$M = \max \left\{ \sup_{\Omega} |u_I|, \sup_{(0,T] \times \partial\Omega} |u_D| \right\} + \frac{\sup_{(0,T] \times \Omega} f}{\inf_{(0,T] \times \Omega} b},$$

which does not depend on t , such that

$$\max_{\Omega} |u| \leq M.$$

Proof. We define the operator L as follows

$$Lu := \partial_t u - \nabla \cdot (a \nabla u) + (b - c)u = f.$$

Consider the functions $u - M$ and $u + M$, where M is defined as

$$M = \max \left\{ \sup_{\Omega} |u_I|, \sup_{(0,T] \times \partial\Omega} |u_D| \right\} + \frac{\sup_{(0,T] \times \Omega} f}{\inf_{(0,T] \times \Omega} b},$$

where $\inf_{(0,T] \times \Omega} b$ and $\sup_{(0,T] \times \Omega} f$ are given by the estimations (4.18) and (4.19).

$$L(u - M) = Lu - (b - c)M = \begin{cases} -M \leq 0 & x \in \Omega_m, \\ f - bM \leq 0 & x \in \Omega_s, \end{cases}$$

$$L(u + M) = Lu + (b - c)M = f + (b - c)M \geq 0.$$

According weak maximum principle $\max_{\Omega} (u - M) \leq 0$ and $\min_{\Omega} (u + M) \geq -\max_{\partial\Omega} \{-\min(u + M, 0)\} = 0$, $u + M|_{\partial\Omega} = M$, i.e., $\max_{\Omega} u \leq M$ and $\min_{\Omega} u \geq -M$, therefor $\max_{\Omega} |u| \leq M$. □

4.2 Discretized model

4.2.1 Conservative scheme

For the discretization of our model we have chosen the finite-difference scheme, because, as we will see later on, such numerical approximation conserves the particles exactly.

For simplicity we skip in this section the indices k and l and use a notation $u_i^j := u_{i,k,l}^j$.

Let $u(t_j, x_i, y_k, z_l) = u_{i,k,l}^j := C_T(t_j, x_i, y_k, z_l)$ be a new discretized variable, where u_{s-1}^j and u_{s-2}^j correspond to $C_{PT}(t_j)$ and $C_{nT}(t_j)$, respectively. We define discretized operators as

$$\begin{aligned}\tilde{\mathcal{L}}(i, k, l) &:= \frac{u_{i,k,l}^{j+1} - u_{i,k,l}^j}{\Delta t}, \\ \mathcal{L}_x(i, k, l) &:= \frac{1}{\Delta x} \left(d_{i+1}^x \frac{u_{i+1}^j - u_i^j}{\Delta x} - d_i^x \frac{u_i^j - u_{i-1}^j}{\Delta x} \right),\end{aligned}$$

where $d_i^x = D(x_i - \frac{\Delta x}{2}, y_k, z_l)$ or $d_i^x = \sqrt{D(x_i, y_k, z_l)D(x_{i-1}, y_k, z_l)}$ and, hence, $d_s^x = 0$ and $d_{s+N_x}^x = d_{s+N_x-1}^x$. Analogously we can write $\mathcal{L}_y(i, k, l)$, $\mathcal{L}_z(i, k, l)$, d_k^y and d_l^z . The functionalized surface is located at s and $N_x + 3$ is a number of space grid points.

In summary, the system of equations for $j = 0, \dots, N_t$, $k = 1, \dots, N_y$ and $l = 1, \dots, N_z$ are detailed as follows

$$\tilde{\mathcal{L}}(i, k, l) = \mathcal{L}_x(i, k, l) + \mathcal{L}_y(i, k, l) + \mathcal{L}_z(i, k, l) \quad i = s + 1, \dots, s - 1 + N_x, \quad (4.28)$$

$$\begin{aligned}\tilde{\mathcal{L}}(s, k, l) &= \mathcal{L}_x(s, k, l) + \mathcal{L}_y(s, k, l) + \mathcal{L}_z(s, k, l) \\ &\quad - r_a(C_{P,0} - u_{s-1}^j)u_s^j + r_d u_{s-1}^j \\ &\quad - k_a(C_{nT,max} - u_{s-2}^j)u_s^j + k_d u_{s-2}^j,\end{aligned} \quad (4.29)$$

$$\tilde{\mathcal{L}}(s-1, k, l) = r_a(C_{P,0} - u_{s-1}^j)u_s^j - r_d u_{s-1}^j, \quad (4.30)$$

$$\tilde{\mathcal{L}}(s-2, k, l) = k_a(C_{nT,max} - u_{s-2}^j)u_s^j - k_d u_{s-2}^j, \quad (4.31)$$

$$\text{BC:} \quad u_{s-1+N_x}^j = u_{s+N_x}^j, \quad (4.32)$$

$$\text{IC:} \quad u_i^0 = C_{T,0}, \quad i = s + 1, \dots, s - 1 + N_x, \quad (4.33)$$

$$\text{IC:} \quad u_{s-2}^0 = u_{s-1}^0 = 0. \quad (4.34)$$

Lemma 4.2.1. *The discretized model (4.28)-(4.34) satisfies the law of mass conservation.*

Proof. The integral of C_T over Ω^+ in discretized form can be obtained from Eqs. (4.28)-(4.31) by summing the u_i^{j+1} over all space grid points with $s = 2$.

$$\begin{aligned}\sum_{i=0}^{N_x+1} u_i^{j+1} &= \sum_{i=0}^{N_x+1} u_i^j + \frac{\Delta t}{\Delta x^2} \underbrace{\left(\sum_{i=3}^{N_x+1} (d_{i+1}^x u_{i+1}^j - d_{i+1}^x u_i^j - d_i^x u_i^j + d_i^x u_{i-1}^j) + d_3^x u_3^j - d_3^x u_2^j \right)}_{=0} \\ &\stackrel{(4.32)}{=} N_x C_{T,0} = \text{const}.\end{aligned}$$

Note, that in 3-d case $\sum u_{i,k,l}^{j+1} = N_x N_y N_z C_{T,0} = \text{const}$, because the chemical reaction is one-dimensional. □

4.2.2 Stability and convergence

Theorem 4.2.2. (Stability) Let $\{u_i^j\}$ be the solution of (4.28)-(4.34) and $D = \overline{D}$. Then, under the CFL-conditions $\Delta t \leq \min\{\frac{\Delta x^2}{4D}, \frac{\Delta y^2}{2D}, \frac{\Delta z^2}{2D}, \frac{1}{2r_d}, \frac{1}{2k_d}, \frac{1}{4r_a C_{P,0}}, \frac{1}{4k_a C_{nT,max}}\}$, $\forall T > 0$ there exists a positive constant c , such that $\|u^j\|_{l^1} \leq c\|u^0\|_{l^1}$, by $j\Delta t = T$.

Proof. The definition of norm in l^1 is

$$\begin{aligned} \|u^j\|_{l^1} &= h \sum_{i,k,l} |u_{i,k,l}^j| = h \sum_{k,l} \sum_{i=0}^{N_x+1} |u_i^j| \\ &= h \sum_{k,l} \left(\sum_{i=3}^{N_x+1} |u_i^j| + |u_0^j| + |u_1^j| + |u_2^j| \right), \end{aligned}$$

where $h = \Delta x \Delta y \Delta z$, $i = 0, \dots, N_x + 1$, $k = 1, \dots, N_y$ and $l = 1, \dots, N_z$. $|u_0^j| \leq C_{P,0}$ and $|u_1^j| \leq C_{nT,max}$.

Under notations $a_{1,i} = d_i^x \frac{\Delta t}{\Delta x^2}$, (note $a_{1,i} = 0$ for $i = \{0, 1, N_x + 2\}$), $a_2 = k_a C_{nT,max} \Delta t$, $a_3 = r_a C_{P,0} \Delta t$, $a_4 = k_d \Delta t$, $a_5 = r_d \Delta t$, $a_6 = k_a \Delta t$, $a_7 = r_a \Delta t$ and $\tau = \Delta t$ we consider the following absolute values

$$\begin{aligned} \sum_{i=3}^{N_x+1} |u_i^j| &\stackrel{(4.28)}{=} \sum_{i=3}^{N_x+1} |a_{1,i+1} u_{i+1}^{j-1} + (1 - a_{1,i+1} - a_{1,i}) u_i^{j-1} + a_{1,i} u_{i-1}^{j-1} + \tau \mathcal{L}_y(i, k, l) + \tau \mathcal{L}_z(i, k, l)|, \\ |u_0^j| &\stackrel{(4.31)}{=} |a_{1,0} u_0^{j-1} + (1 - a_{1,1} u_0^{j-1} - a_{1,0} u_0^{j-1} - a_4) u_0^{j-1} + (a_2 - a_6 u_0^{j-1}) u_2^{j-1} + a_{1,1} u_0^{j-1}|, \\ |u_1^j| &\stackrel{(4.30)}{=} |a_{1,1} u_1^{j-1} + (1 - a_{1,2} - a_{1,1} - a_5) u_1^{j-1} + (a_3 - a_7 u_1^{j-1}) u_2^{j-1} + a_{1,2} u_1^{j-1}|, \\ |u_2^j| &\stackrel{(4.29)}{=} |a_{1,3} u_3^{j-1} + \left(a_{1,2} + (1 - a_{1,3} - a_{1,2}) - (a_2 - a_6 u_0^{j-1}) - (a_3 - a_7 u_1^{j-1}) \right) u_2^{j-1} \\ &\quad + a_5 u_1^{j-1} + a_4 u_0^{j-1} + \tau \mathcal{L}_y(2, k, l) + \tau \mathcal{L}_z(2, k, l)| \\ &\leq a_{1,2} |u_2^{j-1}| + a_{1,3} |u_3^{j-1}| + a_5 |u_1^{j-1}| + a_4 |u_0^{j-1}| + |\tau \mathcal{L}_y(i, k, l)| + |\tau \mathcal{L}_z(i, k, l)| \\ &\quad + \left((1 - a_{1,3} - a_{1,2}) - (a_2 - a_6 u_0^{j-1}) - (a_3 - a_7 u_1^{j-1}) \right) |u_2^{j-1}|. \end{aligned}$$

The terms $\mathcal{L}_y(i, k, l)$ and $\mathcal{L}_z(i, k, l)$ appear in two- and three-dimensional cases, respectively, and will be considered separately. Note that $\mathcal{L}_y(i, k, l) = \mathcal{L}_z(i, k, l) = 0$ for $i = \{0, 1\}$.

Here $0 \leq a_{1,i} \leq 1/4$, $1/2 \leq 1 - a_{1,i+1} - a_{1,i} \leq 1$, $0 \leq a_4 \leq 1/2$, $0 \leq a_5 \leq 1/2$, $0 \leq a_2 - a_6 u_0^{j-1} \leq a_2 \leq 1/4$, $0 \leq a_3 - a_7 u_0^{j-1} \leq a_3 \leq 1/4$, $0 \leq 1 - a_{1,i+1} - a_{1,i} - a_4 \leq 1$, $0 \leq 1 - a_{1,i+1} - a_{1,i} - a_5 \leq 1$, $0 \leq 1 - a_{1,i+1} - a_{1,i} - (a_2 - a_6 u_0^{j-1}) - (a_3 - a_7 u_1^{j-1}) \leq 1$, for all $i \in [0, N_x + 3]$.

After summation and multiplication with $h/3$ we obtain the following inequality

$$\begin{aligned} \|u^j\|_{l^1} &\leq \frac{h}{3} \sum_{i,k,l} \left(a_{1,i} |u_i^{j-1}| + (1 - a_{1,i+1} - a_{1,i}) |u_i^{j-1}| + a_{1,i+1} |u_i^{j-1}| \right) \\ &\quad + \frac{h}{3} \sum_{i,k,l} |\tau \mathcal{L}_y(i, k, l)| + \frac{h}{3} \sum_{i,k,l} |\tau \mathcal{L}_z(i, k, l)| \\ &= \frac{h}{3} \sum_{i,k,l} |u_i^{j-1}| + \frac{h}{3} \sum_{i,k,l} |\tau \mathcal{L}_y(i, k, l)| + \frac{h}{3} \sum_{i,k,l} |\tau \mathcal{L}_z(i, k, l)|. \end{aligned}$$

Under analogous notations $b_{1,k} = d_k^y \frac{\Delta t}{\Delta x^2}$, where $d_k^y = d(i, k, l)$, $d(i, k, l) = 0$ for $i = 0, 1, N_x + 2$, and under CFL-conditions the coefficient estimations are

$$0 \leq b_{1,k} \leq 1/2, \quad 0 \leq 1 - b_{1,k+1} - b_{1,k} \leq 1.$$

$$\begin{aligned} \sum_{k=1}^{N_y} |\tau \mathcal{L}_y(i, k, l)| &= \sum_{k=1}^{N_y} |b_{1,k+1} u_{k+1}^{j-1} + (1 - b_{1,k+1} - b_{1,k}) u_i^{j-1} + b_{1,k} u_{k-1}^{j-1}|, \\ &= b_{1,1} u_1^{j-1} - b_{1,1} u_0^{j-1}, \\ \sum_{k=1}^{N_y} |\tau \mathcal{L}_y(i, k, l)| &\leq \sum_{k=1}^{N_y} \left(b_{1,k} |u_k^{j-1}| + (1 - b_{1,k+1} - b_{1,k}) |u_k^{j-1}| + b_{1,k+1} |u_k^{j-1}| \right) \\ &= \sum_{k=1}^{N_y} |u_k^{j-1}|. \end{aligned}$$

Analogously we treat the term $\mathcal{L}_z(i, k, l)$ and obtain the following estimation

$$\|u^j\|_{l^1} \leq h \sum_{i,k,l} |u_{i,k,l}^{j-1}| = \tilde{c} \|u^{j-1}\|_{l^1}$$

After recursive estimation we can find a constant c , such that $\|u^j\|_{l^1} \leq c \|u^0\|_{l^1}$. □

Theorem 4.2.3. (Convergence) *Let $U(t, x)$ be an exact smooth solution of the well-posed initial value problem (4.5)-(4.10). The numerical method (4.28)-(4.34) with diffusion coefficients defined above under CFL-conditions from Theorem 4.2.2 has convergence of order $(\Delta t, \Delta x, \Delta y^2, \Delta z^2)$, i.e.,*

$$\|U(t, x) - u_i^j\| = O(\Delta t, \Delta x, \Delta y^2, \Delta z^2).$$

Proof. From standard convergence theory for finite-difference scheme the diffusion equation has convergence of order $(\Delta t, \Delta x^2, \Delta y^2, \Delta z^2)$. It is easy to see, by using the Taylor-expansion, that the reaction terms from Eqs. (4.29)-(4.31), which appear only in x-direction, degrade the

convergence to first order, i.e., $O(\Delta x)$. □

Thus, the solution of Eqs. (4.28)-(4.32) give us a target distribution at the time t . The analyte concentration in the vicinity of functionalized surface will be used below in our work. As mentioned above the space step shall be small enough to provide the binding, for instance, $d_x := |\Omega_s| = 1.5 \times \text{Length}_{DNA} = |\Omega_1| = |\Omega_2|$.

On the other hand, there is a limit on the time step. For a diffusive process, a molecule travels the distance Δx during the time of about $\Delta t_{diff} = \frac{\Delta x^2}{2D}$ in $\Omega \setminus \Omega_s$ and $\Delta t_{diff} = \frac{\Delta x^2}{4D}$ in Ω_s . The time step Δt is required to be smaller than Δt_{diff} . If $\Delta t > \frac{1}{4r_a C_{P,0}}$ or $\Delta t > \frac{1}{4k_a C_{nT,max}}$ at the beginning of the simulation, when the association processes are predominant, we see the oscillation of the solution. The time step that does not satisfy the other CFL-conditions, i.e., $\Delta t \leq \frac{1}{2r_d}$ or $\Delta t \leq \frac{1}{2k_d}$, leads to the fluctuation at the time of chemical equilibrium.

We choose Δt and Δx so that they satisfy the CFL-conditions, but along with that they are still large enough to perform simulations within reasonable time. As it mentioned above, Δx shall be small enough to allow the chemical reactions. Therefore, we do not use the original problem, but take the simulations with scaled parameters $\tilde{r}_i := \delta^2 r_i$ and $\tilde{k}_i := \delta^2 k_i$, for $i = a, d$, respectively, where $\delta := \Delta x/d_x$.

4.3 Simulation results

In the following section we analyze a target hybridization kinetics under pure diffusion motion. The used nominal input parameters are summarized in Table 4.1, where the viscosity, which arises from the given temperature and salt concentration, is obtained from Ref. [27]. The equilibrium constant for hybridization process r_a/r_d is chosen in such a way that the binding efficiency reaches 50%, while the rate k_a/k_d is small.

Meaning	Variable	Value
Target concentration	$C_{T,0}$	1 μ M
Probe density	$C_{P,0}$	3×10^{12} molecules/cm ²
Equilibrium constants	r_a/r_d	$1.3 \times 10^6 \text{M}^{-1}$
	k_a/k_d	69.5M^{-1}
Length of DNA	L_{bp}	25 base-pairs (bp)
Radius of DNA	R_P, R_T, R_{PT}	1nm
NaCl concentration		1M
Temperature	T	298.15K
Fluid viscosity	μ_f	0,9719Ns/m ²
Diffusion coefficient	D	$8.90856 \times 10^{-11} \text{m}^2/\text{s}$

Table 4.1: Nominal input parameters.

The single-stranded B-DNA oligomer (ssDNA) is modeled as a rod-like molecule of length

L_{DNA} (0.34nm rise per bp) and a diameter $d = 2$ nm. The diffusion coefficient D for rod-like DNA molecules is determined to be $8.90856 \times 10^{-11} \text{m}^2/\text{s}$.

$$D = \frac{Ak_B T}{3\pi\eta L_{DNA}},$$

where A represents a correction factor [73] that is given by

$$A = \ln \frac{L_{DNA}}{d} + \frac{0.565}{L_{DNA}/d} - \frac{0.1}{(L_{DNA}/d)^2} + 0.312.$$

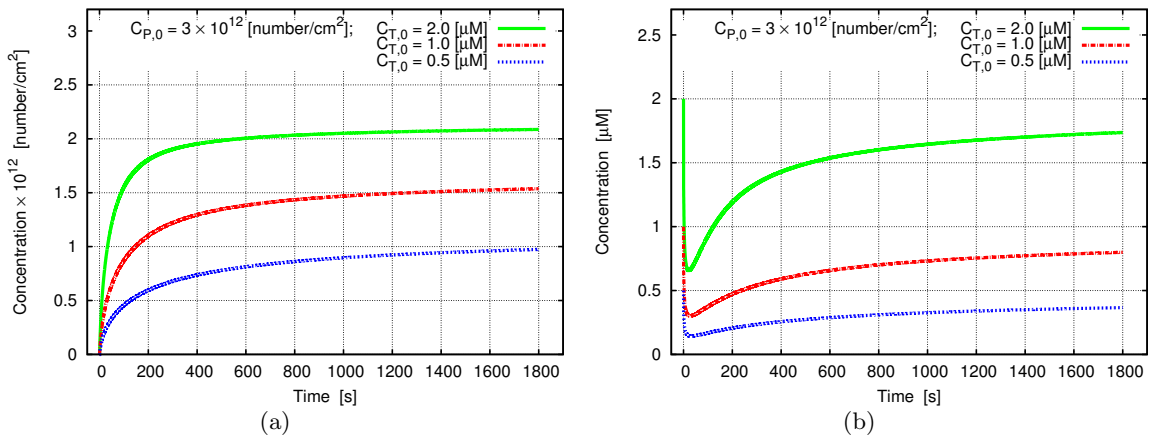


Figure 4.2: Simulation results obtained at different analyte concentrations. (a) Density of probe-target complexes as a function of time. The binding efficiencies are ca. 62%, 51% and 30% for the green, red and blue lines, respectively. (b) Transport of target molecules to the functionalized surface.

As it was mentioned above, the goal of a BioFET is to detect the analyte molecules in the physiological solution. That means, the number of target molecules is much smaller than the number of probe molecules that are functionalized to the surface. For this reason the developed method has to be capable of dealing with small concentration of analyte molecules. Fig. 4.2 (a) demonstrates the dynamics of the synthesis of probe-target complexes in a solution with relatively small initial analyte concentration. Fig. 4.2 (b) shows the transport of the target molecules to the functionalized surface that occurs at the same time. Because the binding speed at the beginning is faster than the transport of molecules a rapid decrease of targets at the surface is observed, as demonstrated in Fig. 4.2 (b). This amplitude depends not only on the initial concentrations of targets and probes (compare with Fig. 4.5 b) but also on their uniformity and on the type of the used biomolecules, i.e., on the hybridization parameters. The initial concentration of analyte molecules affects the speed and the efficiency of the hybridization. The binding efficiencies are found to be ca. 62%, 51% and 30% for the green, red and blue lines, respectively. Such a non-linear dependence of binding efficiency on concentration will be also shown in the Section 6.3.

If the number of probe and target molecules in the reaction chamber is equal, the binding efficiency reaches its maximum value of nearly 100% very fast, but it cannot be exactly 100%. This fact is shown in Fig. 4.3, which is in agreement with the estimation given by (4.3).

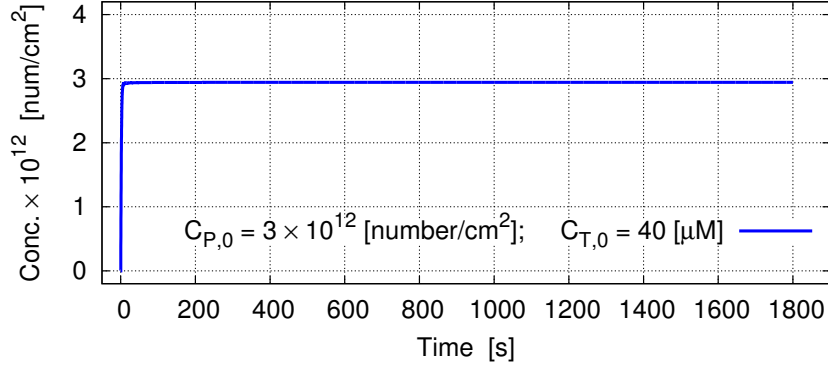


Figure 4.3: Dynamics of probe-target hybridization at high analyte concentration.

Previous research has shown that the hybridization efficiency of the target molecules to the probes depends on the density of the probe molecules [54], where under hybridization (or binding) efficiency (BE) at the time t we understand

$$BE(t) = \frac{C_{PT}(t)}{C_{P,0}} \times 100\%.$$

It has been asserted that the lower probe densities lead to higher hybridization efficiencies due to electrostatic effects.

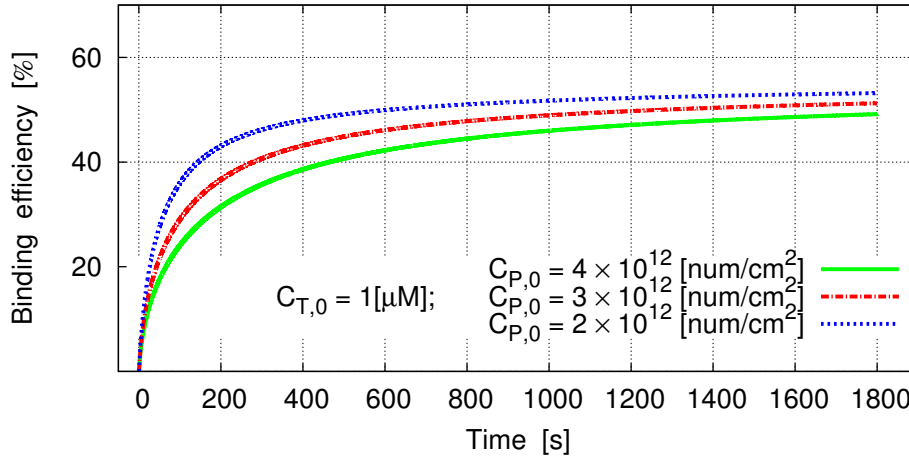


Figure 4.4: Target hybridization kinetics as a function of probe densities obtained by the simulations at the room temperature of 25 °C. The probe density varies from 2×10^{12} to 4×10^{12} molecules/cm².

It has been shown in Ref. [54] that the hybridization efficiencies are $\approx 35\%$ and $\approx 50\%$ at probe concentrations of 5.2×10^{12} molecules/cm² and 3×10^{12} molecules/cm², respectively, while the hybridization efficiency is $\approx 70\%$ at the concentration of 2×10^{12} molecules/cm².

Fig. 4.4 shows the correlation between the probe density and hybridization obtained by our simulations. Despite of the absence of the electrostatic effects, a slight difference of binding efficiencies is observed, as demonstrated in Fig. 4.4.

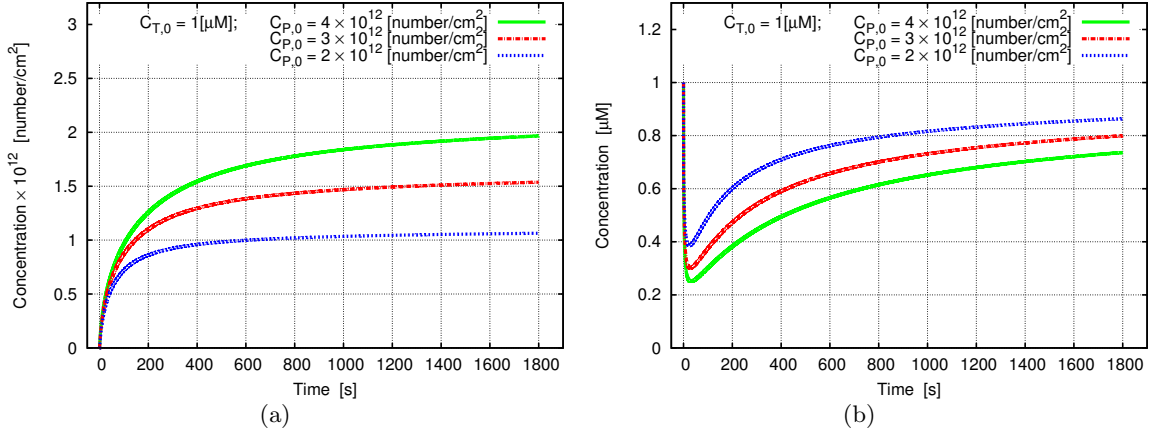


Figure 4.5: Simulation results obtained at different probe densities. (a) Density of probe-target complexes as a function of time. (b) Transport of target molecules to the functionalized surface.

The comparison of graphics in Fig. 4.4 and Fig. 4.5 demonstrates that a higher probe density (green lines) leads to a faster binding process at the beginning and to a decrease of total analyte concentration in the solution. Therefore, the transport of target molecules to the functionalized surface decreases as well (see Fig. 4.5 b). Accordingly, the weaker transport, despite of the generation of a larger amount of molecules (Fig. 4.5 a), results in a lower binding efficiency (Fig. 4.4).

4.4 Conclusions

In this chapter we deal with the different types of the chemical reactions occurring near the functionalized surface. We also focus on the influence of the diffusion transport of target molecules on the efficiency of the hybridization process. The diffusion equation with the time-varying boundary conditions comprising the chemical reactions at the surface is transformed to well-studied reaction-diffusion problem with Neumann and Dirichlet boundary conditions. Moreover, the number of unknowns is reduced to one.

The developed model and algorithm are applicable for the small initial concentration of the analyte molecules and for the specific as well the non-specific chemical reactions. The model is also suitable for modeling of the immobilization of probe molecules to the surface. In this case $r_a = r_d = 0$ and k_a and k_d are appropriate immobilization parameters. The resulting equations were implemented by using the discretized conservative scheme. That allowed to conserve exactly the total number of biomolecules, which are present in the system.

The model can be easily expanded to include the hybridization of mismatched and partially matched DNA [55]. In this case we shall consider two additional ODE, like (4.7), with corresponding hybridization parameters, and modify the equation (4.6) in an analogous way.

In the simulation step we study the effect of the diffusive mass transport on the rate of the reactions and can conclude that, even with the weak transport, a difference in the calculated binding efficiencies is observed. We also found that the non-specific chemical reaction play the major role in a detection mechanism because it affects the speed of the hybridization process by reducing the number of free target molecules.

Chapter 5

Self-consistent model

We consider the same problem as in Section 2.2 with the same definitions. In order to couple the microscopic and the macroscopic simulations together, the original Poisson equation (2.1) is replaced by a homogenized problem, which has been proposed in refs. [30,32,60]. The left-hand side of the homogenized Poisson equation depends on the distribution of the electrons and the holes, and no longer depends on the charge distributions of the analyte ions and the biomolecules

$$-\nabla \cdot (\varepsilon(\mathbf{x})\nabla\Psi_I(\mathbf{x})) = \varrho \quad (5.1)$$

$$\varrho = \begin{cases} q(p(\mathbf{x}) - n(\mathbf{x}) + \varrho_d - \varrho_a), & \text{in } \Omega_{Si}, \\ 0 & \text{in } \Omega_{Ox}, \\ 0 & \text{in } \Omega_{Liq}, \end{cases}$$

where ε is the permittivity, n and p are the concentrations of the electrons and holes, ϱ_d and ϱ_a denote the concentrations of electrically active donor and acceptor atoms, respectively.

We define the border between Ω_{Liq} and Ω_{Ox} as Γ with "+"-side from Ω_{Liq} -direction and "-"-side from Ω_{Ox} -direction, i.e., Γ_+ and Γ_- , respectively. We also denote the internal potential calculated at the interface from the side of the liquid (i.e., at Γ_+) as $\Psi_I(x+, y, z)$ and at the interface Γ_- as $\Psi_I(x-, y, z)$. The link between the insulator and the aqueous solution is realized by the following interface conditions

$$\Psi_I(x+, y, z) - \Psi_I(x-, y, z) = -\frac{\mathcal{D}}{\varepsilon_{Ox}}, \quad (5.2)$$

$$\varepsilon_{Liq} \Psi_I(x+, y, z) - \varepsilon_{Ox} \Psi_I(x-, y, z) = -\mathcal{C}, \quad (5.3)$$

where \mathcal{C} is the macroscopic surface charge density, which causes the jump in the electric field, and \mathcal{D} is the macroscopic dipole moment density, which causes the jump in the potential. \mathcal{C} and \mathcal{D} are unknown parameters, which shall be obtained from the microscopic simulations. Note that the notation ϱ is defined for oxide-surface charge density.

5.1 Compilation procedures

The whole simulation consists of several steps as follows:

Step 1: We recalculate the oxide-surface charge density by using the site-dissociation model given in Section 2.2.4. The dependence of the surface charge density of SiO_2 on the pH-value of the solution is shown in Fig. 5.1

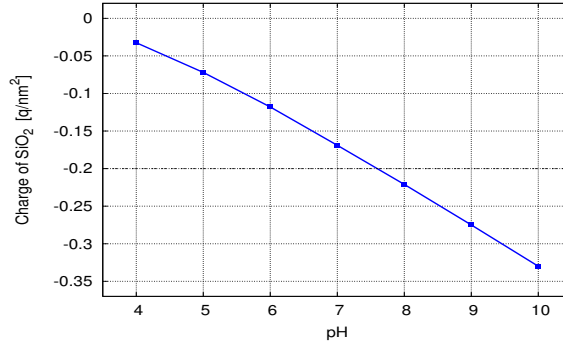


Figure 5.1: Influence of pH-value on the SiO_2 surface charge density.

Step 2: The Metropolis Monte Carlo algorithm in the constant-voltage ensemble, which is given in Section 3, is applied to find the ionic concentrations χ near the insulator-electrolyte interface and within the intermolecular space until the electrolyte bulk, i.e. in the boundary layer. Under *electrolyte bulk* we understood the space where the concentration of the anions and cations are equal. The thickness of the boundary layer on the functionalized surface L_{bl} is quantified as well. At first, the simulation is performed with the surface that is functionalized with probe molecules, which have a known density, and then the MMC is applied to the probe-target complexes with the same density. At both sub-steps the recalculated charge density for insulator-electrolyte interface is used.

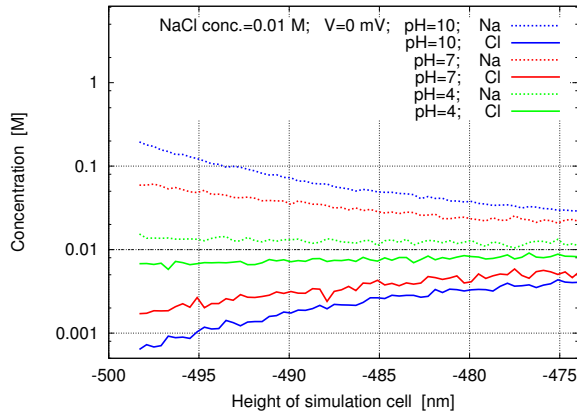


Figure 5.2: Concentration profiles near the non-functionalized surface for a bulk concentration of $0.01mM$ at backgate voltage of $0V$ and at different pH values.

Fig. 5.2 shows the ionic concentration profiles near the non-functionalized surface, which

are calculated for different pH-values of the electrolyte solution and without applied voltage. The difference in the charge distribution indicates the necessity of the recalculation of the surface charge density of the insulator.

Step 3: For coupling the atomistic and the continuum models, the microscopic charge distributions χ from the MMC solver are recalculated to the macroscopic surface charge densities \mathcal{C}_i and to the macroscopic dipole moment densities \mathcal{D}_i as follows

$$\mathcal{C}_i = \int_0^{L_{\text{bl}}} \chi(y) dy, \quad \mathcal{D}_i = \int_0^{L_{\text{bl}}} y \chi(y) dy, \quad (5.4)$$

where i denotes the simulation.

Step 4: The initial-boundary-value problem, which is described by the system of the diffusion and the reaction equations (4.5) - (4.10), is solved and the distribution and the binding efficiency of the captured κ_s as well as of the non-specifically bounded target molecules κ_n are determined. Indices s and n denote specific and non-specific binding.

Step 5: Furthermore, in the chemical equilibrium three types of biomolecules are linked to the surface: bounded complexes (bc), e.g., PNA-ssDNA(T) or ssDNA(P)-ssDNA(T), single, non-bounded molecules (nb), e.g., PNA or ssDNA(P), and non-specifically bounded molecules (ns), e.g., ssDNA(T), where (P) and (T) denote probe and target molecules, respectively. Hence, the macroscopic surface charge and dipole moment densities include in fact three terms

$$\begin{aligned} \mathcal{C} &= \kappa_s \mathcal{C}_{bc} + (1 - \kappa_s) \mathcal{C}_{nb} + \kappa_n \mathcal{C}_{ns}, \\ \mathcal{D} &= \kappa_s \mathcal{D}_{bc} + (1 - \kappa_s) \mathcal{D}_{nb} + \kappa_n \mathcal{D}_{ns}. \end{aligned} \quad (5.5)$$

Hence, \mathcal{C}_i and \mathcal{D}_i are weighted by the binding efficiencies κ_s and κ_n and used as interface conditions in the homogenized model (5.1) - (5.3).

Note that the ionic charge distributions shall be calculated for each type of the functionalized surface, namely for "bc", "nb" and "ns" separately.

Step 6: Afterwards the homogenized model (5.1) - (5.3) coupled with the drift-diffusion model given in Section 2.2.1 is solved by using the calculated value of \mathcal{C} and \mathcal{D} . The solution provides the voltage for MMC and the external potential for the migration model.

Step 7: A self-consistent loop between the micro- and macroscopic simulations provides the basis for the quantitative description of BioFETs and their predictive simulation. For simplicity we can calculate the look-up tables of \mathcal{C} and \mathcal{D} values as functions of the discrete value of the surface potential. Then, in the self-consistent loop, we can choose from these tables approximate values of \mathcal{C} and \mathcal{D} , which correspond to the calculated surface potential.

5.2 Simulation results

In this section we investigate the micro- and macroscopic simulations separately and in a self-consistent loop. For this goal we consider three test-simulations. For the first simulation we choose discrete values of the macroscopic surface charge and the dipole moment densities and calculate the electrical conductance of the device analogously as in the step 6 of the algorithm. The *electrical conductance* is defined as a current between the source and the drain divided by a potential difference between the source and the drain. In the second test we study the macroscopic surface charge and the dipole moment densities, which are calculated for some discrete values of the surface potential for different types of the surface functionalizations. The self-consistent loop is investigate in the third test.

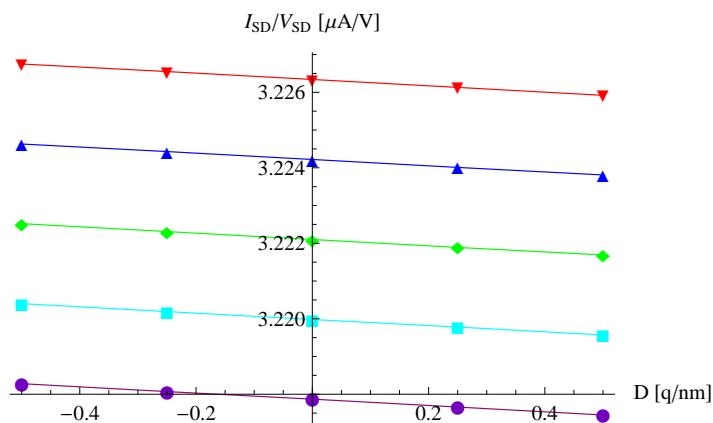


Figure 5.3: Electrical conductance as a function of the dipole moment density \mathcal{D} of the bio-functionalized surface layer for different values of the surface charge density \mathcal{C} . The bottom line is for $\mathcal{C} = -0.5 \text{ q/nm}^2$. The top line is for $\mathcal{C} = 0.5 \text{ q/nm}^2$. The step size in \mathcal{C} is 0.125 q/nm^2 .

Fig. 5.3 shows a conductance as a function of dipole moment density for different values of the surface charge density \mathcal{C} , which is changed from -0.5 q/nm^2 (bottom line) to $+0.5 \text{ q/nm}^2$ (top line). We see that not only surface charge density \mathcal{C} but also the dipole moment density \mathcal{D} is important for self-consistent loop between microscopic and macroscopic simulations.

Surface charge density \mathcal{C} and dipole moment density \mathcal{D} , as a function of the applied voltage varying from -250 mV to 250 mV are presented in Fig. 5.4. Here we assume that $\kappa_s = 1$ and $\kappa_n = 0$, i.e. we have an optimal binding. By the simulation without molecules and without applied voltage the surface charge density increases from -0.2 q/nm to -0.1 q/nm , which is shown in the middle of the green line marked with triangles. Hence, the screening of the surface charge by the counter-ions is about 50%.

Fig. 5.5 shows the macroscopic surface charge density \mathcal{C} and the macroscopic dipole moment density \mathcal{D} as a function of applied voltage, varying from -5 V to 5 V . The three types of the insulator are given by their surface charge density. All simulations show that there is an interval in the middle in which the dependence of dipole moment density on applied

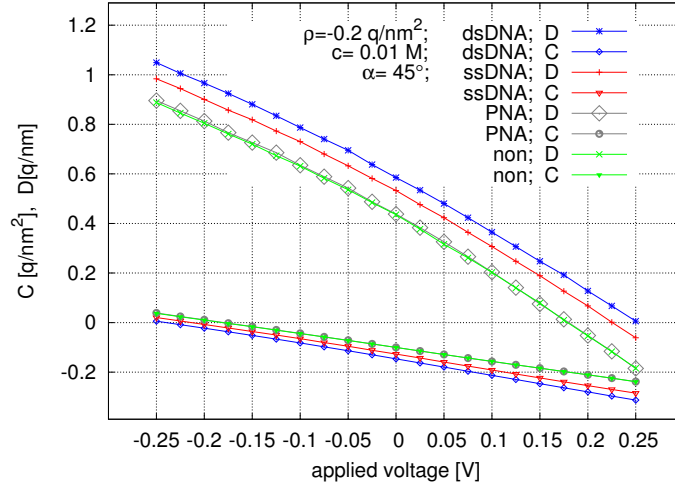


Figure 5.4: Surface charge density \mathcal{C} and dipole moment density \mathcal{D} as a function of applied voltage for no molecules, for a 10-mer of PNA, ssDNA, and dsDNA, for an angle of the oligomer of $\alpha = 45^\circ$ with respect to the surface, for a oxide-surface charge density of $\rho = -0.2 \text{ q/nm}^2$, for a bulk concentration of 0.01 M, and for applied potentials of -250 mV to 250 mV . The macroscopic surface charge and dipole moment densities are of the same order of magnitude.

potential is almost linear. A further increase or decrease of the applied potential leads to extrusion of the negative or positive ions far from the surface, respectively. If the potential reaches a certain value, i.e. -1.5 V or 1.5 V (see the blue line with triangles), only one type of ions remains in the boundary layer $[0; L_{bl}]$ and the dipole moment density increases or decreases, respectively.

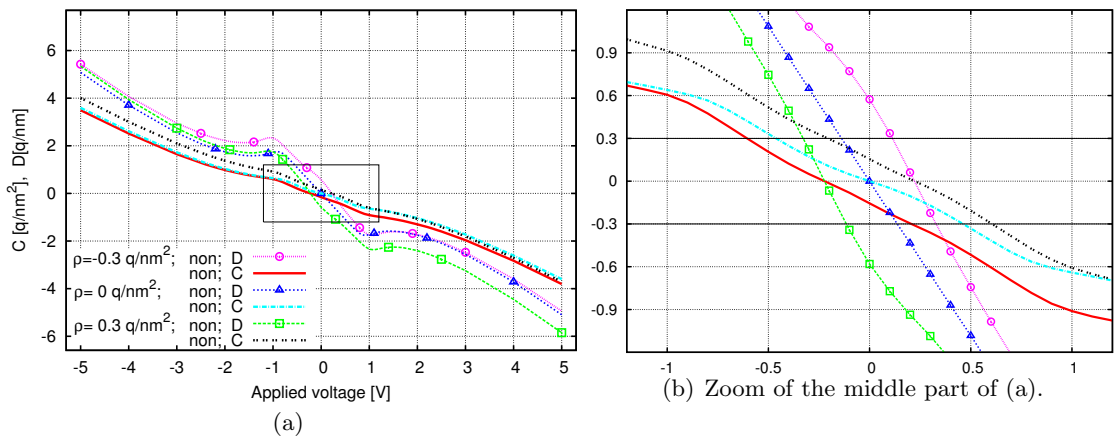


Figure 5.5: Surface charge density \mathcal{C} and dipole moment density \mathcal{D} as a function of applied voltage calculated without biomolecules for different oxide-surface charge densities, for a bulk concentration of 0.01 M, and for applied potentials of -5 V to 5 V . The macroscopic surface charge and dipole moment densities are of the same order of magnitude.

In Fig. 5.6 the simulations of the surface charge density and the dipole moment density with different molecules and an uncharged insulator are compared. The appreciable difference especially in value of the dipole moment density is shown for the small and positive applied voltage.

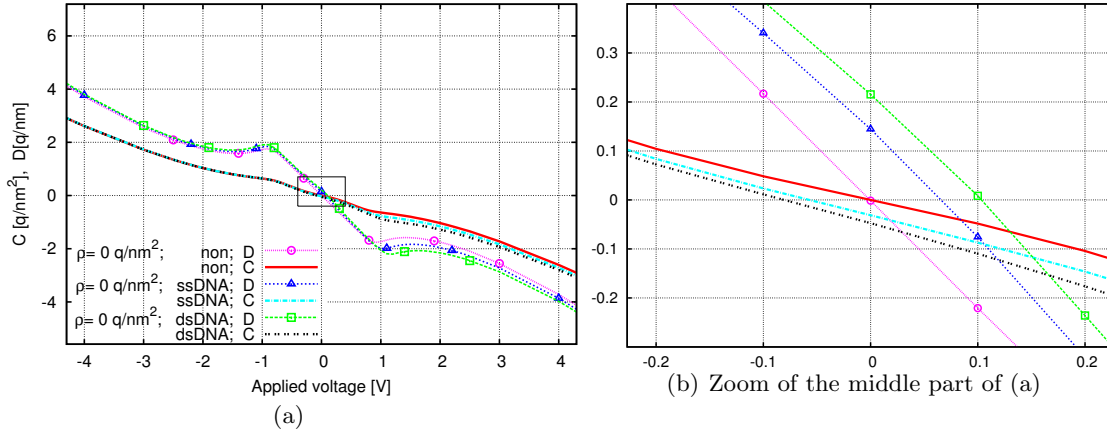


Figure 5.6: Surface charge density \mathcal{C} and dipole moment density \mathcal{D} as a function of applied voltage for no molecules, for a 10-mer of ssDNA and dsDNA, for an angle of the oligomer of $\alpha = 45^\circ$ with respect to the surface, for an uncharged oxide-surface, for a bulk concentration of 0.01 M, and for applied potentials of $-4V$ to $4V$. The macroscopic surface charge and dipole moment densities are of the same order of magnitude.

In the last test-simulation we consider a small rectangular semiconductor with measurements $10nm \times 13nm \times 100nm$ that is shown in Fig. 5.7(a). The source, the drain, the electrode and the bulk contacts have applied potentials of $-1V$, $0V$, $0V$ and $-3.8V$, respectively. The input parameters for MMC solve are given in the Table 5.1. Here the optimal binding is as-

Table 5.1: The input parameters for MMC solver.

Input parameters	Value
type of the biomolecules	ssDNA
length of the biomolecules	10bp
angle between biomolecule and surface	90
length of linkers	1nm
type of the electrolyte ions	Na^+Cl^-
concentration of the used ions	0.001M
number of molecules at the surface	3×3
distance between them	8nm
charge of the insulator	$-0.2q/nm^2$

sumed. Fig. 5.7 show the electrical potential as a function of space which is calculated in the self-consistent loop with the microscopic model. The figures (b), (c) and (d) display potentials at the cross sections of the device, which are made in the middle of the semiconductor.

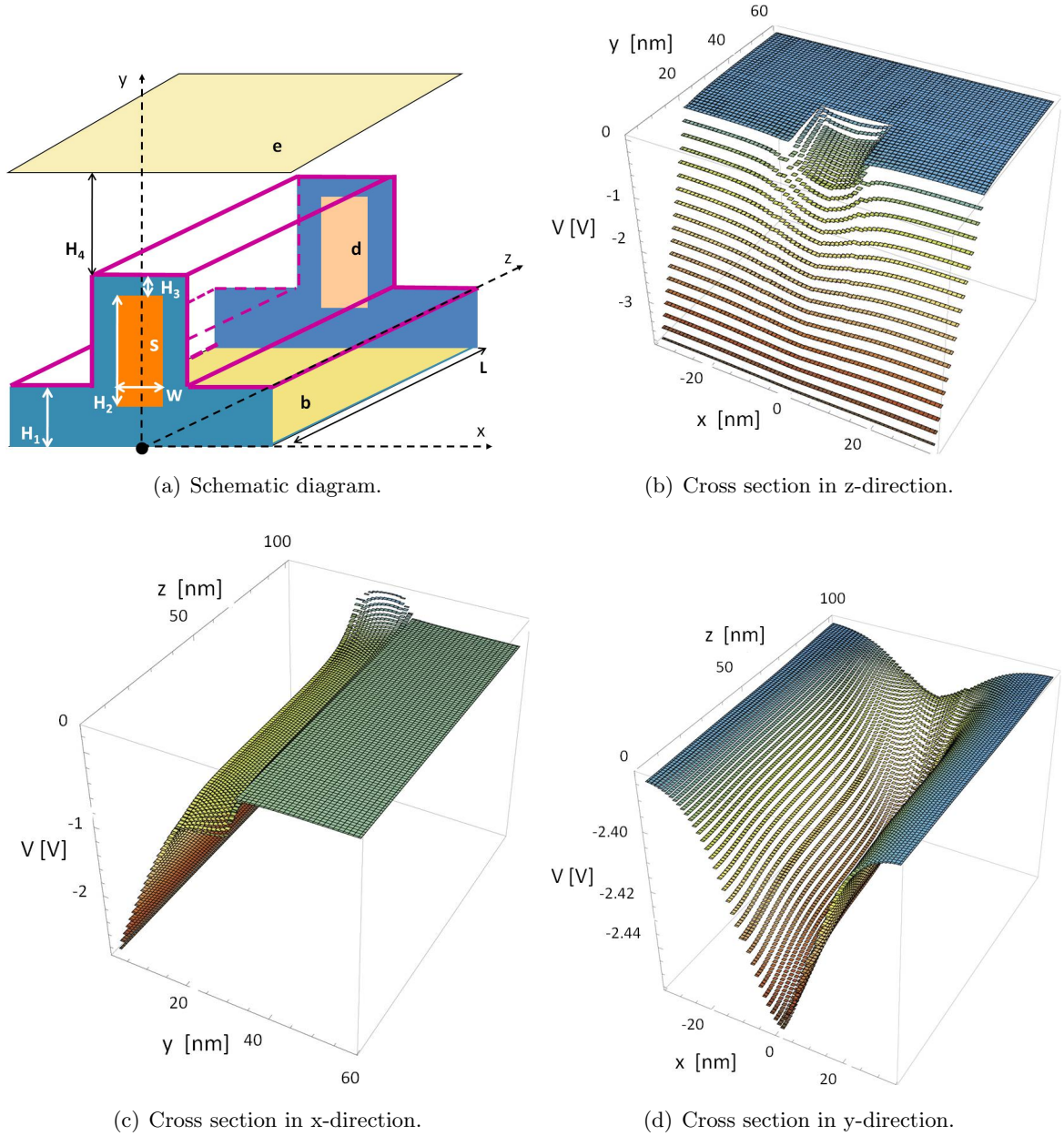


Figure 5.7: Schematic diagram and cross sections made in the middle of the semiconductor. The cross sections show the electric potential as a function of space. s , d , b , e denote the source, drain, bulk contact and electrode, which have applied potentials of -1V , 0V , -3.8V and 0V , respectively. The device has following geometrical parameters: $H_1 = 18\text{nm}$, $H_2 = 10\text{nm}$, $H_3 = 2\text{nm}$, $H_4 = 25\text{nm}$, $W = 13\text{nm}$ and $L = 100\text{nm}$.

5.3 Conclusions

We present a self-consistent 3D model for DNA-modified FET. This model consists of four general parts which are connected with each other via the compilation scheme. The advantage of this technique is that the transport of the target molecules, the surface reactions, and the liquid behavior are modeled independently from the physical part of the model of our sensor and, therefore, can be correctly approximated by using a necessary and a judicious tradeoff between realism and simplicity.

We find the influence of the charge and especially of the dipole moment densities of the boundary layer to the electrical conductance. And we can conclude that the thickness of the boundary layer is significant for the response signal. We also study the influence of the applied potential (between the functionalized surface and the electrode) to the surface charge and dipole moment and find that only small and opposite to the net surface charge voltage has a noticeable influence. Therefore, the change in dipole moment after binding of analyte molecules effects the detection mechanism.

Chapter 6

Stochastic processes at the functionalized surface

We consider an isolated sensor that is immersed in an analyte solution. The reactive solid surface $\partial\Omega_s$ of area A of the sensor is functionalized with $C_{P,0}$ receptors (probe molecules) per unit area, and the solution contains target molecules with initial concentration $C_{T,0}$ mole per liter. We will use below the notations P and T for probe and target molecules, respectively. We denote the molecule after binding event as PT (probe-target complex) and its initial concentration as $C_{PT,0}$.

Hence we work with following concentration functions:

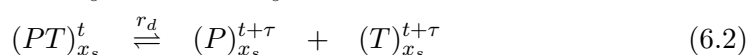
$$C_T = C_T(t, \mathbf{x}), C_P = C_P(t) \text{ and } C_{PT} = C_{PT}(t), \text{ where}$$

$$0 \leq C_T(t, \mathbf{x}) \leq C_{T,0}, 0 \leq C_P(t) \leq C_{P,0} \text{ and } 0 \leq C_{PT}(t) \leq \min[C_{T,0}, C_{P,0}].$$

We also assume initial the concentrations $C_{T,0}$ and $C_{P,0}$ to be uniform and $C_{PT,0} = 0$.

6.1 Interaction processes

The association and dissociation processes which occur at the surface x_s can be schematically depicted as follows



The equation (6.1) denotes a binding process of target molecules T , which are located in position x_s at the time t , with probe molecules P , where captured molecules PT are build during a small interval $\tau := \Delta t$. Analogously the equation (6.2) describes dissociation processes, in which the probes and targets are generated.

The rates λ_a and λ_d of the association and dissociation processes are characterized by the

constants r_a and r_d , respectively.

Number of binding events per unit time and unit area:

$$\lambda_a := \frac{C_{PT}(t + \tau) - C_{PT}(t)}{\tau} = r_a C_T(t, x_s) C_P(t) \quad (6.3)$$

Number of dissociation events per unit time and unit area:

$$\lambda_d := \frac{C_P(t + \tau) - C_P(t)}{\tau} = r_d C_{PT}(t) \quad (6.4)$$

6.2 Chemical Langevin equation at the surface

To quantify the biological noise of the system we treat the reaction at the surface as a stochastic process, i.e., the bond of probe and target molecules occur in an essentially random manner. Langevin equations for chemical reactions inside some fixed volume have been discussed recently in [24, 33]. Here we obtain the Langevin equation for a association/dissociation processes at the surface.

We consider a system of n_P particles (probe molecules) at the time $t = j\tau$ ($\tau := \Delta t$) with following indicator function

$$\omega_i^j = \begin{cases} 1 & i\text{-th probe is bounded at the time } t = j\tau, \\ 0 & \text{otherwise,} \end{cases}$$

where ω_i^j are independent random variables, and $i = 1, 2, \dots, n_P$. In these notations the number of probe-target complexes PT and the number of single probes P at the time t can be written as $\sum_i \omega_i^j$ and $n_P - \sum_i \omega_i^j$ respectively. We denote a new random variable $X(t) := \frac{\sum_i \omega_i^j}{A}$ which describes the dynamic state of the system, where $t = j\tau$ and $X(t) \in [0, \dots, C_{P,0}]$.

Lemma 6.2.1. (The chemical Langevin equation at the surface)

Let $X_t := X(t)$ be a stochastic variable describing the probe-target binding at the time t . The binding process is specified by the first order chemical reactions occurring at the functionalized surface x_s , which are given by equations (6.1) and (6.2). Let $\frac{d[B_1(t)]}{dt}$ and $\frac{d[B_2(t)]}{dt}$ be statistically independent Gaussian white noises according to association and dissociation processes, respectively. Then the evolution of $X(t)$ from the given initial state $X(0) = x_0$ is described by the following equation

$$\begin{aligned} \frac{dX_t}{dt} &= r_a (C_{P,0} - X_t) C_T(t, x_s) - r_d X_t \\ &+ \sqrt{r_a (C_{P,0} - X_t) C_T(t, x_s)} \frac{d[B_1(t)]}{dt} - \sqrt{r_d X_t} \frac{d[B_2(t)]}{dt} \end{aligned} \quad (6.5)$$

Proof. Let $K_a(X_t, t)$ and $K_d(X_t, t)$ be numbers of association and dissociation events, respectively, which occur in the subsequent time interval $[t, t + \tau]$. The change in PT complexes

during the small time interval τ can be written as follows

$$\begin{aligned} X_{t+\tau} - X_t &= K_a(X_t, t) - K_d(X_t, t), \\ K_a(X_t, t) &= (C_{P,0} - X(t))p_a, \\ K_d(X_t, t) &= X(t)p_d, \end{aligned} \tag{6.6}$$

where p_a is a probability that *one single probe molecule* will react in the next time interval τ (association event has occurred) and p_d is a probability of dissociation process of *one complex PT*, which can be derived from the equations (6.3) and (6.4).

$$\begin{aligned} p_a &= \frac{C_{PT}(t+\tau) - C_{PT}(t)}{C_P(t)} \stackrel{(6.3)}{=} \tau r_a C_T(t, x_s), \\ p_d &= \frac{C_P(t+\tau) - C_P(t)}{C_{PT}(t)} \stackrel{(6.4)}{=} \tau r_d \end{aligned}$$

Thus, the rates λ_a and λ_d can be defined as functions of X_t

$$\begin{aligned} \lambda_a(X_t) &:= \frac{K_a(X_t, t)}{\tau} = r_a C_T(t, x_s) (C_{P,0} - X_t) \\ \lambda_d(X_t) &:= \frac{K_d(X_t, t)}{\tau} = r_d X_t \end{aligned} \tag{6.7}$$

Remark. Let \bar{p}_a be a probability that the free target is bounded during the time interval τ (association event has occurred).

$$\bar{p}_a := \frac{C_{PT}(t+\tau) - C_{PT}(t)}{C_T(t, x_s)} \stackrel{(6.3)}{=} r_a \tau C_P(t) = r_a \tau (C_{P,0} - X(t)).$$

In this case the expectation of the first term on the right-hand side of the eq. (6.6) can be written as

$$K_a(X_t, t) = C_T(t, x_s) r_a \tau (C_{P,0} - X(t)),$$

where $C_T(t, x_s)$ is the number of free targets at the surface. Putting all together we obtain the same rate λ_a as in (6.7).

If τ is large enough, i.e., $\tau\lambda_a \gg 1$ and $\tau\lambda_d \gg 1$ (it means that more than one events occurs during this time interval), the random variables $K_j(X_t, t)$, $j = a, d$ are statistically independent Poisson random variables $\mathcal{P}_j(\lambda_j(X_t), \tau)$ with mean value and variance equal to $\tau\lambda_j(X_t)$. $\mathcal{P}_j(\lambda_j(X_t), \tau)$ can be approximated by a normal random variable with the same mean and variance, i.e., $\mathcal{N}_j(\tau\lambda_j(X_t), \tau\lambda_j(X_t))$.

We rewrite the equation (6.6) by using $\tau = \Delta t \rightarrow dt$, $X_t := X(t)$ and the linear combination theorem for normal random variables $\mathcal{N}(m, \sigma^2) = m + \sigma\mathcal{N}(0, 1)$.

$$\begin{aligned} X(t+dt) &= X(t) + \lambda_a(X_t)dt - \lambda_d(X_t)dt \\ &\quad + \sqrt{\lambda_a(X_t)}\sqrt{dt}\mathcal{N}_a(0, 1) - \sqrt{\lambda_d(X_t)}\sqrt{dt}\mathcal{N}_d(0, 1) \end{aligned} \tag{6.8}$$

$$\begin{aligned}
 X(t + dt) &= X_t + \left(r_a(C_{P,0} - X_t)C_T(t, x_s) - r_d X_t \right) dt \\
 &\quad + \sqrt{r_a(C_{P,0} - X_t)C_T(t, x_s)} \sqrt{dt} \mathcal{N}_a(0, 1) - \sqrt{r_d X_t} \sqrt{dt} \mathcal{N}_d(0, 1) \quad (6.9)
 \end{aligned}$$

$$\begin{aligned}
 \frac{dX_t}{dt} &= r_a(C_{P,0} - X_t)C_T(t, x_s) - r_d X_t \\
 &\quad + \sqrt{r_a(C_{P,0} - X_t)C_T(t, x_s)} \frac{d[B_1(t)]}{dt} - \sqrt{r_d X_t} \frac{d[B_2(t)]}{dt} \quad (6.10)
 \end{aligned}$$

Equations (6.9) and (6.10) are called standard-form and white-noise form Langevin equations, respectively, where $\frac{d[B_1(t)]}{dt} = \frac{\mathcal{N}_a(0,1)}{\sqrt{dt}}$ and $\frac{d[B_2(t)]}{dt} = \frac{\mathcal{N}_d(0,1)}{\sqrt{dt}}$ are statistically independent Gaussian white noises. \square

Remark. Eq. (6.5) in integral form with initial condition is

$$\begin{aligned}
 X(t) &= X(0) - \int_0^t \left(X(s) \left(r_a C_{P,0} + r_d \right) + r_a C_{P,0} C_T(s, x_s) \right) ds \\
 &\quad + \int_0^t \sqrt{r_a(C_{P,0} - X(s))C_T(s, x_s)} dB_1(s) - \int_0^t \sqrt{r_d X(s)} dB_2(s), \\
 X(t) \Big|_{t=0} &= 0 \quad (6.11)
 \end{aligned}$$

6.3 Signal-to-Noise Ratio

As in all sensors, the most important characteristics of biosensor systems is their signal-to-noise ratio (SNR). In this paper we regard the biological noise. To find this ratio, we should identify the signal as well as noise sources.

Definition 6.3.1. If we consider hybridization events occurring at the time t as *signals* $X(t)$, the *noise* can be defined as a standard deviation of the probe-target complexes and the SNR will be the expectation of captured molecules over the corresponding standard deviation

$$\text{SNR}(t) = \frac{\mathbb{E}[X(t)]}{\sqrt{\text{Var}[X(t)]}}.$$

Remark. In physics the signal-to-noise ratio is usually expressed in decibels (dB) given by the formula: $10 \times \log_{10}(\text{SNR})$.

Lemma 6.3.1. *The signal-to-noise ratio can be computed explicitly*

$$\text{SNR}(t) = \frac{1 - e^{-\delta t}}{\sqrt{b_3 e^{-3\delta t} - b_2 e^{-2\delta t} + b_1 e^{-\delta t} + b_0}},$$

and is bounded in time

$$0 < \text{SNR}(t) \leq \sqrt{\frac{r_a}{r_d} C_{P,0} C_T(t, x_s)} < \sqrt{\frac{r_a}{r_d} C_{P,0} \bar{y}}, \quad \forall t > 0,$$

where b_0, b_1, b_2, b_3 and δ are functions of $C_T(t, x_s)$ and \bar{y} is a constant.

Proof. For simplicity we use the following notations $y(t) := C_T(t, x_s)$ and $c := C_{P,0}$.

- *The expectation*

We consider the equation (6.5) and calculate the mean value of its left and right part:

$$\frac{d\mathbb{E}[X(t)]}{dt} = -\mathbb{E}[X(t)](r_d + r_a y(t)) + r_a c y(t)$$

The solution is a function of $y(t)$

$$\mathbb{E}[X(t)] = \frac{r_a y(t) c}{r_d + r_a y(t)} \left(1 - e^{-(r_a y(t) + r_d)t}\right). \quad (6.12)$$

- *The variance:* The SDE under following notations $u(X) = r_a y(t)(c - X(t))$ and $v(X) = r_d X(t)$ is

$$\frac{dX_t}{dx} = u(X_t) - v(X_t) + \sqrt{u(X_t)} \frac{d[B_1(t)]}{dt} - \sqrt{v(X_t)} \frac{d[B_2(t)]}{dt}$$

Applying Ito's formula [2] to $H(X_t) := X^2(t)$, where $\frac{\partial H(X_t)}{\partial x} = 2X(t)$, $\frac{\partial^2 H(X_t)}{\partial x^2} = 2$, $\frac{\partial H(X_t)}{\partial t} = 0$, and because $H(X_t)$ does not depend explicitly on t , we have

$$\begin{aligned} dH(X_t) &= \frac{\partial H(X_t)}{\partial t} dt + \frac{\partial H(X_t)}{\partial x} dX + \frac{1}{2} \frac{\partial^2 H(X_t)}{\partial x^2} \left(u(X_t) + v(X_t)\right) dt \\ d(X_t)^2 &= 2X \left(u(X_t)dt - v(X_t)dt + \sqrt{u(X_t)}d[B_1(t)] - \sqrt{v(X_t)}d[B_2(t)]\right) + \left(u(X_t) + v(X_t)\right)dt \end{aligned}$$

$$\begin{aligned} dX^2(t) &= \left(u(X) + v(X) + 2(u(X) - v(X))X(t)\right)dt \\ &\quad + 2\sqrt{u(X)}X(t)d[B_1(t)] - 2\sqrt{v(X)}X(t)d[B_2(t)] \\ &= \left(r_a y(t)(c - X(t)) + 2r_a y(t)(c - X(t))X(t) + r_d X(t) - 2r_d X^2(t)\right)dt \\ &\quad + \sqrt{4r_a y(t)(c - X(t))X^2(t)}d[B_1(t)] - \sqrt{4r_d X^3(t)}d[B_2(t)] \end{aligned}$$

$$\begin{aligned} \frac{dX^2(t)}{dt} = & X^2(t) \left(-2r_a y(t) - 2r_d \right) + X(t) \left(r_a y(t)(2c - 1) + r_d \right) + r_a y(t)c \\ & + \sqrt{4r_a(c - X(t))X^2(t)y(t)} \frac{d[B_1(t)]}{dt} - \sqrt{4r_d X^3(t)} \frac{d[B_2(t)]}{dt} \end{aligned}$$

By taking the expectation, we have

$$\begin{aligned} \mathbb{E} \left[\frac{dX^2(t)}{dt} \right] = & \frac{d\mathbb{E}[X^2(t)]}{dt} = -\mathbb{E}[X^2(t)] \left(2r_a y(t) + 2r_d \right) \\ & + \mathbb{E}[X(t)] \left(r_a y(t)(2c - 1) + r_d \right) + r_a y(t)c \end{aligned}$$

where $\mathbb{E}[X(t)]$ is given by (6.12).

The solution of the equation above is a function of $y(t)$

$$\mathbb{E}[X^2(t)] = \frac{\mathbb{E}[X(t)] \left(r_a y(t)(2c - 1) + r_d \right) + r_a y(t)c}{2(r_a y(t) + r_d)} \left(1 - e^{-2(r_a y(t) + r_d)t} \right).$$

Therefore $\text{Var}[X(t)] = \mathbb{E}[X^2(t)] - \left(\mathbb{E}[X(t)] \right)^2$.

- *The signal-to-noise ratio*

Let us introduce the following notations:

$$\begin{aligned} r &:= r_a/r_d, & \delta &:= r_a y(t) + r_d, \\ \alpha &:= r y(t) + 1, & \beta &:= r y(t)c, & \gamma &:= r y(t) - 1, \\ a_1 &:= \frac{\beta\gamma}{2\alpha^2}, & a_2 &:= \frac{\beta}{2\alpha}, & a_3 &:= \frac{\beta^2}{\alpha^2}. \end{aligned}$$

Then the mean value and the variance of process X_t will be

$$\begin{aligned} \mathbb{E}[X(t)] &= \sqrt{a_3}(1 - e^{-\delta t}), \\ \text{Var}[X(t)] &= (a_3 - a_1)e^{-3\delta t} - (a_1 + a_2)e^{-2\delta t} - (a_2 - 3a_3)e^{-\delta t} + (a_2 - a_1). \end{aligned}$$

Thus,

$$\text{SNR}(t) = \frac{1 - e^{-\delta t}}{\sqrt{b_3 e^{-3\delta t} - b_2 e^{-2\delta t} + b_1 e^{-\delta t} + b_0}},$$

where $b_0 := \frac{1}{\beta}$, $b_1 := \frac{\gamma}{2\beta} - 3$, $b_2 := \frac{\alpha + \gamma}{2\beta}$ and $b_3 := 1 - \frac{\gamma}{2\beta}$.

- *In the equilibrium state*

The number of target molecules at the surface in chemical equilibrium can be either calculated by using, for instance, diffusion equation or can be kept constant $y(\infty) = C_T(\infty, x_s) < \varepsilon \ll$

$C_{T,0}$, where ε is a small constant. Because the system doesn't have any external influence (interaction), we expect that in the chemical equilibrium the balance between association and dissociation processes exists, i.e.

$$\lim_{t \rightarrow \infty} \frac{d\mathbb{E}[X(t)]}{dt} = -\mathbb{E}[X(\infty)](r_d + r_a y_\infty) + r_a y_\infty C_{P,0} = 0,$$

where $X_\infty := X(\infty)$ is the notation of bounded probes $X(t)$ if the system is in equilibrium.

$$0 \leq E_\infty := \mathbb{E}[X_\infty] = \frac{r_a y_\infty c}{r_d + r_a y_\infty} < \infty. \quad (6.13)$$

$$\lim_{t \rightarrow \infty} \mathbb{E}[X^2(t)] = \mathbb{E}[X^2(\infty)] = \frac{E_\infty (r_a y_\infty (2c - 1) + r_d) + r_a y_\infty c}{2(r_a y_\infty + r_d)}.$$

As a result

$$\text{Var}[X(\infty)] = \frac{r_a r_d c y_\infty}{(r_a y_\infty + r_d)^2} \quad \text{and} \quad \text{SNR}(\infty) = \sqrt{\frac{r_a}{r_d} y_\infty c}.$$

The model equations for evaluation of $C_T(t, x_s)$ (and accordingly of y_∞) and their solution are considered in the section Section 4.1. Thus, $y_\infty = \bar{y} = \text{const} < \infty$ (see Theorem 4.1.4) and the SNR is bounded in time

$$0 < \text{SNR}(t) < \sqrt{\frac{r_a}{r_d} \bar{y} C_{P,0}}, \quad \forall t > 0.$$

□

Therefore, the lower estimation of standard deviation is given by

$$0 < \frac{\sqrt{r_a r_d c y_\infty}}{r_a y_\infty + r_d} =: \epsilon_\sigma \leq \sigma[X(\infty)] = \sqrt{\text{Var}[X(\infty)]} \quad (6.14)$$

From (6.12) and (6.13) we can also calculate the expectation of binding efficiency (BE), which is the fraction of all receptors that are bound to analyte molecules:

$$\begin{aligned} \mathbb{E}[BE(t)] &= \frac{r_a y(t)}{r_d + r_a y(t)} \left(1 - e^{-(r_a y(t) + r_d)t}\right) \times 100\% \\ \mathbb{E}[BE(\infty)] &= \frac{r_a y_\infty}{r_d + r_a y_\infty} \times 100\%. \end{aligned} \quad (6.15)$$

6.4 Simulation results

The expectation and the standard deviation

At first we consider a situation with a constant flow of analyte molecules to the functionalized surface and analyze the expectation of hybridized molecules and the corresponding standard deviation by using stochastic model described in section Section 6.3. The used nominal input parameters are summarized in Table 6.1.

Initial probe concentration	$c = C_{P,0} = 3 \times 10^{12}$ molecules/cm ² ;
Target concentration at the surface	$y(t) = 0.016 \mu\text{M} \quad \forall t$;
Association rate	$r_a = 3.0 \times 10^5 \text{ M}^{-1}\text{s}^{-1}$;
Dissociation rate	$r_d = 5.0 \times 10^{-3} \text{ s}^{-1}$.

Table 6.1: Nominal input parameters.

Fig. 6.1 shows the expected value of captured analyte molecules $\mathbb{E}[X(t)]$ and the area between $\mathbb{E}[X(t)] + \sigma[X(t)]$ and $\mathbb{E}[X(t)] - \sigma[X(t)]$ in which 67% of random variables are located, where $\sigma[X(t)] = \sqrt{\text{Var}[X(t)]}$ is corresponding standard deviation.

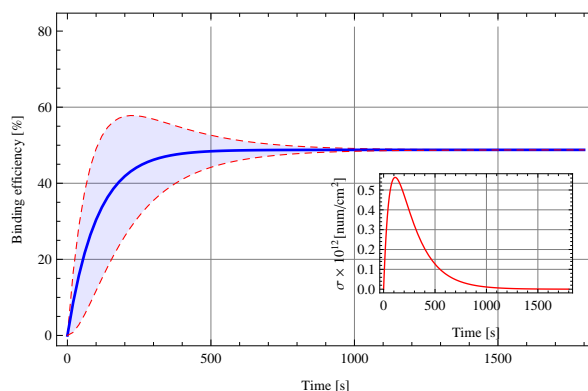


Figure 6.1: Mean value of captured analyte as a function of time. The red dashed lines are mean value plus or minus standard deviation. The corresponding standard deviation is shown in a small box. The calculations is made with probe density of 3×10^{12} molecules/cm².

We compare the proposed stochastic model with experimental results from Peterson et al. (see Refs. [54] and [55]) for target hybridization kinetics as a function of probe density. It has been shown that the hybridization efficiency is ca. 10% at the probe concentration of 12×10^{12} molecules/cm², while the hybridization efficiency is ca. 50% at the concentration of 3×10^{12} molecules/cm². The equilibrium constant r_a/r_d is obtained in the experiment ([55]) and is equal to $6 \times 10^7 \text{ M}^{-1}$.

Fig. 6.2 demonstrates the correlation between the probe density and hybridization obtained by the simulations (colored lines) and in the experiments (marked curves). In the experiments the lower probe densities lead to higher hybridization efficiencies. Because the

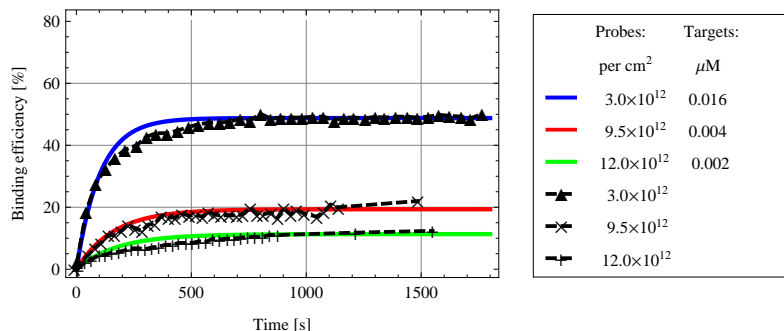


Figure 6.2: Target hybridization kinetics as a function of probe density received by experiments [54] (marked curves) and after simulations (colored lines) at the room temperature 25C. The probe density varies from 3×10^{12} to 12×10^{12} molecules/cm².

expected value of binding efficiency does not explicitly depend of the probe concentration (see (6.15)), the same result is observed by the simulations if a faster flow of analyte molecules is used for a lower probe densities. Such assumption is in agreement with the model discussed in Section 4.3. Thus, all curves obtained by the simulation at the given equilibrium constant and at the concentration of target molecules near the functionalized surface ranging from $0.002\mu\text{M}$ to $0.016\mu\text{M}$ are located between green and blue lines and binding efficiencies are constant for time $t > 1000\text{s}$.

The signal-to-noise ratio

To choose transistor design parameters for optimal operation it is useful to analyze the signal-to-noise ratio for several regions of transistor operation. The design parameters relate to a probe concentration, to a temperature, to a concentration of salt or to some other parameters, which affect analyte transport. Fig. 6.3 shows the SNR as a function of time for different probe densities and different target concentrations at the surface. The used nominal input parameters are chosen to clearly characterize the SNR and are summarized in Table 6.2. Because the initial concentration of target molecules ($1\mu\text{M}$) is not a controlled parameter we consider only a change of analyte concentration near the functionalized surface.

Initial probe concentration	$c = C_{P,0} = 5.2 \times 10^{12} \text{ molecules/cm}^2$;
Target concentration at the surface	$y(t) = 1/70\mu\text{M} \quad \forall t$;
Association rate	$r_a = 3.0 \times 10^5 \text{ M}^{-1}\text{s}^{-1}$;
Dissociation rate	$r_d = 5.0 \times 10^{-3} \text{ s}^{-1}$.

Table 6.2: Nominal input parameters.

The signal-to-noise ratios for different probe densities and different target concentrations at the surface are demonstrated in Fig. 6.3 (a). At higher probe densities and at weaker analyte transport, like those in the situation discussed above, the SNRs are also higher but they get their maximal values at a later time and, accordingly to the Fig. 6.2, the binding

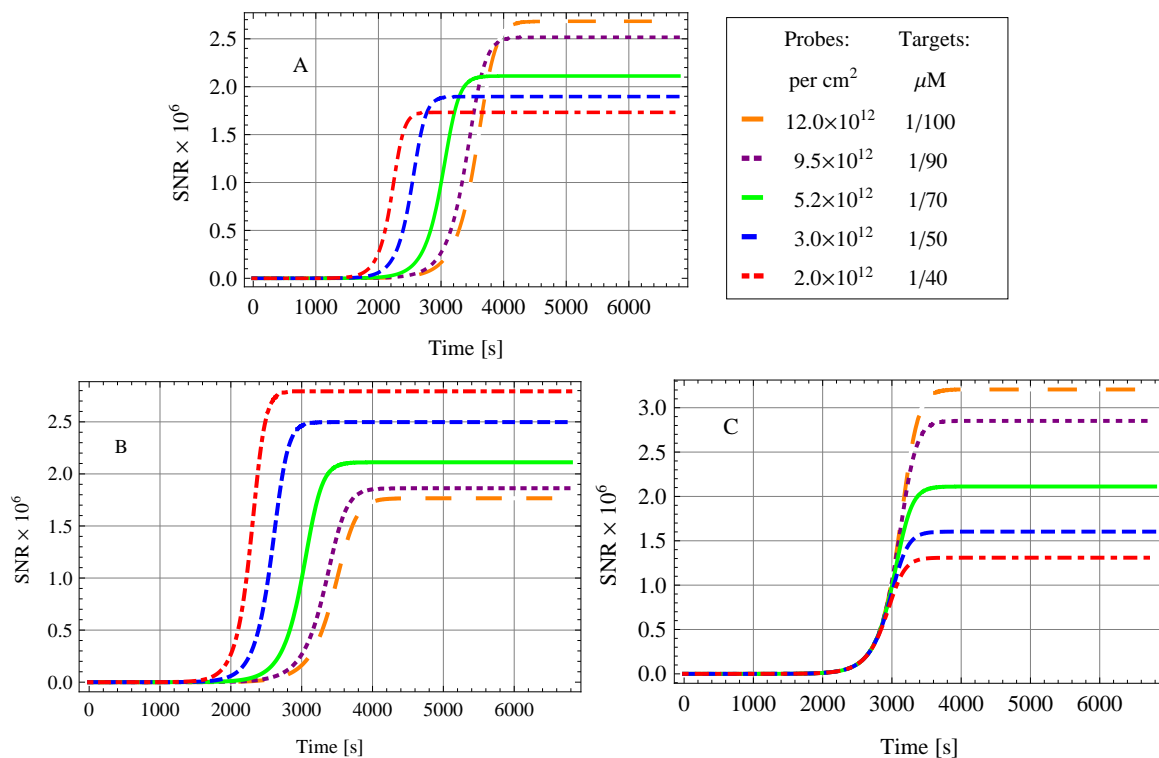


Figure 6.3: Signal-to-noise ratios (A) for different probe densities and different target concentrations at the surface, (B) for different target concentrations at the surface and the same probe density of 5.2×10^{12} molecules/cm², and (C) for different probe densities and the same target concentration of $1/70 \mu\text{M}$ at the surface. In all simulations the association and dissociation rates are $r_a = 3.0 \times 10^5 \text{ M}^{-1}\text{s}^{-1}$ and $r_d = 5.0 \times 10^{-3} \text{ s}^{-1}$.

efficiencies of captured analyte are smaller. Contrariwise, in the case of the lowest probe density and the highest analyte transport the value of the SNR is the smallest, but the advantage of the later case consist in the highest binding efficiency. In Fig. 6.3 (b) the SNR is compared for probe density of 5.2×10^{12} molecules/cm² and different flows of target molecules to the surface, which vary from $\frac{1}{100} \mu\text{M}$ to $\frac{1}{40} \mu\text{M}$. The raise of the flow generates an increase in SNR and reduces the time, during which the SNR reaches its maximal value. In Fig. 6.3 (c), we investigate the situation, where the different probe densities and the fixed target concentration of $\frac{1}{70} \mu\text{M}$ at the surface determine the signal-to-noise ratio. The increase of the initial amount of the probe molecules induces the rise in the SNR at the same time.

Fig. 6.4 shows the standard deviation in linear (a) an logarithmic (b) scales, which are calculated with nominal parameters. By analyzing Fig. 6.4 and Fig. 6.3 we can identify five time intervals. in which the standard deviation increases $I_1 = [0, 100]$ or decreases $I_2 = [100, 1000]$ rapidly, an interval with weak depletion $I_3 = [1000, 2000]$, an interval $I_4 = [2000, 3300]$, where $1 > \sigma \geq \epsilon_\sigma > 0$ and an interval $I_5 = [2000, \infty]$ with a constant standard deviation $\sigma = \epsilon_\sigma$, where ϵ_σ is lower bound of standard deviation, given by (6.14). In the first three regions the SNR is small. Despite of the fact that the binding efficiency is constant after 1000s, the standard deviation gives rise to SNR only in the fourth interval and keeps it

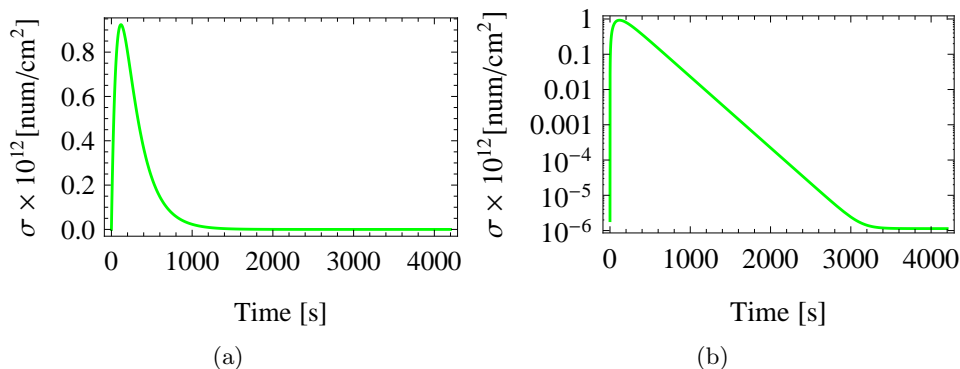


Figure 6.4: The standard deviation in linear (a) and logarithmic (b) scales.

constant in I_5 , since there is no any additional source of target molecules. The behavior of the standard deviation, of the SNR and of the binding efficiency is summarized in Table 6.3.

Interval	Standard deviation	SNR	Binding efficiency
$I_1 = [0, 100]$	increase rapidly	small	increase rapidly
$I_2 = [100, 1000]$	decrease rapidly	small	increase slowly
$I_3 = [1000, 2000]$	decrease slowly	small	constant
$I_4 = [2000, 3300]$	decrease slowly	increase rapidly	constant
$I_5 = [3300, \infty]$	constant	constant	constant

Table 6.3: The behavior of the standard deviation, of the SNR and of the binding efficiency during the time.

The coupled model

As it mentioned above, the explicit dependency of binding efficiency and of SNR on the transport of analyte molecules requires to connect the stochastic model for SNR with the continuum model for analyte transport. In this section we consider a standard deviation and signal-to-noise ratio for the coupled model, which are calculated with the nominal parameters and the flux given in Section 4.3. The probe density varies from 2×10^{12} molecules/cm² to 4×10^{12} molecules/cm².

Despite of the fact, that the change in the transport is small, a difference of standard deviations is observed, as demonstrated in Fig. 6.5. The time of stochastic fluctuations is also different.

Hence, the difference in standard deviations gives a small distinction to the signal-to-noise ratios, which are shown in Fig. 6.6 (a). In the case, when the electrolyte solution will contain a larger amount of analyte molecules we expected a higher SNR at the shorter time. Such behavior is illustrated in Fig. 6.6 (b).

Similarly as above, we summarize the behavior of the standard deviation, of the SNR

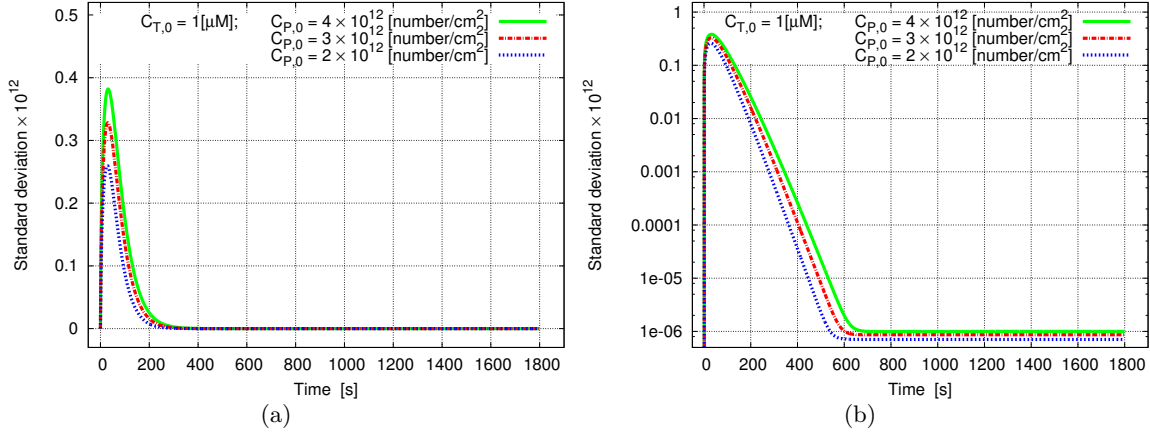


Figure 6.5: The standard deviation in linear (a) and logarithmic (b) scales.

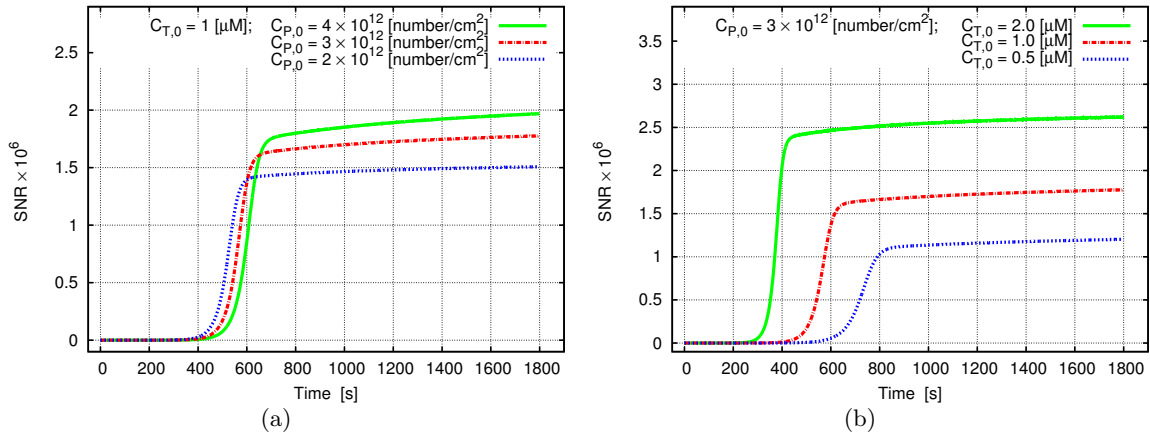


Figure 6.6: Signal-to-noise ratios calculated by different probe densities (a) and different initial analyte concentrations (b).

and of the binding efficiency in Table 6.4. The rapid increase and decrease of the standard deviation are shown in the intervals I_1 and I_2 , respectively. The rapid increase of the signal-to-noise ratio occurs during the time interval I_4 . Hence, all considered parameters are constant only in the interval I_5 .

Comparison of Table 6.3 with Table 6.4 demonstrates that not only the analysis of the binding efficiency but also the examination of the signal-to-noise ratio are essential for the estimation of measurement time.

Interval	Standard deviation	SNR	Binding efficiency
$I_1 = [0, 50]$	increase rapidly	small	increase rapidly
$I_2 = [50, 200]$	decrease rapidly	small	increase
$I_3 = [200, 400]$	decrease slowly	small	increase slowly
$I_4 = [400, 650]$	decrease slowly	increase rapidly	increase slowly
$I_5 = [650, \infty]$	constant	constant	increase very slowly and is constant for $t > 1800$

Table 6.4: The behavior of the standard deviation, of the SNR and of the binding efficiency during the time.

6.5 Conclusions

In this chapter we treat the chemical reaction as stochastic process and obtain the Langevin equation for the association and the dissociation processes at the surface. That allows us to derive the mean value and the standard deviation of probe-target complexes and, therefore, the signal-to-noise ratio analytically.

The simulations show that the observed signal-to-noise ratio is proportional to the initial amount of the probe molecules and to the analyte flow. Along with that the SNR is inversely proportional to the binding efficiency. We can conclude that the signal-to-noise ratio and the binding efficiency have to be analyzed together to choose the design parameters. Moreover, due to sensitivity of the SNR to the presence of free target molecules near functionalized surface, the stochastic model for SNR and the continuum model for analyte transport have to be considered together. We also study the coupled model and find that the response time strongly depends on the SNR and on the binding efficiency. Thus, to estimate the measurement time we also have to pay attention to both to the SNR and to the BE.

The presented method can be applied for analyzes and prediction of the noise behavior and, thus, makes possible the design of the biophysical part of the DNA-based sensors. It is a beneficial tool to achieve the acceptable speed and efficiency of the hybridization, to predict the measurement time, and to sensitively detect the DNAs of interest.

Appendix A

Variables and units

The variables and their units or values for calculation are summarized in this table.

Meaning	Variable	Unit or value
Elementary charge	q	$1.6021917 \cdot 10^{-19}$ C
Boltzmann constant	k_B	$1.3806 \cdot 10^{-23}$ CVK ⁻¹
	β	$2.4144 \cdot 10^{20}$ C ⁻¹ V ⁻¹
Avogadro number	N_A	$6.0221417930 \cdot 10^{23}$ mol ⁻¹
Vacuum permittivity	ε_0	$8.85418781762 \cdot 10^{-12}$ CV ⁻¹ m ⁻¹
Dielectric constant of water	ε_{Liq}	80.1
Dielectric constant of silicon	ε_{Si}	11.7
Dielectric constant of silicon-dioxide	ε_{Ox}	3.9
Thermal de-Broglie wavelength	Λ	nm
Number of particles	N	1
Temperature	T	K
Valence	z, z_i	1
Charge of species i	q_i	C
Ionic concentration	c	M
Surface charge density	$\rho, \sigma, \hat{\sigma}$	C nm ⁻²
Charge concentration	ϱ, ϱ_i	q nm ⁻³
Surface charge density multiplied by the space step	ϱ_s, ϱ_{Ox}	q nm ⁻³
Target concentration	$C_{T,0}, C_T$	M
Probe density	$C_{P,0}, C_P$	molecules cm ⁻²
Density of probe-target complexes	C_{PT}	molecules cm ⁻²
Density of non-specific binding molecules	$C_{nT}, C_{nT,max}$	molecules cm ⁻²
Macroscopic surface charge density	\mathcal{C}	q nm ⁻²
Macroscopic dipole moment density	\mathcal{D}	q nm ⁻¹
Electron concentration	n	q nm ⁻³
Hole concentration	p	q nm ⁻³

Intrinsic carrier concentration	n_{in}	$q \text{ nm}^{-3}$
Electron mobility	μ_n	$\text{nm}^2 \text{ V}^{-1} \text{ s}^{-1}$
Hole mobility	μ_p	$\text{nm}^2 \text{ V}^{-1} \text{ s}^{-1}$
Electron life-time	τ_n	s
Hole life-time	τ_p	s
Recombination-generation rate	R	$q \text{ nm}^2 \text{ s}^{-1}$
Electron current density	J_n	$q \text{ nm}^{-2} \text{ s}^{-1}$
Hole current density	J_p	$q \text{ nm}^{-2} \text{ s}^{-1}$
Current flow	J, J_C, J_D, J_M	$\text{mol nm}^{-2} \text{ s}^{-1}$
Electric field	E	N C^{-1}
Electrostatic potential energy	U	J
Helmholtz free energy	A_H	J
Applied voltage	Φ	V
Thermal voltage	U_{th}	V
Electrical potential	Ψ, ψ	V
Chemical potential	μ	J
Length of DNA	L_{bp}	number of bp
Radius of DNA	R_P, R_T, R_{PT}	nm
Length	$W, H, L,$ d, h, r	nm
Area	A	nm^2
Volume	V	nm^3
Fluid viscosity	μ_f	N s m^{-2}
Fluid velocity	ν	nm s^{-1}
Diffusion coefficient	D, D_n, D_p	$\text{nm}^2 \text{ s}^{-1}$
Association rate	r_a	$\text{M}^{-1} \text{ s}^{-1}$
Dissociation rate	r_d	s^{-1}
Adsorption rate	k_a	$\text{M}^{-1} \text{ s}^{-1}$
Desorption rate	k_d	s^{-1}
Time	t	s

Appendix B

Theorems

Theorem B.0.1. (*Banach's Fixed Point Theorem [18]*)

Assume $G : \mathcal{K} \rightarrow \mathcal{K}$ is a nonlinear mapping, and suppose that

$$\|Gu - Gu^*\| \leq \gamma \|u - u^*\| \quad u, u^* \in \mathcal{K}$$

for some constant $\gamma < 1$. Then G has a unique fixed point.

Theorem B.0.2. (*Gauss' Divergence Theorem [20, 87]*)

Let Ω be a bounded domain in \mathbb{R}^3 satisfying the following conditions

- (a) The boundary $S = \partial\Omega$ of Ω consists of a finite number of smooth surfaces.
- (b) Any straight line parallel to any of the coordinate axes either intersects S at a finite number of points or has a whole interval common with S .

Let $\mathbf{F} = (P, Q, R)$ be a vector field defined in $\bar{\Omega}$ such that each of the components P, Q, R are in $C^1(\Omega) \cup C^0(\bar{\Omega})$ and integral

$$\int_{\Omega} \nabla \cdot \mathbf{F} \, d\mathbf{v} := \iiint_{\Omega} (\partial_x P + \partial_y Q + \partial_z R) \, dx \, dy \, dz$$

is convergent. Then

$$\int_{\Omega} \nabla \cdot \mathbf{F} \, d\mathbf{v} := \int_S \mathbf{F} \cdot \bar{\mathbf{n}} \, d\sigma$$

where $\bar{\mathbf{n}}$ is the outward pointing normal vector, and $d\sigma$ is the element of surface on S .

Theorem B.0.3. (Picard-Lindelöf Theorem [38])

Let $F \in \mathbb{R}^{n+1}$ be a domain and let $f : F \rightarrow \mathbb{R}^n$ be a continuous function satisfying a Lipschitz conditions

$$\|f(t, u) - f(t, v)\| \leq L\|u - v\|$$

for all $(t, u), (t, v) \in F$ and some constant $L > 0$. Then for each initial data pair (t_0, u_0) there exists an interval $[t_0 - a, t_0 + a]$ with $a > 0$ such that the initial value problem

$$\begin{aligned} \frac{\partial u(t)}{\partial t} &= f(t, u), \\ u(t_0) &= u_0 \end{aligned}$$

has a unique solution in this interval.

Theorem B.0.4. (Weak maximum principle for the second-order parabolic PDE for $c \geq 0$ [18])

Consider the initial/boundary-value problem

$$\begin{aligned} u_t + Lu &= f && \text{in } [0, T] \times \Omega, \\ u &= u_D && \text{on } [0, T] \times \partial\Omega, \\ u &= u_I && \text{on } \{t = 0\} \times \Omega, \end{aligned}$$

where $f(t, x) : [0, T] \times \Omega \rightarrow \mathbb{R}$, $u_I : \Omega \rightarrow \mathbb{R}$ are given, $u = u(t, x) : \bar{\Omega} \rightarrow \mathbb{R}$ is unknown, and L is a second-order partial differential operator having the divergence form

$$Lu = - \sum_{i,j=1}^n \nabla_{x_i} (a_{i,j}(t, x) \nabla_{x_j} u) - \sum_{i=1}^n \nabla_{x_i} b_i(t, x) u + c(t, x) u$$

for given coefficients $a_{i,j}$, b_i and c ($i, j = 1, \dots, n$).

Assume $u \in C_1^2(\bar{\Omega}) \cap C(\Omega)$ and $c \geq 0$ in Ω .

W1: If $u_t + Lu \leq 0$ in Ω , then $\max_{\Omega} u \leq \max_{\partial\Omega} \{\max(u, 0)\}$.

W2: If $u_t + Lu \geq 0$ in Ω , then $\min_{\Omega} u \geq -\max_{\partial\Omega} \{-\min(u, 0)\}$.

Bibliography

- [1] M.H. Abouzar, A.M. Pedraza, Schöning, and A. Poghossian, *Label-free DNA hybridization and denaturation detection by means of field-effect nanoplate SOI capacitors functionalized with gold nanoparticles*, Proc. Eurosensors XXIV (Linz, Austria), vol. 5, Procedia Engineering, sep 2010, pp. 918–921. 4, 8
- [2] Edvard Allen, *Modeling with Itô stochastic differential equations*, Springer-Verlag, 2007. 75
- [3] M. P. Allen and D. J. Tildesley, *Computer simulation of liquids*, Oxford University Press, Oxford, New York, 1987. 3, 25, 27
- [4] Gerda Ara and James G. Mullen, *Effect of ion size on diffusion in alkali halides*, Phys. Rev. **143** (1966), no. 2, 663–665. 18, 25
- [5] P. Bergveld and A. Sibbald, *Analytical and biomedical applications of ion-selective field-effect transistors*, Elsevier, Amsterdam, 1988. 20, 22
- [6] D. Boda, K.-Y. Chan, and D. Henderson, *Monte Carlo simulation of an ion-dipole mixture as a model of an electrical double layer*, JCHEP **109** (1998), no. 17, 7362–7371. 25, 31
- [7] D. Boda, W. R. Fawcett, D. Henderson, and S. Sokołowski, *Monte Carlo, density functional theory, and Poisson–Boltzmann theory study of the structure of an electrolyte near an electrode*, JCHEP **116** (2002), no. 16, 7170–7176. 25, 38
- [8] D. Boda, D. Henderson, and K.-Y. Chan, *Monte Carlo study of the capacitance of the double layer in a model molten salt*, JCHEP **110** (1999), no. 11, 5346–5350. 38
- [9] D. Boda, D. Henderson, P. Plaschko, and W. R. Fawcett, *Monte Carlo and density functional theory study of the electrical double layer: The dependence of the charge/voltage relation on the diameter of the ions*, Mol. Simulat. **30** (2004), no. 2-3, 137–141. 3, 25
- [10] Leland C. Clark and Champ Lyons, *Electrode systems for continuous monitoring in cardiovascular surgery*, Ann. N. Y. Acad. Sci. **102** (1962), 29–45. 1
- [11] H. Cohen and J.W. Cooley, *The numerical solution of the time-dependent Nernst-Planck equations*, J. Biophys. **5** (1965), no. 2, 257–268. 4

-
- [12] Y. Cui, X. F. Duan, J. T. Hu, and C. M. Lieber, *Doping and electrical transport in silicon nanowires*, J. Phys. Chem. B **104** (2000), 5213–5216. 11
- [13] P. Debye and E. Hückel, *Zur Theorie der Elektrolyte. I. Gefrierpunktserniedrigung und verwandte Erscheinungen*, Physikalische Zeitschrift **24** (1923), no. 9, 185–206. 3, 25
- [14] M. J. Deen, M. W. Shinwari, and J. C. Ranuárez, *Noise considerations in field-effect biosensors*, J. Appl. Phys. **100** (2006), 074703/1–8. 4
- [15] Rory Dijkink and Claus-Dieter Ohl, *Laser-induced cavitation based micropump*, Lab Chip **8** (2008), 1676–1681. 17
- [16] N. Elfström, R. Juhasz, I. Sychugov, T. Engfeldt, A. E. Karlström, and J. Linnros, *Surface charge sensitivity of silicon nanowires: Size dependence*, Nano Lett. **7** (2007), no. 9, 2608–2612. 8
- [17] David Erickson, Dongqing Li, and Ulrich J. Krull, *Modeling of DNA hybridisation kinetics for spatially resolved biochip*, Anal. Biochem. **317** (2003), no. 2, 186–200. 4
- [18] L. C. Evans, *Partial differential equations*, Oxford University Press, 1998. 51, 87, 88
- [19] E. Fatemi and F. Odeh, *Upwind finite difference solution of Boltzmann equation applied to electron transport in semiconductor devices*, JCOMP2 **108** (1993), no. 2, 209–217. 3
- [20] R. P. Feynman, R. B. Leighton, and M. Sands, *The feynman lectures on physic. ii. mainly electromagnetism and matter*, Addison-Wesley Publishing Company, Massachusetts, 2005. 87
- [21] Daan Frenkel and Berend Smit, *Understanding molecular simulation*, academic press, London WC1X 8RR, UK, 2002. 3
- [22] J. Fritz, E. B. Cooper, S. Gaudet, P. K. Sorger, and S. R. Manalis, *Electronic detection of DNA by its intrinsic molecular charge*, PRONA **99** (2002), no. 22, 14142–14146. 4, 9
- [23] Z. Gao, A. Agarwal, A. D. Trigg, N. Singh, C. Fang, C.-H. Tung, Y. Fan, K. D. Buddharaaju, and J. Kong, *Silicon nanowire arrays for label-free detection of DNA*, Analytical Chemistry A **79** (2007), no. 9, 3291–3297. 4
- [24] Daniel T. Gillespie, *The chemical Langevin equation*, J. Chem. Phys. **113** (2000), no. 1, 297–306. 72
- [25] Teena Goel, Chandra N. Patra, Swapan K. Ghosh, and Tulsi Mukherjee, *Three component model of cylindrical electric double layers containing mixed electrolytes: A systematic study by Monte Carlo simulations and density functional theory*, J. Chem. Phys. **132** (2010), no. 19, 194706. 25
- [26] J. Hahm and C. M. Lieber, *Direct ultrasensitive electrical detection of DNA and DNA sequence variations using nanowire nanosensors*, Nano Lett. **4** (2004), no. 1, 51–54. 4

- [27] Zhang Hai-Lang and Han Shi-Jun, *Viscosity and density of water + sodium chloride + potassium chloride solutions at 298.15 K*, J. Chem. Eng. Data **41** (1996), no. 3, 516–520. 58
- [28] A. Hassibi, R. Navid, R. W. Dutton, and T. H. Lee, *Comprehensive study of noise processes in electrode electrolyte interfaces*, J. Appl. Phys. **96** (2004), no. 2, 1074–1082. 4
- [29] A. Hassibi, S. Zahedi, R. Navid, R. W. Dutton, and T. H. Lee, *Biological shot-noise and quantum-limited signal-to-noise ratio in affinity-based biosensors*, J. Appl. Phys. **97** (2005), 084701/1–10. 4
- [30] Clemens Heitzinger, Rick Kennell, Gerhard Klimeck, Norbert Mauser, Michael McLennan, and Christian Ringhofer, *Modeling and simulation of field-effect biosensors (BioFETs) and their deployment on the nanoHUB*, J. Phys.: Conf. Ser. **107** (2008), 012004/1–12. 63
- [31] Clemens Heitzinger, Yang Liu, Norbert Mauser, Christian Ringhofer, and Robert Dutton, *Calculation of fluctuations in boundary layers of nanowire field-effect biosensors*, J. Comput. Theor. Nanosci. **7** (2010), no. 12, 1–7. 26
- [32] Clemens Heitzinger, Norbert Mauser, and Christian Ringhofer, *Multiscale modeling of planar and nanowire field-effect biosensors*, *siaja* **70** (2010), no. 5, 1634–1654. 63
- [33] Desmond J. Higham, *Modeling and simulation chemical reactions*, SIAM Rev. **50** (2008), no. 2, 347–368. 4, 72
- [34] Heather K. Hunt and Andrea M. Armani, *Label-free biological and chemical sensors*, *Nanoscale* **2** (2010), no. 9, 1544–1559. 1, 2, 9
- [35] S. Ingebrandt, Y. Hana, F. Nakamura, A. Poghossian, M.J. Schöning, and A. Offenhäusser, *Label-free detection of single nucleotide polymorphisms utilizing the differential transfer function of field-effect transistors*, *Biosens. Bioelectron.* **22** (2007), no. 12, 2834–2840. 2
- [36] K. Kiyohara and K. Asaka, *Monte Carlo simulation of electrolytes in the constant voltage ensemble*, *JCHEP* **126** (2007), 214704. 25, 27
- [37] J. F. Klemic, E. Stern, and M. A. Reed, *Hotwiring biosensors*, *Nature Biotechnology* **19** (2001), 924–925. 9
- [38] Rainer Kress, *Numerical analysis*, Springer-Verlag, New York, Berlin, Heidelberg, 1998. 88
- [39] Murray A. Lampert and Richard S. Crandall, *Nonlinear Poisson–Boltzmann theory for polyelectrolyte solutions: The counterion condensate around a line charge as a δ -function*, *Chem. Phys. Lett.* **72** (1980), 481–486. 3, 25

-
- [40] D. Landheer, G. Aers, W. R. McKinnon, M. J. Deen, and J. C. Ranuárez, *Model for the field effect from layers of biological macromolecules on the gate of metal-oxide-semiconductor transistors*, J. Appl. Phys. **98** (2005), 044701/1–15. 4
- [41] A. Majorana and R. M. Pidotella, *A finite difference scheme solving the Boltzmann–Poisson system for semiconductor devices*, JCOMP2 **174** (2001), no. 2, 649–668. 3
- [42] A. Malasics, D. Gillespie, and D. Boda, *Simulating prescribed particle densities in the grand canonical ensemble using iterative algorithms*, JCHEP **128** (2008), 124102. 3, 25, 30
- [43] P. A. Markowich, *The stationary semiconductor device equations*, Springer-Verlag, Wien, 1986. 3, 10
- [44] P. A. Markowich, C. A. Ringhofer, and C. Schmeiser, *Semiconductor equations*, Springer-Verlag, Wien, 1990. 3, 10
- [45] N. Metropolis, A. W. Rosenbluth, M. N. Rosenbluth, A. H. Teller, and E. Teller, *Equation of state calculations by fast computing machines*, JCHEP **21** (1953), 1087–1092. 27
- [46] N. Metropolis and S. Ulam, *The Monte Carlo method*, JAMES **44** (1949), 335–341. 3, 25, 27
- [47] P. Nair and M. Alam, *Design considerations of silicon nanowire biosensors*, IEEE Trans. El. Dev. **54** (2007), no. 12, 3400–3408. 1
- [48] Liviu Nicu and Thierry Le'ichlé, *Biosensors and tools for surface functionalization from the macro to the nanoscale: The way forward*, J. Appl. Phys. **104** (2008), no. 11, 111101/1–15. 1
- [49] C. W. Outhwaite and L. B. Bhuiyan, *A modified Poisson–Boltzmann analysis of the electric double layer around an isolated spherical macroion*, Molecular Physics **74** (1991), no. 2, 367–381. 3, 25
- [50] Won II Park, Gengfeng Zheng, Xiaocheng Jiang, Bozhi Tian, and Charles M. Lieber, *Controlled synthesis of millimeter-long silicon nanowires with uniform electronic properties*, Nano Lett. **8** (2008), no. 9, 3004–3009. 8
- [51] F. Patolsky, B. P. Timko, G. Yu, Y. Fang, A. B. Greytak, G. Zheng, and C. M. Lieber, *Detection, stimulation, and inhibition of neuronal signals with high-density nanowire transistor arrays*, SCIEN **313** (2006), 1100–1104. 8
- [52] F. Patolsky, G. Zheng, and C. M. Lieber, *Fabrication of silicon nanowire devices for ultrasensitive, label-free, real-time detection of biological and chemical species*, Nature Protocols **1** (2006), no. 4, 1711–1724. 1, 2
- [53] Daniel E. Perea, Eric R. Hemesath, Edwin J. Schwalbach, Jessica L. Lensch-Falk, Peter W. Voorhees, and Lincoln J. Lauhon, *Direct measurement of dopant distribution in*

- an individual vapour-liquid-solid nanowire*, Nature Nanotechnology **4** (2009), 315–319. 11
- [54] A. W. Peterson, R. J. Heaton, and R. M. Georgiadis, *The effect of surface probe density on DNA hybridization*, Nucleic Acids Res. **29** (2001), no. 24, 5163–5168. 4, 26, 60, 78, 79
- [55] A. W. Peterson, L. K. Wolf, and R. M. Georgiadis, *Hybridization of mismatched or partially matched DNA at surfaces*, J. Am. Chem. Soc. **124** (2002), no. 49, 14601–14607. 4, 62, 78
- [56] A. Poghosian, M.H. Abouzar, F. Amberger, D. Mayerb, Y. Hanb, S. Ingebrandt, A. Offenhäusser, and M.J. Schoning, *Field-effect sensors with charged macromolecules: Characterisation by capacitance-voltage, constant-capacitance, impedance spectroscopy and atomic-force microscopy methods*, Biosens. Bioelectron. **22** (2007), no. 9-10, 2100–2107. 8
- [57] A. Poghosian, M.H. Abouzar, and M.J. Schoning, *Capacitance-voltage and impedance characteristics of field-effect EIS sensors functionalised with polyelectrolyte multilayers*, ITBM-RBM **29** (2008), no. 2-3, 149–154. 8
- [58] A. Poghosian, A. Cherstvy, S. Ingebrandt, A. Offenhäuser, and M. J. Schöning, *Possibilities and limitations of label-free detection of DNA hybridization with field-effect-based devices*, Sensors and Actuators B **111-112** (2005), 470–480. 2, 9
- [59] Andreas Richter, Stephan Klatt, Georgi Paschew, and Christian Klenke, *Micropumps operated by swelling and shrinking of temperature-sensitive hydrogels*, Lab Chip **9** (2009), 613–618. 17
- [60] Christian Ringhofer and Clemens Heitzinger, *Multi-scale modeling and simulation of field-effect biosensors*, ECS Transactions **14** (2008), no. 1, 11–19. 63
- [61] M. J. Schöning and A. Poghosian, *Recent advances in biologically sensitive field-effect transistors (BioFETs)*, Analyst **127** (2002), 1137–1151. 1, 2, 7, 9
- [62] ———, *Bio FEDs (field-effect devices): State-of-the-art and new directions*, Electroanalysis **18** (2006), no. 19-20, 1893–1900. 9
- [63] K. A. Sharp and B. Honig, *Electrostatic interactions in macromolecules: Theory and applications*, Annu. Rev. Biophys. Biophys. Chem. **19** (1990), 301–332. 3, 25
- [64] P. E. Sheehan and L. J. Whitman, *Detection limits of nanoscale biosensors*, Nano Lett. **5** (2005), no. 4, 803–807. 3
- [65] T. M. Squires, R. J. Messinger, and S. R. Manalis, *Making it stick: Convection, reaction and diffusion in surface-based biosensors*, Nature Biotechnology **26** (2008), no. 4, 417–426. 4, 15

- [66] S. Ravindran and J. Wu, *Ion size effect on colloidal forces within the primitive model*, Condensed Matter Physics **8** (2005), no. 2, 377–388. 18, 25
- [67] E. Stern, *Label-free sensing with semiconducting nanowires*, Ph.D. thesis, Yale University, 2007. 7, 8
- [68] E. Stern, J. F. Klemic, D. A. Routenberg, P. N. Wyrembak, D. B. Turner-Evans, A. D. Hamilton, D. A. LaVan, T. M. Fahmy, and M. A. Reed, *Label-free immunodetection with CMOS-compatible semiconducting nanowires*, NATURE **445** (2007), 519–522. 2, 3, 7, 8
- [69] E. Stern, A. Vacic, N. K. Rajan, J. M. Criscione, J. Park, B. R. Ilic, D. J. Mooney, M. A. Reed, and T. M. Fahmy, *Label-free biomarker detection from whole blood*, Nature Nanotechnology **5** (2009), 138 – 142. 2, 9
- [70] A. H. Talasaz, M. Nemat-Gorgani, Y. Liu, P. StÅ¥hl, R. W. Dutton, M. Ronaghi, and R. W. Davis, *Prediction of protein orientation upon immobilization on biological and nonbiological surfaces*, PRONA **103** (2006), no. 40, 14773–14778. 3, 25, 26
- [71] Daniel R. Théavenot, Klar Toth, Richard A. Durst, and George S. Wilson, *Electrochemical biosensors: recommended definitions and classification*, Pure Appl. Chem. **71** (1999), no. 12, 2333–2348. 2, 3
- [72] Aleksey M. Tikhonov, *Ion-size effect at the surface of a silica hydrosol*, J. Chem. Phys. **130** (2009), no. 2, 024512. 18, 25
- [73] M. M. Tirado, C. L. Martinez, and J. G. Delatorre, *Comparison of theories for the translational and rotational diffusion coefficients of rod-like macromolecules. application to short DNA fragments*, J. Chem. Phys. **81** (1984), no. 4, 2047–2052. 59
- [74] G. M. Torrie and J. P. Valleau, *Electrical double layers. I. Monte Carlo study of a uniformly charged surface*, JCHEP **73** (1980), no. 11, 5807–5816. 3, 25, 31
- [75] George A. Truskey, Fan Yuan, and David F. Katz, *Transport phenomena in biological systems*, Pearson Prentice Hall, New Jersey, 2004. 4, 13
- [76] M. Valiskó, D. Boda, and G. Gillespie, *Selective adsorption of ions with different diameter and valence at highly-charged interfaces*, J. Phys. Chem. C **111** (2007), no. 43, 15575–15585. 3, 18, 25, 38
- [77] M. Valiskó, D. Henderson, and D. Boda, *Competition between the effects of asymmetries in ion diameters and charges in an electrical double layer studied by Monte Carlo simulations and theories*, J. Phys. Chem. B **108** (2004), no. 42, 16548–16555. 25, 38
- [78] D. van der Spoel, E. Lindahl, B. Hess, Carsten Kutzner, A. R. van Buuren, E. Apol, P. J. Meulenhoff, D. P. Tieleman, A. L. T. M. Sijbers, K. A. Feenstra, R. van Drunen, and H. J. C. Berendsen, *Gromacs user manual version 4.0*, 2006, http://www.gromacs.org/@api/deki/files/82/=gromacs4_manual.pdf. 19

- [79] R. E. G. van Hal, J. C. T. Eijkel, and P. Bergveld, *A novel description of ISFET sensitivity with the buffer capacity and double-layer capacitance as key parameters*, *Sensors and Actuators B* **24-25** (1995), 201–205. 20
- [80] A. H.-J. Wang, G. J. Quigley, F. J. Kolpac, J. L. Crawford, J. H. van Boom, G. van der Marel, and A. Rich, *Molecular structure of a left-handed double helical DNA fragment at atomic resolution*, *Nature* **282** (1979), no. 13, 680–686. 19
- [81] J. Wang, E. Palecek, P. E. Nielsen, G. Rivas, X. Cai, H. Shiraishi, N. Dontha, D. Luo, and P. A. M. Farias, *Peptide nucleic acid probes for sequence-specific DNA biosensors*, *JAMEC1* **118** (1996), no. 33, 7667–7670. 1
- [82] Ke Wang, Yang-Xin Yu, and Guang-Hua Gao, *Density functional study on the structures and thermodynamic properties of small ions around polyanionic dna*, *Phys. Rev. E* **70** (2004), no. 1, 011912. 25
- [83] Ke Wang, Yang-Xin Yu, Guang-Hua Gao, and Guang-Sheng Luo, *Density-functional theory and Monte Carlo simulation study on the electric double layer around DNA in mixed-size counterion system*, *JCHEP* **123** (2005), no. 23, 234904. 25
- [84] James G. Wetmur, *Hybridisation and renaturation kinetics of nucleic acids*, *Anna. Rev. Biophys. Bioeng* **5** (1976), 337–361. 4
- [85] James G. Wetmur and Norman Davidson, *Kinetics of renaturation of DNA*, *J. Mol. Biol.* **31** (1968), no. 3, 349–370. 4
- [86] X. Wu and X. Xu, *Degenerate semiconductor device equations with temperature effect*, *Nonlinear Analysis* **65** (2006), no. 2, 321–337. 3
- [87] E. G. Zachmanoglou and Dale W. Thoe, *Introduction to partial differential equations with applications*, Dover Publications, Mineola, N. Y. 11501, 1987. 87
- [88] Yi Zhang, Thomas C. Gamble, Alexander Neumann, Gabriel P. Lopez, Steven R. J. Brueck, and Dimiter N. Petsev, *Electric field control and analyte transport in Si/SiO₂ fluidic nanochannels*, *Lab Chip* **8** (2008), 1671–1675. 4, 17
- [89] G. Zheng, F. Patolsky, Y. Cui, W. U. Wang, and C. M. Lieber, *Multiplexed electrical detection of cancer markers with nanowire sensor arrays*, *Nature Biotechnology* **23** (2005), 1294–1301. 2, 7

Curriculum Vitae of Alena Bulyha

Alena Bulyha graduated from the Belarussian State University, Minsk with specialization in Mathematics. Diploma work was carried out at the Institute of Engineering Cybernetics / Academy of Sciences of Belarus, Minsk on the subject "Development of Algorithms and Programs for Detailed Control of Topographical Data Reliability" under supervision of Prof. Dr. Sergey V. Ablameyko with grade "excellent".

After graduating from the University Alena had the following research works:

on software development for application in physics and chemistry, cooperation with the Radiation Physics and Chemistry Problems Institute / Academy of Sciences of Belarus;

on geometry algorithms with certified results at the Institute of Informatics, Mainz University, Germany in group of Prof. Dr. Elmar Schömer "Algorithmic Geometry and Computer Graphics";

on developing of practical software applications for recognition of batch shapes (Gemengelage) for glass production industry, feasibility study, cooperation with Mainz University and Schott AG company, Mainz, Germany.

Alena began her PhD studies in October 2007 at the Institute for Analysis and Scientific Computing, Vienna University of Technology, Austria on the subject "Modeling and Simulation of Field-Effect Biosensors" under supervision of Prof. Dr. Christoph W. Überhuber and Dr. Clemens Heitzinger. Since Januar 2008 she has carried out her studies at the Faculty of Mathematics, University of Vienna, Austria under supervision of Prof. Dr. Nortbert J. Mauser and Dr. Clemens Heitzinger.

Publications on subject of thesis

1. [A. Bulyha](#) and C. Heitzinger, *An algorithm for three-dimensional Monte-Carlo simulation of charge distribution at biofunctionalized surfaces*, *Nanoscale*, 3(4), 1608-1617, 2011.
2. [A. Bulyha](#), C. Heitzinger and N. J. Mauser, *Bio-sensors: Modelling and simulation of biologically sensitive field-effect transistors*, *ERCIM-news*, 85, 40-41, 2011.
3. [A. Bulyha](#), C. Heitzinger, and N. J. Mauser, *A stochastic-deterministic approach for modelling of the biological noise in the DNA-sensors*, 2011, *In preparation*.
4. S. Baumgartner, [A. Bulyha](#), M. Vasicek, N. Tassotti, and C. Heitzinger, *Investigations of optimal sensitivity for biosensors using a 3d self-consistent drift-diffusion Monte Carlo approach*, 2011, *In preparation*.

Contributions to academic conferences and workshops

1. [A. Bulyha](#), C. Heitzinger and N. J. Mauser (2010) *Stochastic models of signal and noise in field-effect biosensors*. Poster at the Nanosensors for Industrial Application (NANOSENS 2010), Dec. 2-3, 2010, Tech Gate Vienna, Austria.

-
2. S. Baumgartner, A. Bulyha, C. Heitzinger and N. J. Mauser (2010) *Self-Consistent 3D Simulations of BioFETs*. Talk at the Nanosensors for Industrial Application (NANOSENS 2010), Dec. 2-3, 2010, Tech Gate Vienna, Austria.
 3. A. Bulyha (2010) *Modeling of stochastic processes in field-effect biosensors*. Talk at the 4th Annual Meeting "DEASE Summer-school", May 17-21, 2010 Hammamet, Tunisia.
 4. A. Bulyha, C. Heitzinger, and N. Mauser (2009) *Simulation of biofunctionalized surface layers using a Monte Carlo algorithm*. Talk at the 216th Meeting of the Electrochemical Society (ECS), Oct. 4-9, 2009, Vienna, Austria, Book of abstracts.
 5. A. Bulyha (2009) *Simulation of Biofunctionalized Surface Layers of Field-Effect Sensors*. Talk at the 3rd Annual Meeting "DEASE Summer-school", May 27-30, 2009, IACM - FORTH and University of Crete, Heraklion, Crete.
 6. C. Heitzinger, A. Bulyha, N. J. Mauser, C. Ringhofer, Y. Liu, R. Dutton (2008) *Stochastic and Continuum Models of Biofunctionalized Surface Layers for Multi-Scale Modeling of Field-Effect*. Talk at the Nanosensors for Industrial Application (NANOSENS 2008), Sept. 29-30, 2008, Tech Gate Vienna, Austria.
 7. A. Bulyha (2008) *Modeling and Simulation of Field-Effect Biosensors*. Talk at the 2nd Annual Meeting "DEASE Summer-school", Sept. 18-20, 2008, University of Hamburg and Hamburg University of Technology, Hamburg, Germany.